Measurement of the Beauty Cross Section using the Semileptonic Decay into Electrons at HERA

Dissertation

zur Erlangung des Doktorgrades
des Fachbereichs Physik
der Universität Hamburg

vorgelegt von
Bengt Wessling
aus Witten

Hamburg
2004

Gutachter der Dissertation:	Prof. Dr. V. Blobel Prof. Dr. R.-D. Heuer
Gutachter/Gutachterin der Disputation:	Prof. Dr. V. Blobel Prof. Dr. B. Naroska
Datum der Disputation:	1.12.2004
Dekan des Fachbereichs Physik und Vorsitzender des Prüfungsausschusses:	Prof. Dr. G. Huber

Abstract

The beauty production cross section is measured at the H1-Experiment at the electron proton collider HERA. The data taken in the years 1999 and 2000, corresponding to an integrated luminosity of 51 pb^{-1}, are divided in two kinematical ranges: photoproduction ($Q^2 < 0.01$ GeV^2) and deep inelastic scattering (2 GeV$^2 < Q^2 <$ 100 GeV^2). Events with beauty quarks are selected by requiring an electron with a transverse momentum larger than 2 GeV/c together with two jets with $p_T^{jet\,1(2)} > 6(5)$ GeV/c. The relative transverse momentum of the electron to the jet axis is used to separate electrons from beauty quarks from background processes. In order to reach a sufficient separation of signal and background events, a new reconstruction algorithm of the hadronic final state is developed as well as a new method to identify electrons in jets. For the latter, neural networks are used to combine calorimeter shower shape parameters with the specific energy loss $\mathrm{d}E/\mathrm{d}x$. The measured cross sections are found to be in agreement with predictions from leading-order QCD calculations using parton showers.

Kurzfassung

Es wird eine Messung des Wirkungsquerschnitts der b-Quark-Produktion beim H1-Experiment am Elektron-Proton-Beschleuniger HERA vorgestellt. Die untersuchten Daten der Jahre 1999 und 2000 entsprechen einer integrierten Luminosität von 51 pb^{-1} und sind in zwei kinematische Bereiche unterteilt: Photoproduktion ($Q^2 <$ 0.01 GeV^2) und tiefunelastische Streuung (2 GeV$^2 < Q^2 <$ 100 GeV^2). Ereignisse mit b-Quarks werden durch die Forderung nach einem Elektron mit einem Transversalimpuls von mehr als 2 GeV/c sowie zwei Jets mit $p_T^{jet\,1(2)} > 6(5)$ GeV/c ausgewählt. Der Transversalimpuls des Elektrons relativ zur Jetachse wird zur Trennung des b-Quark-Anteils vom Untergrund verwendet. Um eine ausreichende Trennung von Signal- und Untergrundereignissen zu erreichen, wird ein neuer Algorithmus zur Rekonstruktion des hadronischen Endzustandes entwickelt und eine neue Methode zur Identifizierung von Elektronen in Jets vorgestellt. Für letztere werden neuronale Netze verwendet, in denen die Formen von Kalorimeterschauern mit dem spezifischen Energieverlust $\mathrm{d}E/\mathrm{d}x$ kombiniert werden. Die gemessenen Wirkungsquerschnitte befinden sich in Übereinstimmung mit Vorhersagen von QCD-Rechnungen in führender Ordnung und Partonschauern.

Contents

Introduction

High momentum leptons produced in elementary particle collisions are often a sign for interesting processes since they may be decay products of heavy particles. Leptonic channels play an important role in the search for physics processes beyond the Standard Model and have been analysed in the discovery of the top quark. In the analysis presented here, electrons[1] are used for the measurement of the beauty quark production cross section at the electron proton accelerator HERA.

The advantages of leptonic beauty decay channels are manifold: lepton momenta are very well reconstructed compared to purely hadronic final states (jets) and especially muons can be triggered relatively easily. The production of leptons does not involve processes with large theoretical uncertainties and experimentally the signal to background ratio (ignoring hadron misidentification) is much better as is e. g. in case of jets where light quark production dominates.

The measurement of heavy quark production, which means beauty and charm quarks in case of experiments at HERA, provides a sensitive test of perturbative Quantum Chromodynamics (QCD) since the large masses of the quarks provide a hard scale. Much progress has been made within the last years in the understanding of the beauty quark cross section and it seems as if measurements and QCD predictions now agree within the uncertainties ([1, 2, 3]). Beauty production cross sections have to be precisely known in view of the upcoming Large Hadron Collider at CERN where it is expected to be one of the dominant sources of background processes for the discovery of a possible Higgs-boson.

At the H1-Experiment at HERA, heavy quark cross sections are currently measured using several approaches:

- reconstruction of final states, e. g. J/Ψ-mesons, either with or without using particle identification ([4], [5] and [6]),
- purely hadronic channels (jets), using lifetime information ([7]),
- semimuonic heavy quark decays together with jets ([8]) or with $D^{*\pm}$-mesons ([9]).

Up to now, electrons have only been used in the measurement of the production cross sections of J/Ψ-mesons ([10]) and the identification of electrons within jets has not yet been attempted. Still, having access to the electron channel would be worthwhile: the statistics of the leptonic

[1] The term 'electron' is used for both electrons and positrons throughout this thesis.

channels could be increased by a factor two. In addition, analyses using electrons would complement muon analyses in terms of understanding systematic uncertainties since different detectors are used for the particle identification. The background composition is different as well – cosmic muons and decays of pions and kaons are the main background contribution for one side, electrons from photon conversion processes for the other side.

A method for the identification of electrons in jets will be presented in this thesis. It is based on the following principles:

- an optimised association of tracks measured in tracking chambers and energy depositions in the calorimeter,
- early rejection of easily identified hadrons,
- usage of neural networks combining shower shape parameters with the specific energy loss measured in the tracking chamber.

The resulting algorithm provides a reconstruction of the Hadronic Final State in which energy is neither omitted nor counted twice. Electrons in dijet events are selected with purities of approximately 80%, less than 0.1% of all hadrons are falsely identified as electrons. The efficiency to identify electrons together with two jets is around 30%.

The outline of the thesis is as follows: a short overview on kinematical quantities relevant at HERA and on the theoretical aspects of heavy quark production is given first (chapter 1). Then, important components of the H1-Detector such as the Liquid Argon Calorimeter are briefly described (chapter 2). In the third chapter the data sets analysed are presented together with the data selections and the Monte Carlo simulations used. The new Hadronic Final State reconstruction algorithm is explained in the fourth chapter. The properties of electromagnetic and hadronic showers in calorimeters are briefly reviewed in the following chapter and shower shape parameters are defined. The electron identification using neural networks is explained in chapter 6 and the procedure to determine the fraction of electrons from beauty production in the data is described afterwards (chapter 7). Cross sections are presented in chapter 8 and systematic uncertainties are evaluated before giving a summary and an outlook in the last chapter.

Chapter 1

Heavy Quark Production at HERA

A general overview of electron proton (ep) interactions at HERA will be given first in this chapter and relevant kinematic quantities will be introduced. Then, the main features of heavy quark production will be presented before summarising the main concepts of QCD and Monte Carlo generators.

1.1 Kinematics

Virtual photons γ and gauge bosons Z^0, $W^{\pm}$ are exchanged in electron proton scattering processes. The interaction by the heavy bosons Z^0 and $W^{\pm}$ is suppressed at low momentum transfers at the electron vertex. The neutral current (NC) process is shown on the left side of figure 1.1 in a leading order diagram. The charged current (CC) process, mediated by a W^+- or W^--boson depending on whether electrons or positrons collide with protons, is depicted on the right hand side of this figure. The exchange of heavy bosons is relevant only in the case of very large momentum transfers at the electron vertex and will not be further considered here.

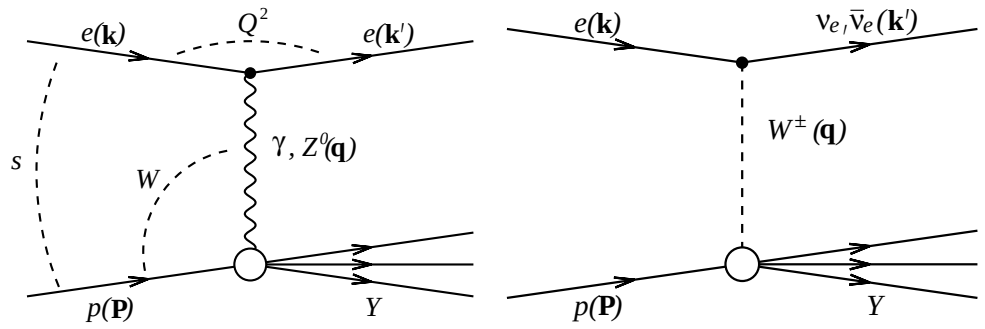

Figure 1.1: Left: *Neutral current (NC) ep interaction, described by the exchange of neutral bosons, γ and Z^0.* Right: *A charged $W^{\pm}$-boson mediates the charged current (CC) ep interaction in a leading order picture.*

The centre-of-mass energy of the ep system, $\sqrt{s}$, is expressed by the four-momenta of the incoming proton and electron, $\mathbf{P}$ and $\mathbf{k}$, respectively. The corresponding beam energies are denoted with E_p and E_e. (In the following, approximations are used if the equations only hold when neglecting proton and electron masses.)

$$s = (\mathbf{P} + \mathbf{k})^2 \approx 4 \cdot E_p \cdot E_e \tag{1.1}$$
$$Q^2 = -\mathbf{q}^2 = -(\mathbf{k} - \mathbf{k}')^2 \tag{1.2}$$

The negative four-momentum transfer squared from the electron to the proton, Q^2, is also called the photon virtuality. Two kinematic regions are distinguished: interactions with $Q^2 < 1$ GeV^2 belong to the **photoproduction** (γp) regime, a quasi-real photon is exchanged. Processes with $Q^2 > 1$ GeV^2 are referred to as **deep inelastic scattering** (DIS) events and the scattered electron is reconstructed in the main detector. The majority of processes at HERA are photoproduction events since the ep cross section is proportional to $1/Q^4$.

The Bjorken scaling variable x and the inelasticity y may be defined by $\mathbf{q}$ and the beam particles' four-momenta:

$$x = \frac{-\mathbf{q}^2}{2 \cdot \mathbf{P} \cdot \mathbf{q}} \tag{1.3}$$
$$y = \frac{\mathbf{P} \cdot \mathbf{q}}{\mathbf{P} \cdot \mathbf{k}} \tag{1.4}$$
$$Q^2 \approx s \cdot x \cdot y \tag{1.5}$$

x is interpreted in the Quark Parton Model, in the infinite momentum frame, as the fraction of the proton momentum carried by the struck quark. The inelasticity represents the relative electron energy transferred to the proton, calculated in the proton's rest frame.

When the scattered electron is reconstructed in the detector, its scattering angle ϑ'_e and its energies E_e and E'_e before and after the interaction may be used to reconstruct the event kinematics:

$$Q^2 \approx 4 \cdot E_e \cdot E'_e \cdot \cos^2 \frac{\vartheta'_e}{2} \tag{1.6}$$
$$y = 1 - \frac{E'_e}{E_e} \cdot \sin^2 \frac{\vartheta'_e}{2} \tag{1.7}$$

1.2 Heavy Quark Production

At HERA the main production process of heavy quark pairs is boson gluon fusion (BGF) ([11]). The pairwise production of top quarks is not possible at HERA because the centre-of-mass energy is less than twice the top quark mass.

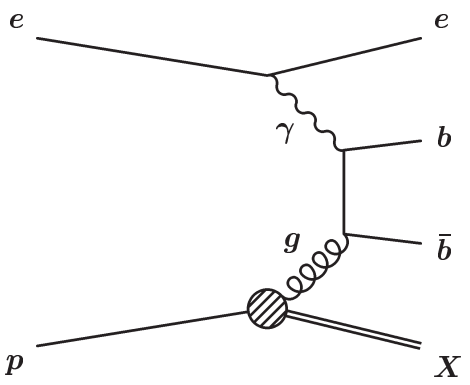

Figure 1.2: *Leading order Feynman diagram for the direct boson gluon fusion (BGF) process of heavy quark production at HERA.*

In a leading order picture the following contributions are found to be important: the *direct* BGF process for beauty production is shown in figure 1.2. A photon radiated off the electron and a gluon from the proton form the heavy quark pair. Heavy quark production via resolved BGF processes is expected to contribute as well at HERA. The *'normal' resolved* process is shown on the left hand side of figure 1.3: the photon fluctuates into a hadronic state which interacts with a gluon from the proton. The *flavour excitation* process is shown on the right hand side of this figure. The photon forms a heavy quark pair one of which takes part in the interaction with a gluon from the proton.

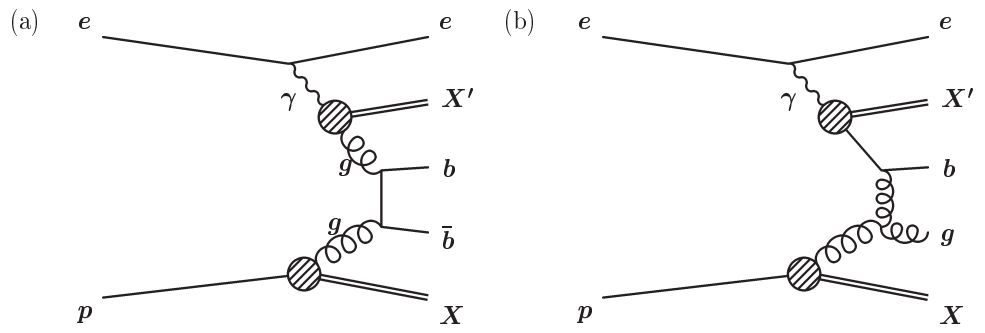

Figure 1.3: a) *'Normal' resolved heavy flavour BGF where e. g. a gluon from the proton interacts with the hadronic state of the photon, forming a heavy quark pair.* b) *Flavour excitation production of heavy quarks. The photon fluctuates into a heavy quark pair, one of the quarks enters the hard process with a gluon from the proton.*

At HERA the production of beauty quark pairs with respect to charm quark pairs is suppressed approximately by a factor 200 due to the larger mass of the beauty quark – 4.75 GeV/c^2

vs. 1.5 GeV/c^2 – and its smaller charge. The light quark production is about one order of magnitude larger than charm quark production.

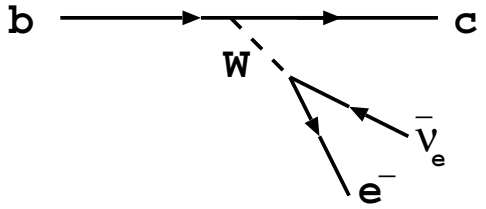

Figure 1.4: *Semileptonic decay of a beauty quark into a charm quark by the weak interaction via a $W^{\pm}$-boson. An electron and an anti-electron neutrino are created in this process; the neutrino escapes from the detector undetected.*

Leptons may be created in the *semileptonic decay* of heavy flavour hadrons via $W^{\pm}$-bosons in the weak interaction. A beauty quark is transformed into a charm quark in case of the beauty hadron decay, see figure 1.4. An electron and an anti-electron neutrino are created. The identification of electrons from beauty hadron decays is the subject of this analysis. The neutrino escapes from the detector undetected.

The branching ratio for the semielectronic decay of heavy quarks is ([12]):

$$\mathcal{B}R(b, c \to e) = 10.72\% \pm 0.16\% \tag{1.8}$$

Electron properties such as their momentum distribution differ for electrons from charm and beauty hadron decays. More energy is transferred to the daughter particles of the beauty hadrons due to the larger mass of the beauty quark. It will be described in chapter 7 how this can be used to separate electrons from charm and beauty production.

1.3 QCD and Monte Carlo Generators

The main concepts of Quantum Chromodynamics (QCD) are *infrared safety* and *factorisation*. They allow to apply results of perturbative QCD (pQCD) obtained on partons to real world particles ([13]). The factorisation theorem separates the calculable "hard" interaction from the non-perturbative "soft" process:

$$\mathrm{d}\sigma(ep \to e'X) = \sum_{partons} \int_0^1 \mathrm{d}x f_{i/p}(x, \mu_F^2) \cdot \mathrm{d}\hat{\sigma}_i \left(\hat{s}, \alpha_s\left(\mu_R\right), \mu_R, \mu_F\right) \tag{1.9}$$

Infrared safety is obtained by replacing infrared singular, perturbatively calculable, partonic fragmentation functions with non-perturbative, finite, hadronic fragmentation functions,

$f_{i/p}(x, \mu_F^2)$, interpreted as parton densities, where i denotes the parton from the proton. The factorisation scale μ_F represents the border between the soft and the hard interaction. The cross section $\hat{\sigma}_i\left(\hat{s}, \alpha_s\left(\mu_R\right), \mu_R, \mu_F\right)$ can be calculated in pQCD as a power series of the coupling constant α_s, with μ_R being the renormalisation scale, $\hat{s}$ is the centre-of-mass energy squared. Ultraviolet divergences are absorbed in the running of α_s. A schematic view of factorisation is shown in figure 1.5 with an *ep* event.

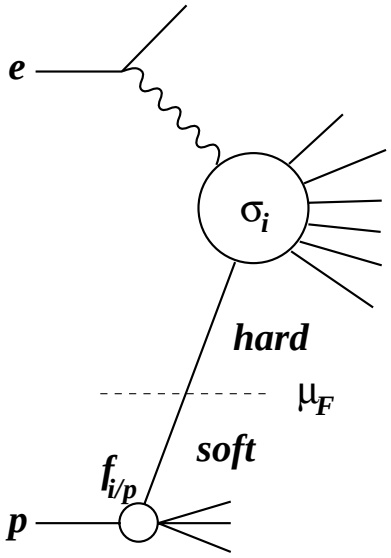

Figure 1.5: *Principle of factorisation in QCD.*

Parton densities are universal (independent of the scattering process) and depend only on the hadron type. They have to be determined with data at a scale μ, which is e. g. Q^2 in case of *ep* scattering, and can be calculated at any other scale using QCD evolution equations. Two of the Monte Carlo generators used in the analysis, PYTHIA ([14]) and RAPGAP ([15]), implement the DGLAP evolution equation ([16], [17]). The DGLAP evolution equation is characterised by the assumption that the gluon emission, the parton ladder, is ordered in k_T^2: $Q_0^2 < k_{T,0}^2 < \cdots < k_{T,n}^2 < Q^2$ where Q_0^2 is a suitably chosen scale. The CCFM evolution equation ([18, 19, 20]) represents an alternative model in which the gluon emissions are ordered according to the angles of the emitted gluons with respect to the incoming proton. It is implemented by the Monte Carlo generator CASCADE ([21], [22]) which is also used in the analysis. (More information about the individual Monte Carlo simulations can be found in section 3.3.)

The process in which colourless hadrons are formed from coloured quarks is called *fragmentation*. It is not calculable in pQCD and phenomenological models have to be used in the Monte Carlo generators. The two most successful models are the "Independent fragmentation" (Peterson fragmentation, [23]) and the "String fragmentation" (Lund fragmentation, [24]). In either case

two jets are formed when the heavy quarks hadronise individually. No hadrons are created if the heavy quark pair forms a bound state such as the J/Ψ-meson. Further particles are only produced in the decay of the meson. Therefore two jets are required in the data selection which is described in chapter 3 in more detail.

Chapter 2

HERA and the H1-Detector

The HERA accelerator and the H1-Detector have been described in detail in [25] and in many theses (e. g. [26], [9]). Therefore they will be only shortly presented in this chapter. Afterwards, the main features of the central tracking detector and of the calorimeters which are relevant for the analysis will be summarised before a brief overview of the trigger system will be given.

2.1 The HERA Accelerator

The HERA accelerator at DESY in Hamburg, Germany, is the world's first and up to now only electron proton collider. Protons are accelerated to energies of 920 GeV (before 1998: 820 GeV) in the 6.3 km long accelerator. With electron energies of 27.5 GeV, a centre-of-mass energy of $\sqrt{s} \approx 318$ GeV is reached. Electron and proton bunches collide every 96 ns in the two ep interaction zones where the experiments H1 and ZEUS are situated. A third experiment, HERMES, is using the electron beam to study the spin structure of nucleons in fixed target collisions. The HERA-B experiment in HERA's fourth interaction zone studied QCD in fixed target collisions of protons with heavy nuclei. This experiment stopped operations in 2003.

HERA's first run period ("HERA-I") ended in summer 2000. The accelerator was upgraded in the following 1.5 years to achieve five times higher luminosity than before. The detectors were upgraded and modernised as well. The most important project in view of heavy flavour physics at the H1-Experiment is the development of the Fast Track Trigger (FTT, [27]).

2.2 The H1-Detector

The H1-Detector is a general purpose detector for energy and momentum measurement of charged and neutral particles. The main focus is on the measurement of high momentum leptons such as the scattered interaction electron. The detector is instrumented asymmetrically to account for the different beam energies of protons and electrons. The amount of dead material has been reduced as much as possible; the superconducting coil comprises the tracking detectors and the calorimeters. The central detector is surrounded by an instrumented iron flux return yoke serving as a muon detector. Further devices exist for the detection of electrons and protons scattered under very small angles.

A schematic side view of the H1-Detector is shown in figure 2.1. The superconducting coil, between the Liquid Argon Calorimeter and the muon detector, is not drawn. The most important detectors for this analysis will be briefly presented in the next sections.

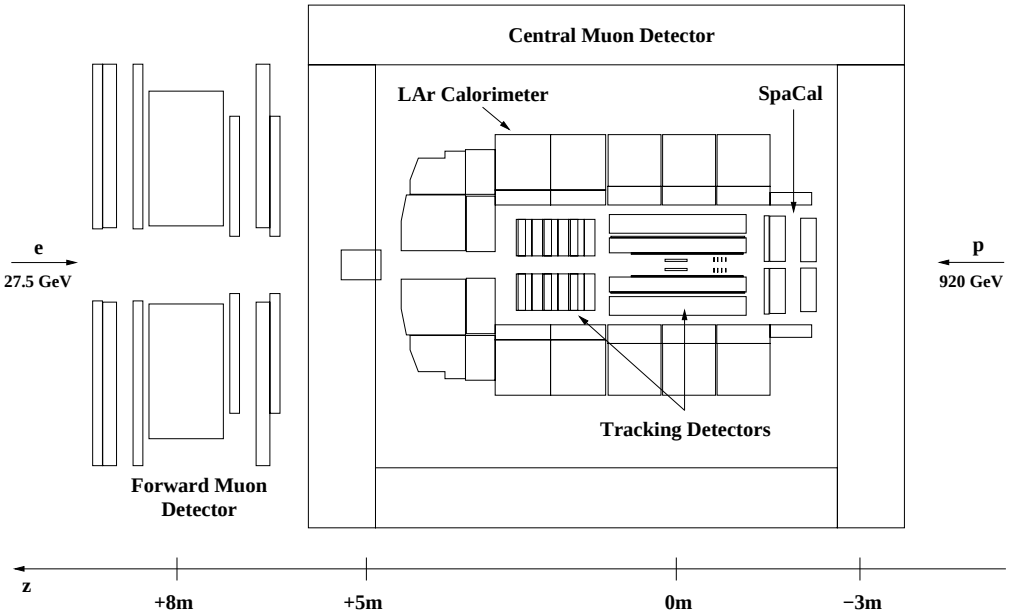

Figure 2.1: *Side view of the H1-Detector. The electrons are coming from the left side, protons from the right.*

The H1 coordinate system is oriented such that the positive z-axis points in the direction of the outgoing proton beam and the x-axis points to the centre of the HERA ring. The polar angle ϑ and the azimuthal angle φ are calculated with respect to these axes. The pseudorapidity η is also used instead of ϑ. It is defined as $\eta = -\ln(\tan\frac{\vartheta}{2})$.

2.3 Tracking Detectors

The momenta of charged particles can be measured using tracking detectors. There are two major tracking devices in the H1-Detector: the Central Jet Chamber (CJC) and the Forward Track Detector (FTD). The FTD was not fully operational in the run periods analysed here and will not be used.

The Central Jet Chamber consists of an inner and an outer drift chamber operated at ambient pressure. It covers a polar angle range from 20° to 160° and has a transverse momentum resolution of $\sigma(p_T)/p_T \simeq 0.005\ p_T[\mathrm{GeV}/c] \otimes 0.015$. It is complemented by two drift chambers for the measurement of the tracks' z-positions, the Central Inner/Outer Z-Chambers (CIZ, COZ) which are shown in figure 2.2 together with the other tracking detectors.

The Central Silicon Tracker (CST) ([28]) is the innermost track detector with a polar angle coverage from 30° to 150°. It consists of two layers, each measuring the $r-\varphi$- and z-positions of tracks independently.

Only the Central Jet Chamber provides redundant information and allows stand-alone track reconstruction. The tracks used in this analysis are reconstructed using the CJC. Z-position measurements delivered by the CIZ or COZ are added when available as well as $r-\varphi$-positions measured by the CST.

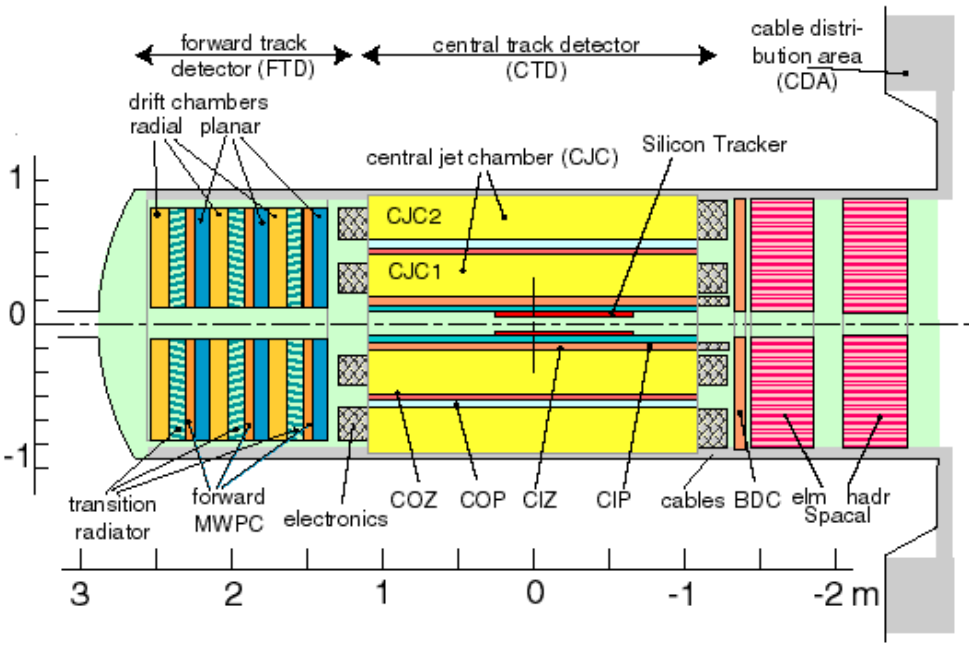

Figure 2.2: *Side view of the tracking system of the H1-Detector. The Central Jet Chamber is shown in the middle, followed by the forward track detectors to the left and by the Spaghetti Calorimeter (see section 2.4.2) to the right.*

The specific energy loss $\mathrm{d}E/\mathrm{d}x$ is measured by the CJC with a resolution of $\sigma(\mathrm{d}E/\mathrm{d}x)/(\mathrm{d}E/\mathrm{d}x) \simeq 8\%$ for long tracks. Electrons with momenta of more than 100 MeV/c have reached the saturation plateau and thus have a flat $\mathrm{d}E/\mathrm{d}x$ distribution. The $\mathrm{d}E/\mathrm{d}x$ value for hadrons in contrast is rising with increasing momenta from the energy loss minimum, around 500 MeV/c in case of pions, to this plateau through the "relativistic rise". The difference between the minimum and the plateau is about 30%. This can be seen from figure 2.3 where $\mathrm{d}E/\mathrm{d}x$ for electrons and pions is shown for particles with transverse momenta larger than 2 GeV/c.

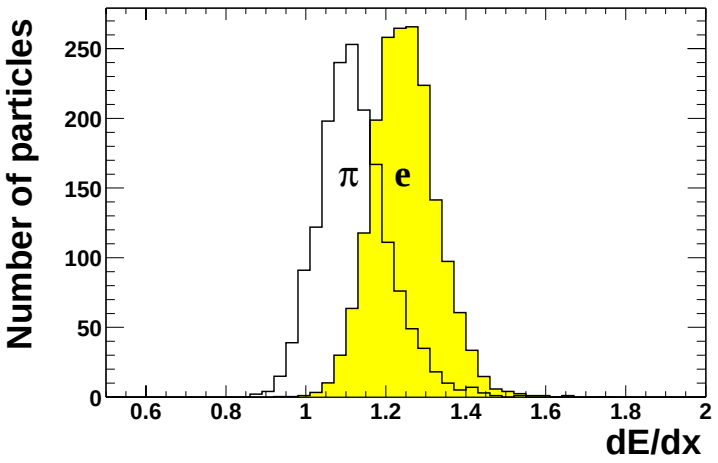

Figure 2.3: *The specific energy loss measured in the CJC for pions from K^0_S-meson decays (white histogram) and electrons from J/Ψ-meson decays (shaded histogram) for particles with transverse momenta larger than* 2 GeV/c.

2.4 Calorimeters

The energy of both charged and neutral particles can be measured with calorimeters. The actual amount of the energy deposited on average in a calorimeter depends on the particle type, its momentum and the calorimeter's configuration. The design of the two most important calorimeters in the H1-Detector will be presented in the next two sections.

2.4.1 Liquid Argon Calorimeter

The Liquid Argon Calorimeter (LAr) encloses the forward and the central part of the detector, it has a polar angle coverage from 4° to 155°. The amount of dead material between the tracking chambers and the calorimeter has been reduced to a minimum; it can however amount up to 2 radiation lengths in certain regions.

The LAr calorimeter is a sampling calorimeter and is non-compensating, with an e/π-ratio of ≈1.3. The absorber material in the electromagnetic part is lead whereas stainless steel is used in the hadronic section.

The electromagnetic part has a high segmentation, with a total of nearly 31,000 readout channels. One readout channel includes several cells consisting of absorber and active material. There are three successive readout channels in the radial direction in the central electromagnetic part of the LAr calorimeter. They correspond to approximately 20 radiation lengths. The energy resolution in the electromagnetic section is $\sigma(E)/E \simeq 12\%/\sqrt{E} \oplus 1\%$ as measured in test beams at CERN ([25]). The granularity of the hadronic section is much coarser than in the electromagnetic part with 13,500 readout cells. The hadronic calorimeter has an energy resolution of $\sigma(E)/E \simeq 50\%/\sqrt{E} \oplus 2\%$.

Both the electromagnetic and the hadronic section of the LAr calorimeter are divided into wheels along the z-axis (see figure 2.4). The segmentation in these wheels differs, ranging from 960 electromagnetic readout channels in the most backward wheel (denoted with *BBE* in figure 2.4) to more than 6100 in the most central one (*CB3E*). The space between these wheels is not instrumented and is therefore dead material. Each LAr wheel is divided into 8 octants (see figure 2.5 for a $r - \varphi$-view of the LAr wheel *CB2*). The space between the octants is not instrumented either.

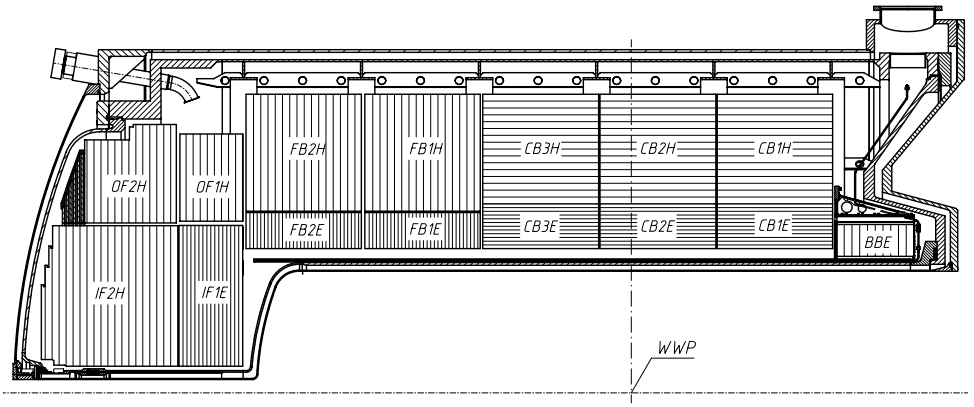

Figure 2.4: *Upper half of the Liquid Argon Calorimeter. The calorimeter is divided into 8 wheels of which the central 6 consist of an inner electromagnetic and an outer hadronic section. The point denoted with WWP is the nominal interaction point. The distance between the interaction region and the beginning of the calorimeter is approximately 100* cm*; the tracking chambers are mounted in between.*

A cluster in the calorimeter is defined as a group of adjacent calorimeter cells. The LAr reconstruction software aims at combining electromagnetic energy depositions, e. g. the scattered electron, into a single cluster. Hadron showers are typically split into several clusters so that the total energy for a hadron in the calorimeter is obtained by counting the energy in a certain cone.

There are three reconstruction energy levels for every calorimeter cluster which are determined by the LAr reconstruction software:

- *raw:* before dead material corrections,
- *electromagnetic:* after dead material corrections,
- *final:* after software weighting to correct for invisible energy contributions in hadronic showers, see also section 5.1. The energy weighting considers the distribution of energy depositions in cones. It has to be noted that energy weighting is only applied for cone energies larger than 10 GeV. Simple factors are used below 7 GeV and a mixture of both is performed in the range of 7 – 10 GeV.

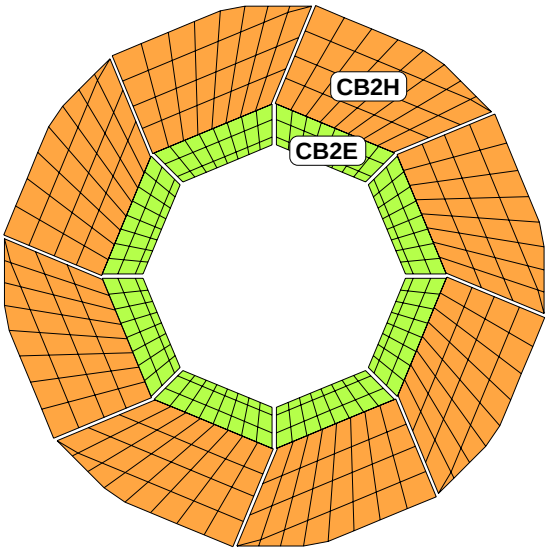

Figure 2.5: *$r-\varphi$-view of the LAr wheel CB2 which is composed of an inner electromagnetic calorimeter, CB2E, and an outer hadronic calorimeter, CB2H. The space between the octants of the calorimeter wheel is not instrumented.*

For the kinematic analysis of Hadronic Final States an association of tracks and energy depositions in the calorimeter is necessary. In this work the standard algorithm is not used. Instead, an alternative method is developed. The track cell association presented in chapter 4 operates on individual calorimeter cells, not on clusters. Their energies are taken at the electromagnetic scale. The final scale is chosen if cells are grouped to neutral clusters.

The LAr calorimeter data contain substantial amounts of electronic noise. Measures against the noise are already taken during the readout of the cells and later on in the reconstruction of clusters. (See [25] for more details.) Additional noise rejection cuts are applied in the course of the track cell association described in chapter 4.

2.4.2 Spaghetti Calorimeter

The inner part of the H1-Detector is completed in the backward region (corresponding to $z < 0$) by the Spaghetti Calorimeter (SpaCal, [29]) which is a lead/scintillating fibre calorimeter. Its angular acceptance is $151° < \vartheta < 178°$. The main task of the SpaCal is the precise measurement of the scattered electron. The energy resolution is $\sigma(E)/E \simeq 7.5\%/\sqrt{E} \oplus 1\%$ in the electromagnetic section and $\sigma(E)/E \simeq 30\%/\sqrt{E} \oplus 7\%$ in the hadronic part.

2.5 Luminosity System and Electron Taggers

Three TlCl/TlBr crystal Cherenkov detectors are situated in the electron flight direction at distances of $z = -33.4$m, $z = -43.2$m and $z = -102.9$m. The first two, called electron taggers

ET33 and ET44, are capable of detecting electrons scattered under very small angles. The ET33 is used in this analysis as will be described in section 3.1.2.

The detector at 103m is the photon detector and is used together with the ET33 for the luminosity measurement by the detection of photons resulting from Bethe-Heitler processes, $e + p \rightarrow e + p + \gamma$, for which the cross section is precisely known.

2.6 Trigger System

While electrons and protons cross at a rate of 10.4 MHz, physically interesting processes only happen in a small fraction of these collisions. It is the task of the trigger system to recognise and select these events and reduce the amount of background, e. g. interactions of beam particles with gas, as much as possible.

The H1 trigger system consists of five trigger levels, L1 to L5:
L1: The individual subdetectors deliver up to 192 trigger elements which yield up to 128 subtriggers. An example for a trigger element is the number of tracks above a certain transverse momentum threshold in the Central Jet Chamber. An event is accepted on L1 if at least one subtrigger is set. The input to L1 is about 100 kHz of which more than 99% are rejected. The decision whether to accept or to reject an event has to be made within 2.3 μs. The bandwidth to the next trigger level is limited so that some events are known to be rejected although a subtrigger has been set. A subtrigger for which only every Nth event is accepted is said to have a prescale of N. The integrated luminosity has to be corrected for a subtrigger's prescale.
L2: Neural networks and topological triggers are implemented on this trigger level. The trigger decision has to made within 20 μs on L2. The subtriggers used in this analysis, S61 and S83 (see the next chapter), have no L2 conditions.
L3: This level was not implemented during the HERA-I run period.
L4: The trigger decisions by L1 and L2 are validated after an online event reconstruction has been performed. The events either have to provide a "hard scale", e. g. a scattered electron with large Q^2, or have to be selected by one of the final state finders ("L4-finders"). The events are classified into L4-classes such as heavy flavour physics, jets, charged current events. A certain fraction of those events which have not been selected by an L4-finder is kept. These events have L4-weights assigned (see also section 3.2). The input to L4 is limited to 50 Hz, the output is fixed to 10 Hz. The maximally allowed decision time on L4 is 100 ms.
L5: An offline event reconstruction is performed and its output is permanently stored on tapes.

Chapter 3

Data Selection

The data sets used in this analysis will be presented in the first section of this chapter. Then, the event selection will be described before giving an overview of the Monte Carlo simulations used.

3.1 Data Sets

The data used in this analysis were taken in the years 1999 and 2000 when protons with energies of 920 GeV were brought to collision with positrons of 27.5 GeV. Run periods with electrons instead of positrons are not considered as is the case for non-standard conditions like the minimum bias run in 1999 or a period in the year 2000 when the interaction zone was shifted by +40 cm to access low photon virtualities.

If one of the main detectors, like the Central Jet Chambers, the LAr calorimeter, the SpaCal or the Luminosity System, is not functional during a luminosity run, the run quality is set to 'poor'. These runs are excluded from the analysis as well as runs where one of the other necessary detectors was not operational, see below. In addition, events are rejected when the z-position of the event vertex deviates more than 35 cm from the nominal interaction point, indicating that a positron interacted with a proton from a satellite bunch. A summary of integrated luminosities available for this analysis is given in table 3.1.

The event signature searched for in this analysis consists of two jets with minimal transverse momenta of 6 and 5 GeV/c, respectively and an electron with a p_T of at least 2 GeV/c in one of these jets. The H1-Detector is not capable of triggering jets at such low energies, electron triggers exist for the scattered electron only. Electrons from the semileptonic decay of heavy quarks are, unlike the scattered electron from the ep interaction, not isolated. Triggers for decay electrons in jets are not possible because of the coarse granularity in which the LAr calorimeter is read out by the LAr trigger. In practice such a trigger would probably suffer from high hadron misidentification rates.

The events analysed here have been triggered by the general purpose subtriggers 61 and 83, detecting the scattered electron. The subtrigger 61 uses the SpaCal, see section 2.4.2, giving

	$\mathcal{L}_{\mathbf{int}}$ **1999e$^+$** [**pb^{-1}**]	$\mathcal{L}_{\mathbf{int}}$ **2000** [**pb^{-1}**]
HERA-produced	29.39	70.59
Delivered to H1	27.63	67.89
H1: Physics-ready	23.36	51.54
This analysis: S61	12.78	38.38
This analysis: S83	12.45	38.34
Uncertainty	1.50%	1.45%

Table 3.1: *Integrated luminosities for the run periods used in this analysis. The values given for the subtriggers 61 and 83 are corrected for subtrigger prescales and satellite bunches.*

access to electron scattering angles between 2° and 26°. This corresponds to negative squared four momentum transfers Q^2 of $1 - 100$ GeV^2. This kinematic region is called deep inelastic scattering (DIS).

The scattered electron escapes undetected when scattered under small angles, corresponding to values of $Q^2 < 1$ GeV^2. This is the photoproduction (γp) regime. The electron tagger ET33, see section 2.5, detects electrons scattered under very small angles of less than 5 mrad, corresponding to $Q^2 < 0.01$ GeV^2. This detector is part of the subtrigger 83. The largest fraction of the photoproduction events is not within the acceptance of the electron taggers. Getting access to these data, usually called "untagged photoproduction", would drastically increase the statistics for this and many other analyses.

3.1.1 Subtrigger 61: Deep Inelastic Scattering

The subtrigger 61 is set if a scattered electron candidate is identified in the SpaCal and if at least one track with a transverse momentum of more than 800 MeV/c is detected in the Central Jet Chambers. The latter requirement is fulfilled if the trigger element `DCRPh_THigh` is set. Tracks are reconstructed using 10 wire layers of the CJC. (See [30], [31] for more information on the DCRPhi trigger.) In addition, the proportional chambers CIP, COP and FPC, see section 2.3, have to set the trigger element `zVtx_sig`, indicating the detection of an event vertex within the acceptance of the central tracking detectors ([32], [33]).

The Inclusive Electron Trigger (IET, [34]) fires if an electron candidate is detected in the SpaCal. An energy deposition is considered an electron candidate if the energy sum of 4×4 neighbouring cells in the electromagnetic part of the SpaCal exceeds certain threshold values. Subtrigger 61 uses an inclusive OR combination of these two IET trigger elements:

- `SPCLe_IET` > 2: this trigger element is set if the energy of the electron candidate exceeds 6 GeV. The central region of the SpaCal, close to the beam-pipe, is excluded.

- `SPCLe_IET_Cen_3`: this trigger element is equivalent to the previous except that it covers the central cells of the SpaCal. The energy threshold is set to 6 GeV as well.

A standard electron finder [35] is run offline and quantities like the energy of the scattered electron (E_e), the photon virtuality (Q_e^2) and the inelasticity (y_e) are determined. Additional cuts are applied on the electron candidates in this analysis:

- $E_e > 8$ GeV,
- radial distance of the cluster's barycentre to the beam axis > 9.1 cm,
- $Q_e^2 > 2$ GeV^2,
- $0.05 < y_e < 0.7$,
- $E - p_z > 35$ GeV.

These cuts ensure that the electron candidate is well measured in the SpaCal detector. The remaining contribution of misidentified particles from photoproduction processes is negligible. While E_e, Q_e^2 and y_e are reconstructed from the scattered electron alone, the Hadronic Final State (HFS) is also used to calculate $E - p_z$. The cut on $E - p_z > 35$ GeV means that the total energy of the HFS subtracted by its momentum in the proton flight direction must be larger than 35 GeV. The value of $E - p_z$ should be twice the electron beam energy, 55 GeV. Energy resolution effects smear the distribution, undetected particles and initial state radiation may lead to smaller values than expected. The reconstruction of the Hadronic Final State will be discussed in section 4.

3.1.2 Subtrigger 83: Photoproduction

In the subtrigger 83 similar trigger elements are combined as in subtrigger 61. The requirement of an electron in the SpaCal is replaced by the demand of an energy deposition of $6-9$ GeV (the threshold is variable) in the electron tagger ET33. In addition, as a veto against Bethe-Heitler processes, not more than $5-7$ GeV are allowed in the photon detector. The notation for this trigger element combination is `LU_ET && not LU_PD_low`.

Three tracks with transverse momenta of at least 450 MeV/c each are required such that the trigger element `DCRPh_Tc`, provided by the DCRPhi trigger, is set. In addition, a central vertex is required by asking that `zVtx_sig_1` is set.

The acceptance of the electron tagger depends on the beam optics and on the inelasticity of the event. A minimal acceptance of 10% is assured in all runs by requiring $0.29 < y < 0.65$ with y being measured by the electron tagger.

A reliable energy measurement in the ET33 is obtained by rejecting events in which the electron has hit the tagger in its outer parts: $|x_{ET33}| < 6.5$ cm. Figure 3.1 shows the acceptance of the electron tagger for the runs used in this analysis with the cut on $|x_{ET33}|$ already applied. More information about using the ET33 in analyses can be found in [36] and [37].

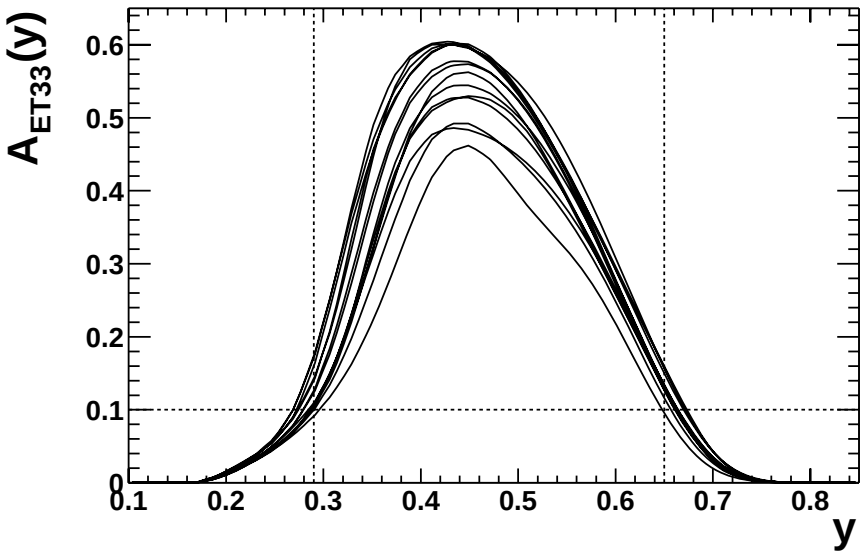

Figure 3.1: *Acceptance of the ET33 in dependence of the inelasticity measured by the ET33. Shown are the data used in the photoproduction analysis. The vertical lines enclose the region of acceptances larger than 10%, indicated by the horizontal line:* $0.29 < y < 0.65$.

3.2 Further Selections

Neither of the two subtriggers has a condition on the second trigger level. However, the events have to pass the 4^{th} trigger level where L4-finders look for certain final states in the detector (see section 2.6). There is no L4-finder (capable of) searching for events with two jets containing an electron. Fortunately, some of the other finders identify parts of the events, so that the selections in DIS and photoproduction do not contain events with weights. The distribution of L4-classes in the final DIS sample is shown in figure 3.2. Prominent contributions come from the classes 11 (Multi-jets), 15 (Open Heavy Quark Production), 19 (Electron in LAr calorimeter), 20 (Electron in SpaCal), 28 (Jets with $E_T > 5$ GeV) and 29 (High W^2) [38].

All events from the nominal run periods with proton positron collisions in the years 1999 and 2000 are fed through the **first preselection:**

- The subtrigger 61 or 83 must be set both on trigger level 1 and 4.
- The quality of the run has to be good or medium.
- The z-position of the primary vertex may not deviate more than 35 cm from the nominal interaction point.
- An event has to contain at least 2 jets. The transverse momentum of one jet must exceed 4 GeV/c. Restrictions on the η range of the jets are not yet applied.

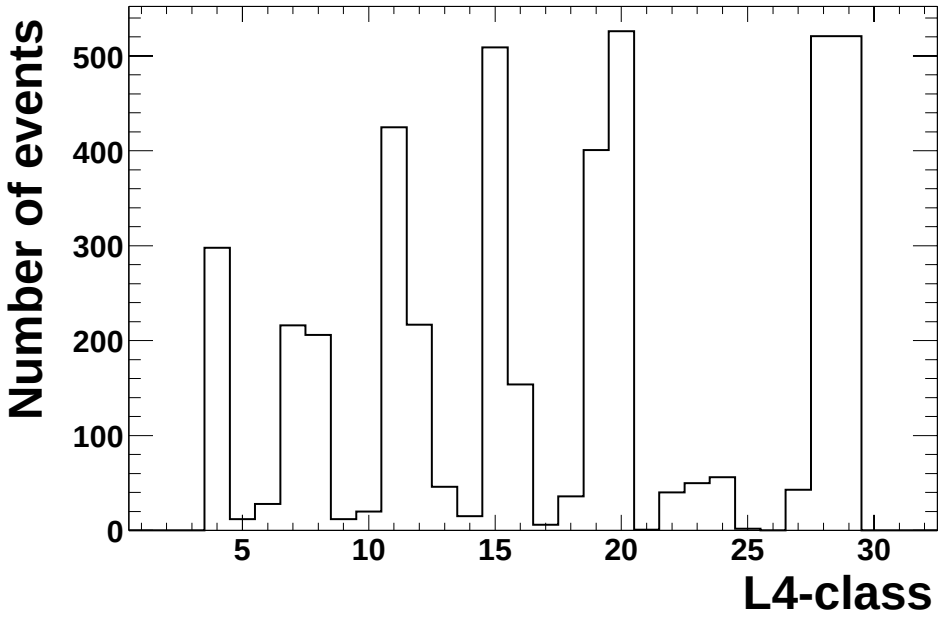

Figure 3.2: *Distribution of L4-classes in the DIS sample. Main contributions come from jet classes (11, 28), electrons (19, 20), heavy quark production (15) and high W^2 (29).*

The selection is applied on H1 data ([26], [39], [40]). All jets, both on these data files and those constructed in this analysis, see section 4, are created with the inclusive k_T-algorithm in the p_T-weighted scheme [41].

All further operations like the reconstruction of the Hadronic Final State or the study of systematic effects is performed in this selection.

About 3.5% of all events pass this selection as can be seen from table 3.2 listing numbers of events for the different data samples before and after the selections. The DIS sample (S61) and the photoproduction sample (S83) are treated separately.

After reconstructing the Hadronic Final State using the algorithm developed in section 4, events are selected which pass the **second preselection:**

- At least two jets must be found with $|\eta| < 2.5$.
- The transverse momenta of these jets must be larger than 5 and 4 GeV/c, respectively.
- A track reconstructed in the CJC with $p_T > 2$ GeV/c has to be present within one of these jets.

The cuts on the transverse momenta of the jets are raised to 6 and 5 GeV/c for the final analysis. The complete event selection will be summarised in table 8.1.

Events	**1999e$^+$: S61**	**1999e$^+$: S83**	**2000: S61**	**2000: S83**
Total	24,635,713		58,757,139	
First Preselection	321,081	352,492	1,039,464	1,200,750
Second Preselection	66,952	66,875	223,400	240,208

Table 3.2: *Overview of data sets: the total number of events for a run period is given in the first line. The number of events remaining after requiring the respective trigger and two jets (see text) are listed in the second line. The third line shows the events selected after the reconstruction of the Hadronic Final State, described in chapter 4. Here, two jets within an η range of $|\eta| < 2.5$ are required. One of them has to contain a track with a transverse momentum of more than* 2 GeV/c.

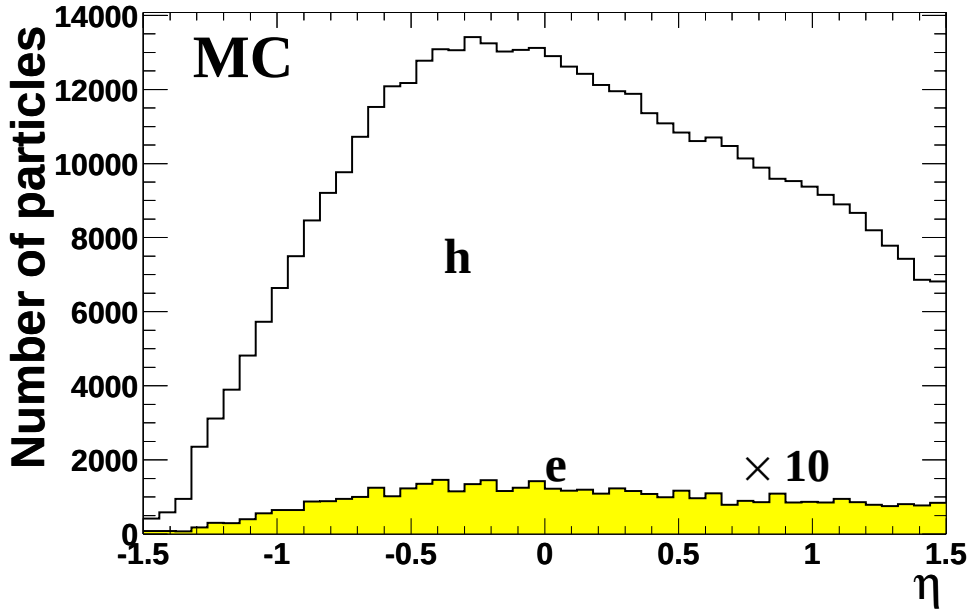

Figure 3.3: *The η distribution of tracks with transverse momenta larger than* 2 GeV/c *in a Monte Carlo simulation (listed in line 6 of table 3.3). The contribution from hadrons is shown as a solid line, the shaded area represents the contribution from electrons, scaled by a factor 10. The electrons fraction is approximately 1%, see also table 6.1.*

The number of events passing this selection are listed in the third line of table 3.2. By looking at the ratio of electrons to hadrons for tracks with $p_T > 2$ GeV/c in a Monte Carlo simulation (listed in line 6 of table 3.3) it becomes clear that it is not justified to speak of these tracks as "electron candidates" since the electron fraction in this sample is only about 1%. The η distribution for these tracks is shown in figure 3.3, the contribution from hadrons is shown as a solid line. The shaded area indicating the contribution from electrons has been scaled up by a

factor 10 to make it visible. The development of an electron identification algorithm leading to electron selection purities larger than 80% is presented in the chapters 5 and 6.

3.3 Monte Carlo Simulations

Monte Carlo simulations used in the H1-Experiment consist of three independent steps: the generation of the events according to physics theories and models, the simulation of the detector response of these events by the use of proper detector descriptions and the reconstruction of charged and neutral particles using the same software as for data.

The energy distribution of electromagnetic and hadronic calorimeter showers has been largely studied using single particle Monte Carlo simulations. The calorimeter response of electromagnetic showers is modeled using the H1FAST shower parameterisation [42], see also section 5.4. The numbers of electrons and pions from single particle simulations are listed in the first two rows of table 3.3. The differences of electromagnetic and hadronic showers and their possible exploitation for the identification of electrons are discussed in chapter 5.

	MC Generator	**Selection**	**Events**	$\mathbf{Q^2}$ **[GeV^2]**	$\mathcal{L}_{\mathbf{int}}$ **[pb^{-1}]**
1	single particle (H1SIM)	Electrons	73,000	–	–
2	single particle (H1SIM)	Pions	546,000	–	–
3	PYTHIA (inclusive)	Beauty	1,386,148	$]0,1[$	4870.00
4	PYTHIA (inclusive)	Charm	1,924,300	$]0,1[$	2349.02
5	PYTHIA (inclusive)	Light Flavours	306,990	$]0,1[$	1238.67
6	PYTHIA (inclusive)	All Flavours	11,318,056	$]0,100]$	88.76
7	RAPGAP (direct)	Beauty	898,318	$[1.5,110]$	45346.63
8	RAPGAP (direct)	Charm	1,134,188	$[1.5,110]$	19025.40
9	RAPGAP (direct)	Light Flavours	868,778	$[1.5,110]$	86.68
10	CASCADE	Beauty	1,149,931	$]0,110]$	4025.98
11	CASCADE	Charm	921,344	$]0,110]$	1008.85

Table 3.3: *Summary of Monte Carlo simulations used in this analysis. Two jets were required in an event in case of the PYTHIA and RAPGAP Monte Carlo generators. A generated electron with a transverse momentum larger than* 1.9 GeV/c *was required for charm and beauty sets. In the PYTHIA simulation containing both light and heavy flavours an event was accepted if at least one particle with a transverse momentum larger than* 1.5 GeV/c *was generated. To study the effect of photon conversion into an electron positron pair a generated photon with* $p_T > 1.9$ GeV/c *was required in case of the RAPGAP light flavour simulation.*

Monte Carlo simulations using the generators PYTHIA ([14]), version 6.1, RAPGAP ([15]), version 3.1, and CASCADE ([21], [22]), version 1.00, are used for the description of physics distributions of signal and background processes such as the relative transverse momentum of the decay lepton to the quark jet (see section 7.1 for more details on $p_{T,rel}$). They are

used as well for the determination of reconstruction efficiencies (section 8.3) and systematic uncertainties (section 8.4).

The generator PYTHIA was used in its inclusive mode, producing direct, 'normal' resolved and flavour excitation events.
With RAPGAP which is only used for the DIS analysis, only direct processes were generated. The program HERACLES ([43]) which simulates initial state radiation is interfaced with the RAPGAP event generator.
CASCADE is used as a cross-check to the other generators as it implements the CCFM ([18], [19], [20]) evolution in contrast to DGLAP ([16], [17]).
The fragmentation of light quarks uses Lund fragmentation ([24]) in all simulations. Heavy Quark fragmentation is performed via the Peterson fragmentation function ([23]).

Several important properties of the Monte Carlo simulations have been checked in the course of an analysis of the semileptonic decay of beauty hadrons into muons ([8]). It was for example made sure that the branching ratios of the semileptonic decays as implemented by JETSET ([14]) are in agreement with the world averages.

Simulations of heavy flavour signal events have been done with all three generators, PYTHIA and CASCADE in the photoproduction regime and RAPGAP and CASCADE in case of DIS. In the generation step, an electron was required within the acceptance of the Central Jet Chambers having a transverse momentum larger than 1.9 GeV/c. Two jets with transverse momenta larger than 4 GeV/c were required as well in case of PYTHIA and RAPGAP simulations. These data sets are listed with 'Beauty' or 'Charm' in the second column of table 3.3; they form the Monte Carlo signal sets.

Simulations of background events have been performed equivalently to the signal sets. Events are considered as background if electrons stem from the decay of light quark mesons such as π^0 or η or if the electron has been created in a photon conversion process, $\gamma \rightarrow e^+e^-$, or if hadrons are falsely identified as electrons. Three kinds of simulations have been carried out to study the individual background contributions:

- $uds \rightarrow e$, with $p_T(e) > 1.9$ GeV/c,
- $uds \rightarrow \gamma$, with $p_T(\gamma) > 1.9$ GeV/c,
- $udscb \rightarrow$ any charged particle with $p_T > 1.5$ GeV/c.

The contribution of light quark decays to the final data sample is unmeasurably small as will be shown in section 7.1. The reason is the suppression of decays of pions and kaons into electrons compared to muons due to the $V - A$-coupling of the weak interaction.

The background from pair production processes via photon conversion on the other hand is large. The corresponding Monte Carlo simulation, the second sample in the listing above, has been generated such that an event has to contain a photon from a light quark decay

with a transverse momentum larger than 1.9 GeV/c. The photon conversion itself cannot be asked for in the Monte Carlo generation because this happens in the detector simulation step.

In case of the third simulation, $udscb \rightarrow$ any charged particle, it has only been required that a charged particle with $p_T(charged\ particle) > 1.5$ GeV/c and two jets with transverse momenta larger than 4 GeV/c were generated. Both light and heavy flavours were simulated. Figure 3.3 shown in the previous section was produced using this simulation. It is the standard set for tests of the electron identification and hadron misidentification in this analysis.

Chapter 4

Hadronic Final State

The definition of the Hadronic Final State (HFS) and the requirements on the HFS in this analysis will be discussed first in this chapter. It will be followed by a description of the newly developed association of tracks and calorimeter cells. Finally, the construction of jets will be discussed.

4.1 Definition and Requirements

The Hadronic Final State is usually defined as the set of all particles found in an event, excluding the scattered electron if it has been reconstructed and identified. The Hadronic Final State may be used to calculate event kinematics and it is the basis for the construction of jets.

The energy of particles can be measured by tracks (charged particles) and with the calorimeter. For the analysis of the Hadronic Final State, tracks and calorimeter energy have to be correlated by associating the tracks with energy measured in the calorimeter cells.

The association of tracks measured in the tracking chambers with energy depositions in the calorimeters has to be performed such that energy is not counted twice or omitted. This is usually achieved by "locking" energy depositions in the calorimeter once they have been assigned to tracks. Other tracks may thus not be matched to locked cells/clusters. As a consequence, the association of tracks and calorimeter energy depends on the order in which the tracks are considered.
Energy carried away by neutrinos is of course lost as are the contributions from very low momentum particles.

The separation of energy depositions by electrons in the LAr calorimeter from those of the surrounding hadrons in the jets is especially important for this analysis: electrons are identified by the shape of their clusters (chapters 5 and 6). In addition, the jet momenta have to be well measured because the transverse momentum of an electron relative to the jet axis is used to determine the fraction of electrons from beauty production.

Neither of the two standard HFS reconstruction algorithms used at the H1-Experiment, FSCOMB ([44]) and HADROO2 ([45]), meets all of the mentioned criteria since they have been

developed for the analysis of jets and not for particle identification. An alternative algorithm is presented in the following sections.

4.2 Track Cell Association

The combination of tracks measured in the tracking chambers with energy depositions in the calorimeter is described in this section. The output of the algorithm is a set of "HFS particles".

The initial preparation is the following:

1. Only energy depositions from the LAr or the SpaCal are accepted.
2. Noise suppression is applied:
   - Clusters, as defined by the H1 calorimeter reconstruction, have to consist of at least two cells.
   - The absolute energy of a cluster on the electromagnetic scale has to be larger than 200 MeV.
3. Clusters are split into individual cells.
4. All tracks measured in the CJC which are fitted to a vertex[1] with transverse momenta larger than 0.12 GeV/c and radial track lengths larger than 10 cm are extrapolated to their impact point on a calorimeter surface.

The actual track cell assignment is performed in the next step with special search algorithms described in section 4.2.2. HFS particles are being created based on tracks. Each cell has a weight which is initialized to zero. Every track assigning the cell to itself increases the cell's weight by one. The cell's energy is later on divided by its weight when quantities like the sum of the cell energies are calculated. The procedure for the track cell association is:

1. A loop over all selected tracks is performed.
2. Cells within a $4^\circ \times 4^\circ$ window ($10^\circ \times 10^\circ$ for cells in the hadronic section) around a track's impact point are selected. Their weight is increased for every track associating the cells.
3. A second search is performed using a $4^\circ \times 4^\circ$ ($10^\circ \times 10^\circ$) window around all cells found in step 2. The weights are updated accordingly.
4. Step 3 is repeated iteratively using a $2^\circ \times 2^\circ$ window until no further cells are found. The weights are updated accordingly. (This iteration is not done for cells in the hadronic calorimeter.)
5. Remaining cells are merged to neutral clusters using a $20^\circ \times 20^\circ$ search window. An iterative procedure is not performed.

[1] If a track is fitted to the primary vertex and to one or more secondary vertices, the former track hypothesis is taken.

This algorithm has the feature that its output is independent of the order in which tracks and cells are associated. This is not the case for the standard algorithms as has been mentioned before.

Three different types of Hadronic Final State particles are distinguished:

- tracks with associated cells (tracks with clusters),
- tracks which have no cells assigned,
- cells without track assignment (neutral clusters).

Clusters may consist of electromagnetic and hadronic cells. The energy fraction in the hadronic calorimeter is denoted with f_{HAD}.

The initial extrapolation windows are small compared to the standard algorithms. Still, energy depositions by two very close tracks are not properly separated when weights are *not* used. This issue is demonstrated in figure 4.1 where the ratio of the energy reconstructed in the calorimeter, E, and the particle's momentum, p, is shown for electrons in a Monte Carlo simulation. The value E/p should be close to one for electrons, see section 5.1.

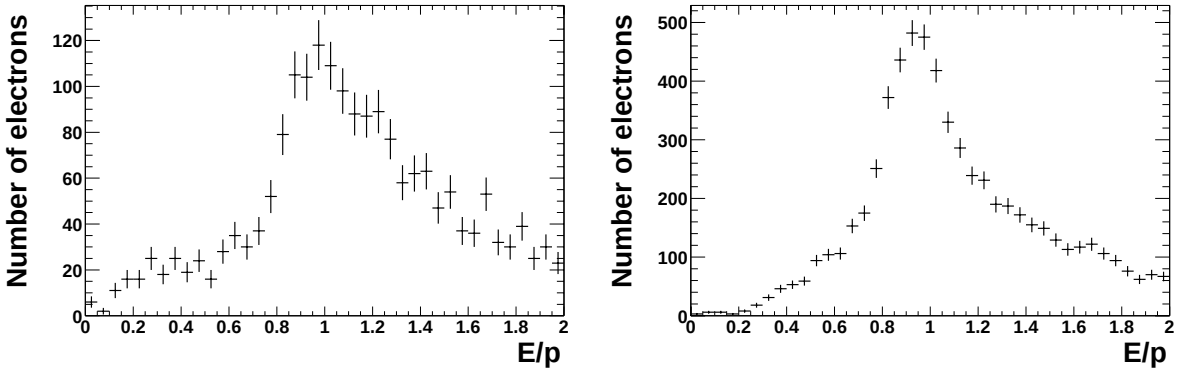

Figure 4.1: *E/p for electrons from a Monte Carlo simulation in which nearly all electrons are produced in photon conversion processes. The left plot shows the E/p distribution obtained by a version of the HFS algorithm presented in this section where cells are locked instead of weighted. The right plot shows the distribution obtained from the regular algorithm as described in the text.*

Almost all electrons in this simulation are created in pair production processes by photon conversion. Thus, an electron positron pair emerges under a small opening angle, which then leads to the development of close or overlapping showers. The values for E/p are shown on the left side of the figure before the introduction of weights. The distribution is very broad and shows long tails. Electrons assigning energy from the other track to themselves contribute to large E/p values. These cells are locked and may not be assigned by the second track. This leads to many electrons with E/p values much smaller or much larger than one.

It has been tried to overcome this problem by alternative strategies:

- step 2 is done for each track before steps 3 and 4 are performed without introducing weights or
- the initial search window is set to, for example, 30-50% of the distance between two close tracks.

Both strategies suffer from their dependence on the track ordering and that cells locked to one track are inaccessible for the other. This problem has been largely solved by the introduction of weights as is shown on the right side of figure 4.1. Cells associated to tracks are not locked and thus may be taken by other tracks as well. As a result, more electron tracks have calorimeter cells assigned and the E/p distribution becomes less broad. The initial extrapolation windows still have to be as small as possible in order not to assign other particles' energy depositions. The problem of overlapping showers of charged and neutral particles, such as photons, cannot be addressed in similar ways. So, broad E/p distributions are still observed (compare for example the right plot of figure 4.1 with figure 4.2). The separation of neutral clusters can probably only be performed if the detector is instrumented with a pre-shower detector or if the longitudinal segmentation is about 10 times larger than in the H1-Detector as is e. g. proposed for a possible TESLA-Detector ([46]).

4.2.1 Kinematical Validation

In this section it will be shown that both individual particle properties and event kinematics are well reconstructed by the HFS algorithm presented in the previous section.

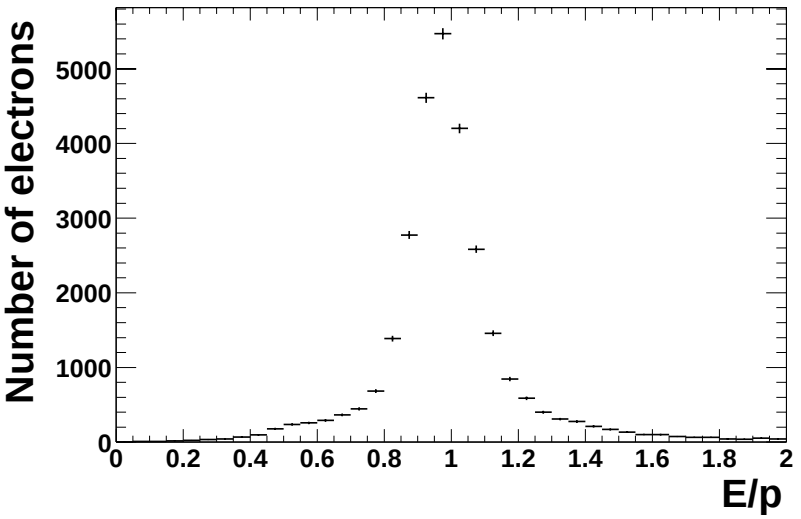

Figure 4.2: *E/p distribution for electrons in a beauty production Monte Carlo simulation. All electrons have transverse momenta of at least* 2 GeV/c.

The E/p distribution obtained for electrons with transverse momenta of at least 2 GeV/c in a beauty production Monte Carlo simulation is shown in figure 4.2. Its mean value is close to one and the shape is narrow and symmetric.

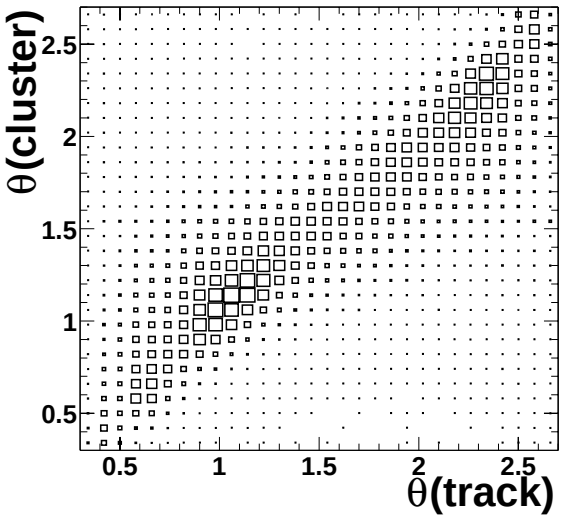

Figure 4.3: *The angle ϑ of the reconstructed cluster axis is plotted vs. ϑ as measured for the track by the tracking chamber. The position of the primary vertex is not used for the determination of the cluster's ϑ value, only the positions of the energy depositions in the cluster are considered.*

The direction of flight of a particle measured by the tracking chamber is compared with that reconstructed by its associated cells in the LAr calorimeter. The construction of the cluster axis is discussed in section 5.3. The ϑ value of the cluster is determined using this cluster axis alone; the vertex position is *not* taken into account. In figure 4.3 the ϑ value of the cluster axis is plotted vs. the track's ϑ and a good correlation is observed. A perfect match cannot be expected, e. g. because of multiple scattering at the calorimeter surface and within the calorimeter. It should nevertheless be noted that the calorimeter cells used for determination of the cluster axis have been chosen to be in a $\vartheta - \varphi$-window around the track. The correlation is however a clear indication that the iterative search for neighbouring cells, step 4 in the HFS algorithm, does not lead to uncontrolled growth of the clusters.

The ratio of the total reconstructed energy per event to the generated energy in the central detector region, $30° < \vartheta < 155°$, is plotted in figure 4.4. Energy contributions from neutrinos and from low momentum particles with $p_T < 0.12$ GeV/c are excluded from the energy sums. The central value is at 1.01, the standard deviation of the distribution is 0.13. This proves that as much energy is reconstructed in the detector as is generated. The question of LAr calorimeter calibration will be discussed in section 8.4.

It can be demonstrated that the overall kinematics reconstruction succeeds as well. The inelasticity y of the interaction can be determined either from the energy of the scattered electron

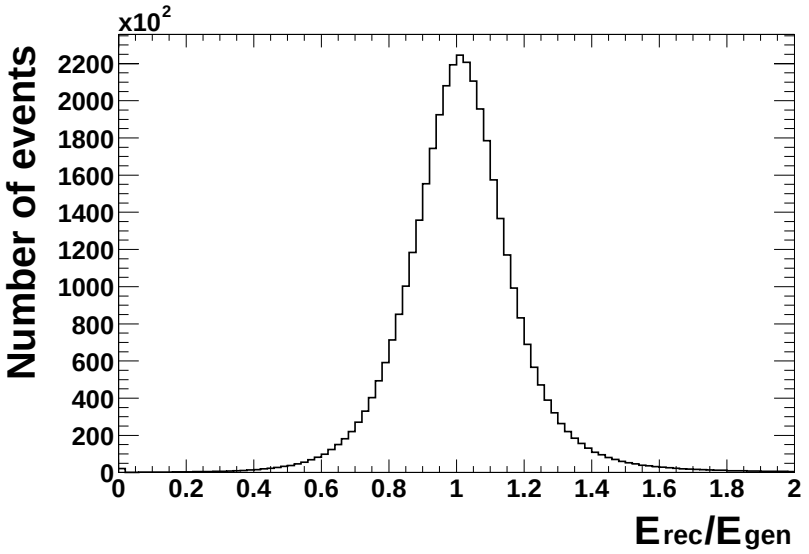

Figure 4.4: *Reconstructed energy in the Hadronic Final State divided by the generated energy for particles reconstructed in the central part of the H1 detector,* $30° < \vartheta < 155°$. *Energy contributions from neutrinos are excluded from the sum over generated particles. All particles with* $p_T < 0.12$ GeV/c *are ignored for both energy sums. The mean is at 1.03, the standard deviation is 0.13.*

or from the Hadronic Final State ([47]). For the electron it is defined as $y = 1 - E'_e/E_e$ with E_e being the initial energy of the electron and E'_e being its energy after the interaction. The reconstruction of y via the Hadronic Final State is defined as $y = \frac{E-p_z}{2 \cdot E_e}$. E is the energy component of the fourvector of the Hadronic Final State, p_z is its momentum's z-component. Figure 4.5 shows the generated y distribution from the Monte Carlo simulation (dashed line), from the standard Hadronic Final State HADROO2 (dotted line) and from this algorithm (solid line). The generated value of y is well reconstructed in the central region of $0.15 \leq y \leq 0.6$.

4.2.2 Technical Aspects of Efficient Track Cell Assignment

A data structure suitable for a track cell assignment as introduced in the previous section has to meet various requirements. It has to be possible to operate on several million events, each containing 10 tracks and 300 cells on average. The most important requirements are therefore:

- Speed allowing many searches to be performed.
- Efficiency: a lot of information is needed for every track and every cell, tracks have to maintain lists of cells associated and *vice versa*.
- It has to be extendible to allow for possible future work.

Sufficient speed is achieved by keeping the data structures as small as possible and by choosing appropriate search algorithms. Here, the range search method, described in the next section,

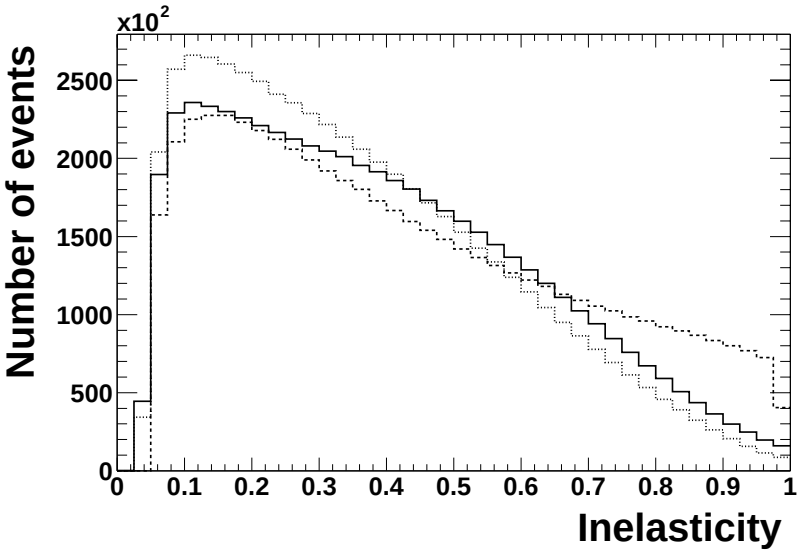

Figure 4.5: *The inelasticity in a Monte Carlo simulation. The dashed line shows the generated y distribution. It is compared with the reconstruction of y using the standard H1 Hadronic Final State HADROO2 (dotted line) and the inelasticity calculated from the HFS used in this analysis (solid line).*

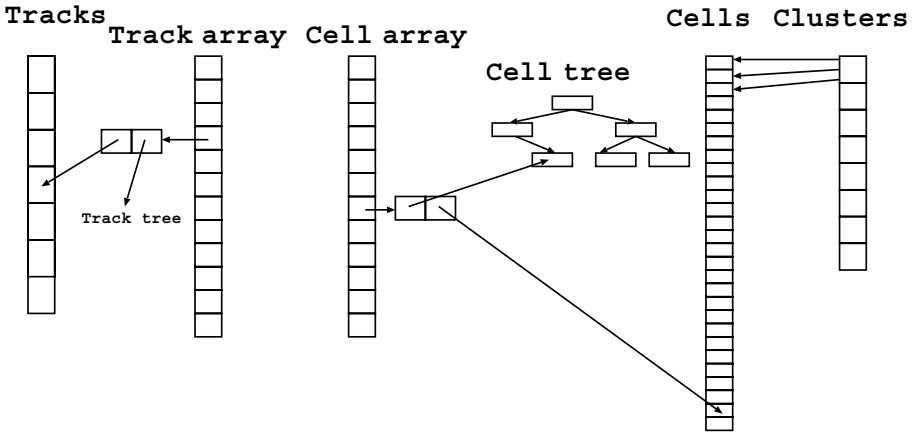

Figure 4.6: *Overview of arrays and binary trees used for the track cell assignment. Tracks (on the left) and clusters, cells (on the right) are unmodified arrays of official H1 data. Additional lists and trees are constructed in between, connected by pointers. Not shown: the track tree holds equivalent information as the cell tree. Every track tree node contains an array with indices of assigned cells.*

is used. Its execution time scales with the logarithm of the number of entries N in a search tree: $T \propto (R + \log(N))$, with R being a constant. (It has to be noticed that the theoretically

calculated scaling with N of an algorithm corresponds only to the lower limit of the execution time in the actual implementation. In reality, the nodes in a search tree require space and therefore compete with each other and with other parts of the program for space in the processor's cache. Thus, small data structures are desirable.). In addition, hash lists are used where random lookups are needed, e. g. in the maintenance of tracks matched to a cell. Simple arrays are taken when only sequential reading is required, as is the case for cells being assigned to a track.

The data structure used here is illustrated in figure 4.6: the basic properties of tracks and cells are kept in arrays on official H1 data sources. All information relevant for the track cell association process is accessible through binary trees. The tracks and cells are connected with the respective trees via arrays (denoted with "Track array" and "Cell array" in figure 4.6) containing pointers to a tree node and a track/cell. The impact points of the tracks extrapolated to the calorimeter entrance are available in the tree nodes as well as lists indicating which cells have been assigned to a track and which tracks point to a cell. Figure 4.7 shows the cell tree in some more detail. The tree holding the track nodes has a similar but smaller structure.

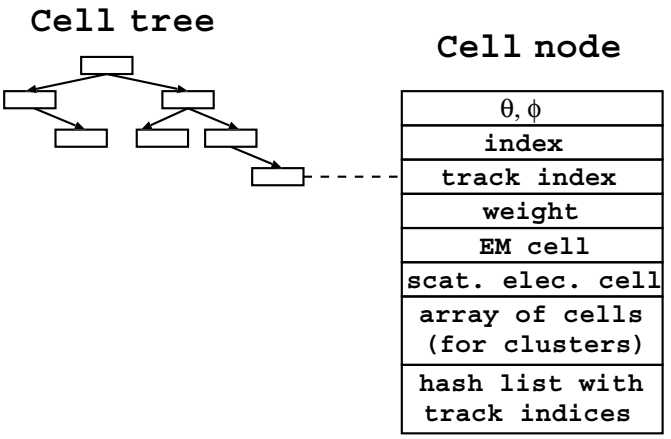

Figure 4.7: *Binary tree holding cell nodes. Each node contains characterising information, such as the cell's ϑ and φ values, as well as technical information, e. g. the indices of tracks having assigned the cell are stored in a hash list.*

4.2.3 The Range Search Algorithm

The range search algorithm described in [48] is used to quickly match positions of calorimeter cells to given $\vartheta - \varphi$-windows around extrapolated tracks. The search time T scales logarithmically with the number of entries N: $T \propto (R + \log(N))$.

The binary trees holding the positions of electromagnetic and hadronic cells have to be set up once per event, making a loop over all cells necessary. All subsequent searches for matching cells access these trees, leading to a large gain in time compared to ordinary loops.

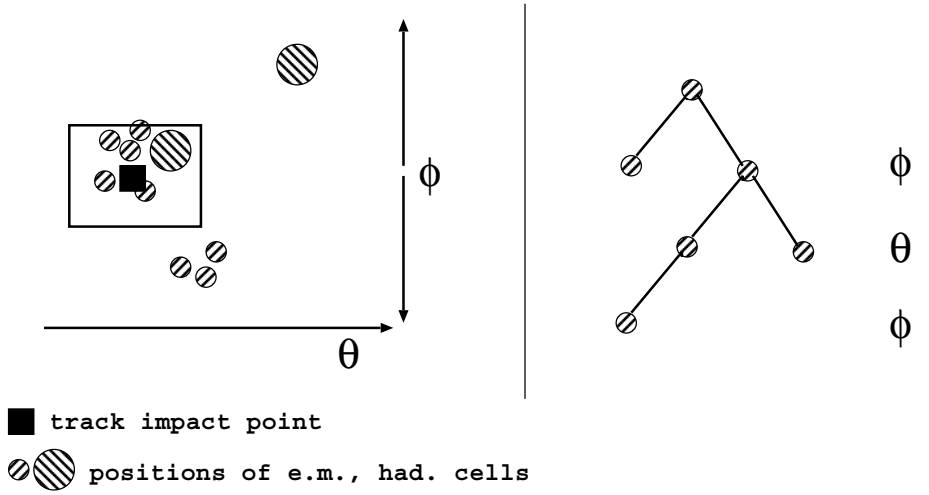

Figure 4.8: Left: *Visualisation of the arrangement of electromagnetic and hadronic cell positions (small and large circles) and positions of extrapolated tracks (black box) in the $\vartheta - \varphi$-plane. The rectangle around the track's position indicates the area selected by a range search.* Right: *Example of how electromagnetic cell positions are stored in a binary tree. The first cell is taken as the top node. It has two daughter nodes: one for cells with smaller φ-positions and one for cells with larger φ-positions. Cells sort according to ϑ in the next layer. Positions of hadronic cells are stored in a separate tree.*

The creation of a binary tree for a range search is illustrated in figure 4.8. The first cell entering the tree becomes the top node. The φ-position of the second cell is compared to that of the top node. If it is larger, the cell is set up as the first daughter node on the right side, otherwise on the left. A comparison of the φ-value is done for the third cell as well. If it is larger than that of the top node, its ϑ-position is compared to that of the daughter node on the right side. In the next layer, the comparison is again performed against the φ-positions and so on.

Searching for matching cells works equivalently: if the φ-position of one boundary of the search rectangle is at larger values than the top node, the other side of the tree is excluded from this search. In an approximately balanced tree, about half of the cells are discarded by one comparison.

The extrapolation windows are rectangles in the $\vartheta - \varphi$-plane. Although circular windows, possibly even taking the local cell granularity into account, would be preferable, the chosen layout does not lead to inefficiencies because of the iterative nature of the track cell association.

If the presented HFS algorithm were to be adapted to future experiments with many more calorimeter cells, switching from simple binary trees to balanced binary trees ([49]) may lead to additional performance improvements.

4.3 Construction of Jets

Jets are an indication for fragmentation and hadronisation of quarks and gluons. They are defined using jet construction algorithms which group charged and neutral particles in narrow cones, allowing for a reconstruction of the kinematics of the quarks in the hard interaction. Jet algorithms should be infrared safe (two collinear particles can be replaced by one particle) as well as insensitive to soft particles.
At least two jets are expected in the leading order picture of heavy quark production by boson gluon fusion at HERA, see section 1.2.

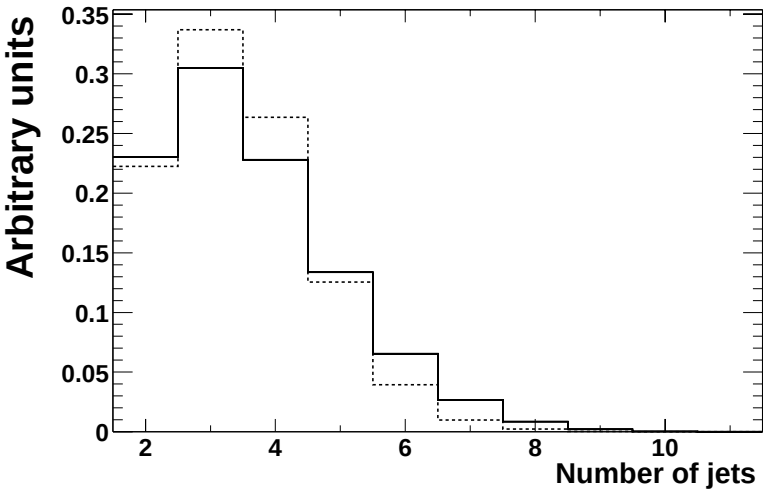

Figure 4.9: *Number of jets per event for Monte Carlo simulations of beauty production. The solid line represents a PYTHIA simulation, the dashed line a CASCADE simulation. At least two jets were required in all events. Both distributions are normalised to the total number of events.*

Input particles for the jet construction are the particles of the Hadronic Final State. The inclusive k_T-algorithm in the p_T-weighted scheme [41] is used, with a minimal transverse momentum of 2.5 GeV/c per jet. The k_T-algorithm is an iterative procedure in which particles have distances $d_i = p^2_{T,i}$ assigned to the beam axis as well as pairwise to each other, $d_{ij} = \min(p^2_{T,i}, p^2_{T,j})R_{ij}/R$. R is a separation parameter and chosen to be 1, R_{ij} is the distance between two particles in the $\eta - \varphi$-plane: $R_{ij} = \sqrt{(\eta_i - \eta_j)^2 + (\varphi_i - \varphi_j)^2}$. Particles are grouped together as long as the pairwise distance d_{ij} is smaller than the distance to the beam axis. Otherwise, they are added to the list of jets.

The effects of different theoretical models on jet production can be seen in figure 4.9. The number of jets per event predicted by a PYTHIA Monte Carlo simulation for beauty production (solid line) is compared with a CASCADE simulation (dashed line). The CCFM-based CASCADE simulation clearly contains more 3-jet-events than PYTHIA, implementing DGLAP.

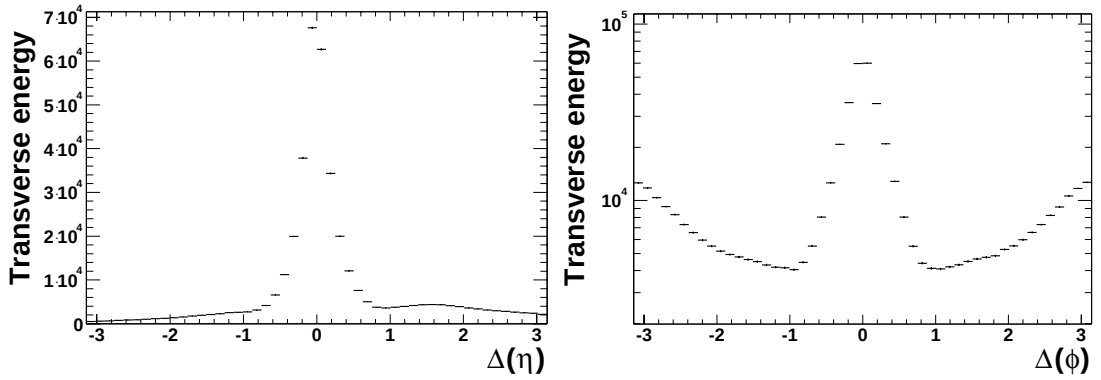

Figure 4.10: *Jet profile histograms for photoproduction data.* Left: *η-profile. The distance* $\Delta(\eta)$ *between the particles in an event to the highest* p_T *jet is shown. The particles must have a distance difference* $\Delta(\varphi) < 1$ *to this jet.* Right: *φ-profile. The distance* $\Delta(\varphi)$ *between the particles in an event to the highest* p_T *jet is shown. The particles must have a distance difference* $\Delta(\eta) < 1$ *to this jet.*

The dijet structure of photoproduction events can be seen from figure 4.10. At least two jets were required for events to pass the selection, see section 3.2. Two jet profile histograms are shown: on the left side, the distance $\Delta(\eta)$ between the jet with the highest transverse momentum and all particles in the event is plotted, if the distance $\Delta(\varphi)$ from the jet to the particle is smaller than one. The equivalent φ-profile is shown on the right side of the figure.

Chapter 5

Shower Development in the Calorimeter

The discrimination of electrons and hadrons based on differences in their energy depositions in the calorimeter requires the choice of parameters with good separation power. It is however, especially in the energy regime of a few GeV, not a priori clear which parameters should be chosen.

A short overview of relevant processes in calorimeters will be given first in this chapter. It is followed by a presentation of the shower shape parameters used in the analysis. Finally, the shower shape parameters for electrons and pions are compared between data and simulations.

5.1 Properties of Electromagnetic and Hadronic Showers

The almost exclusive source of energy loss in a calorimeter for electrons with energies of more than 100 MeV is bremsstrahlung. Photons are continuously radiated off and deposit their energies after having traveled 9/7 radiation lengths on average, preferably via pair production of an electron and a positron. These particles may as well radiate photons before being absorbed/annihilated. In the case of positron annihilation, two new photons emerge. This is the way the electromagnetic cascade develops. The shower maximum is reached when the average energy of a photon or electron/positron has decreased to a level where most energy is lost via Compton scattering, photoelectric effect or ionisation.

The showers of electrons are narrow and homogeneous, their lateral spread is determined by multiple scattering of electrons/positrons in the early phase of the shower development and by isotropic processes like Compton scattering after the shower maximum has been reached.

This behaviour is just the opposite to the 'erratic' nature of hadronic showers. Reactions involving the strong interaction lead to a variety of possible processes. The energy needed for the release of nucleons, the nuclear binding energy, is undetectable and lost for calorimetry. In addition, energy may be carried away by muons or neutrinos or is only released late by the de-excitation of nuclei. All of this leads to a ratio $e/\pi > 1$, meaning that the detectable energy of an electron shower is always larger than that of a hadron shower. Figures 5.1 and 5.2 show

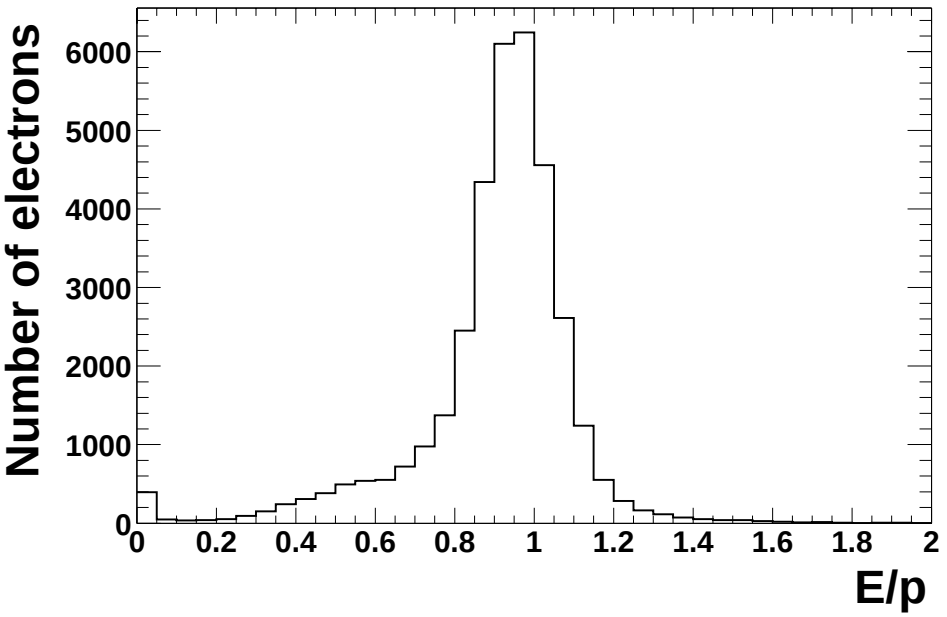

Figure 5.1: *E/p, the energy reconstructed in the calorimeter divided by the track momentum, for electrons in a single particle Monte Carlo simulation. The width of the peak is dominated by the resolution of the electromagnetic calorimeter, the tail to the left is caused by dead material effects as well as radiation of photons before the calorimeter is reached.*

the energy depositions in the LAr calorimeter divided by the track momenta according to single particle Monte Carlo simulations of electrons and charged pions. All particles have transverse momenta larger than 2 GeV/c. Almost all of the electron energy is detected in the calorimeter: $E/p \approx 1$. Only 40 – 80% of the hadrons' energy is visible in the detector.

A hadronic shower has an electromagnetic component which is initiated by electromagnetically decaying mesons like π^0s or ηs which are being produced in the hadronic cascade. These particles decay mostly into two photons which then start the electromagnetic shower. Its energy fraction can grow as more and more π^0-mesons are produced. The total energy fraction of the electromagnetic sub-shower may reach nearly 100% for special processes like $\pi^+ n \rightarrow \pi^0 p$ where the π^0-meson gets nearly all kinetic energy available and only very little energy is lost due to the capture of the (slow) proton.

The lateral extension of hadronic showers is composed of a narrow cone, originating from the electromagnetic component, and an irregular halo with radially exponentially decreasing energy.

A comprehensive discussion of calorimetry can be found in [50].

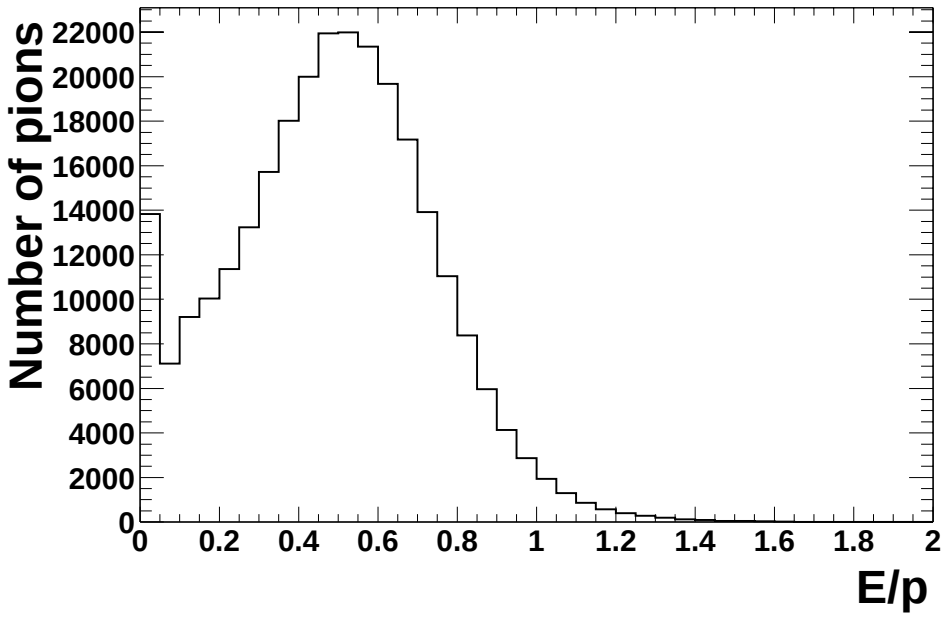

Figure 5.2: *E/p for charged pions in a single particle Monte Carlo simulation. For most pions, only 40-80% of the energy is seen in the electromagnetic and hadronic LAr calorimeter.*

5.2 Longitudinal Energy Distribution

With the cuts listed in table 5.1, approximately 90% of all hadrons are rejected while most electrons are kept (see also figures 5.1 and 5.2). Hadrons surviving these cuts have a large electromagnetic component and are therefore more "electron-like" than the average hadron.

Energy on e.m. scale in the LAr calorimeter over track momentum	$0.8 < E/p < 1.2$
Fraction of energy in the hadronic calorimeter	$f_{HAD} = 0$

Table 5.1: *Initial requirements for all particles. Most electrons pass these cuts while the majority of hadrons is rejected.*

The continuous energy loss of electrons through bremsstrahlung leads to large energy depositions close to the calorimeter entrance. Hadrons, in contrast, deposit their energy sporadically over a longitudinally extended region in the calorimeter. The electromagnetic sub-shower starts later in the calorimeter when compared with electrons because a photon travels 9/7 radiation lengths on average before depositing its energy.

The parameter λ has been chosen to measure the longitudinal energy deposition

$$\lambda = \frac{\sum_{i=1}^{3} E_i \cdot i}{\sum_{i=1}^{3} E_i} \; . \tag{5.1}$$

The index i is the number of the electromagnetic layer, with $i = 1$ being the innermost one.

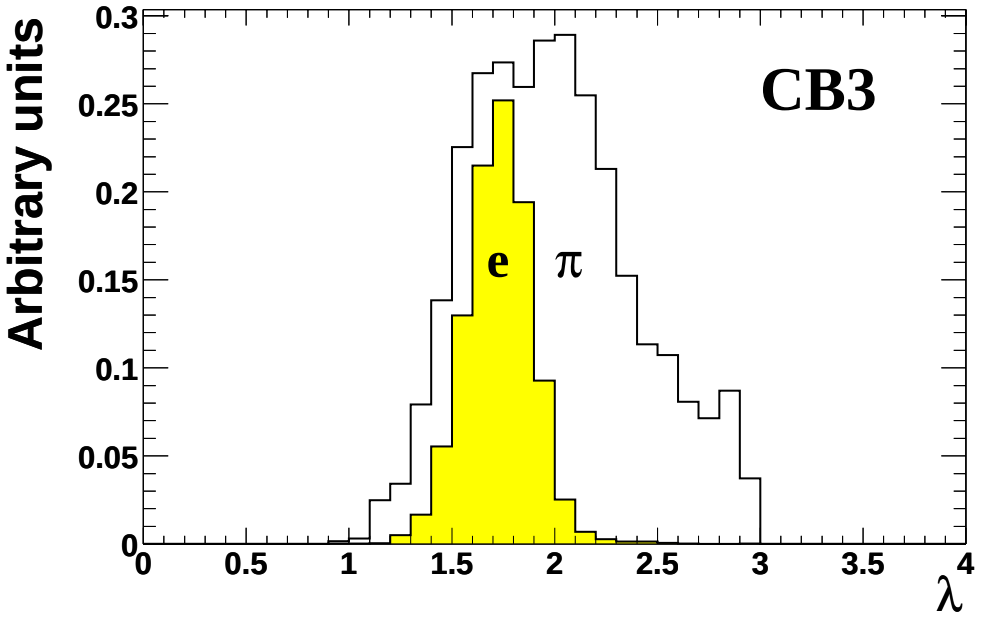

Figure 5.3: *The longitudinal energy deposition λ in the calorimeter wheel CB3: pions are shown in the white, electrons are shown in the shaded histogram. Both distributions have been obtained with single particle Monte Carlo simulations. Only particles fulfilling the requirements from table 5.1 are shown.*

In figure 5.3 the parameter λ is shown for electrons (white histogram) and pions (shaded histogram) in the 4^{th} LAr calorimeter wheel (*CB3* in figure 2.4). All particles have to pass the requirements listed in table 5.1. The electrons' distribution peaks around a value of 1.6 indicating that almost all their energy is being deposited in the first two electromagnetic layers and very little in the last layer. The longitudinal energy deposition for hadrons is more extended, leading to larger values of λ and to a broad distribution.

The effects of the preselection introduced in table 5.1 on the shower shape can be seen from figure 5.4. Pions without the restrictions $0.8 < E/p < 1.2$ and $f_{HAD} = 0$ (white histogram) are compared to those surviving these cuts (shaded histogram). The latter distribution, scaled by a factor 15, is clearly shifted towards smaller λ.

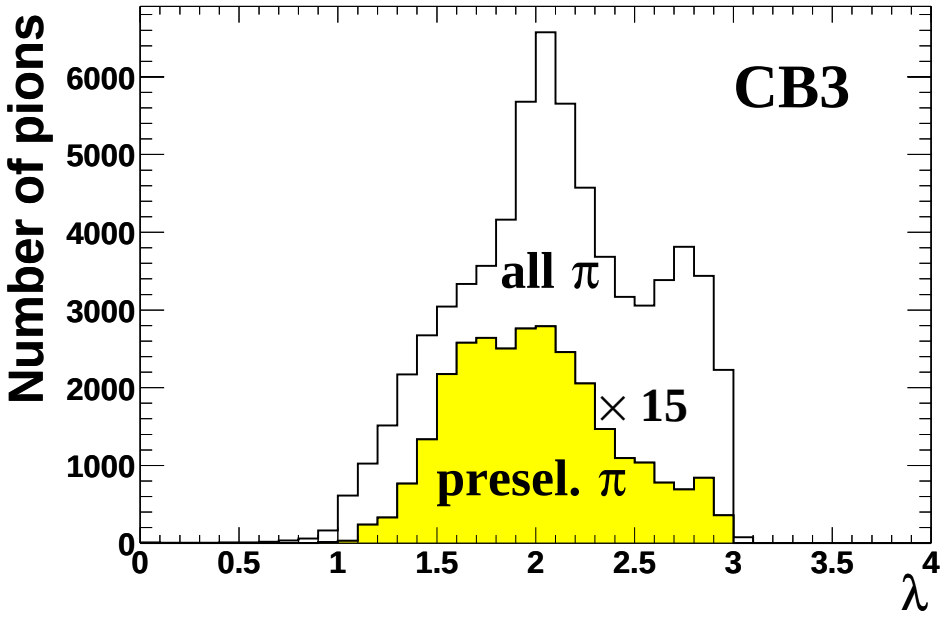

Figure 5.4: *Longitudinal energy deposition λ for pions with $p_T > 2$ GeV/c. The white histogram shows the distribution for all pions. For the shaded histogram, particles not matching the cuts listed in table 5.1 were rejected. It has been scaled by a factor 15.*

The restriction to hadronic showers with very large electromagnetic fractions has the advantage that the dependence on Monte Carlo simulations of hadronic showers is low.

The λ distributions for electrons and for pions before and after the preselection are shown in section A.1 for the different calorimeter wheels.

5.3 Lateral Energy Distribution

The definition of a shower's lateral spread requires

- a robust definition of a cluster axis,
- a measure for the distance of an energy deposition to this axis.

A cluster is defined as the group of cells being associated to a track. Quantities for the cluster are calculated using weights

$$w_j = \sqrt{|E_j|} \tag{5.2}$$

where E_j is the energy of the j^{th} cell[1].

[1]The absolute value of the cell energy is taken because electronic noise may result in negative energies.

In a first step, a barycentre $B_i(x, y, z)$ is calculated for each electromagnetic layer i. The positions P_j of the individual cells are summed individually in the coordinates x, y and z, weighted with w_j

$$B_i(x,y,z) = \frac{\sum_{j=1}^{N_i} w_j \cdot P_j(x,y,z)}{\sum_{j=1}^{N_i} w_j} \qquad \text{with } i = 1,2,3. \tag{5.3}$$

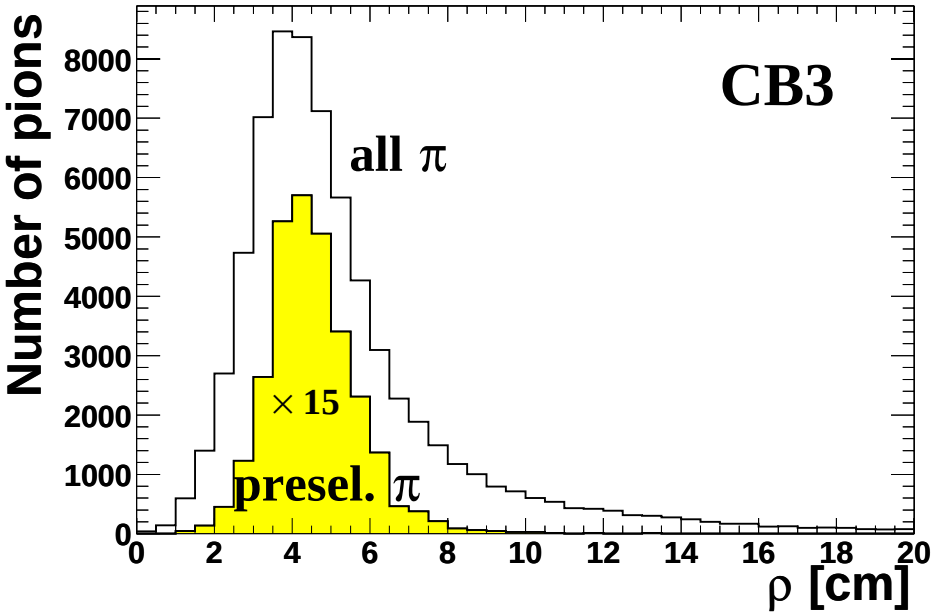

Figure 5.5: *The lateral energy deposition ρ for pions in the calorimeter wheel CB3. The shaded histogram represents the distribution after the rejection of pions not fulfilling the requirements listed in table 5.1. It has been scaled by a factor 15. The white histogram shows the distribution for all pions. All particles have transverse momenta larger than* 2 GeV/c.

The cluster axis CA is subsequently obtained by a linear concatenation of the three barycentre positions[2]. Figure 4.3 in chapter 4.2.1 shows a comparison of the track's ϑ value measured in the tracking chamber (on the x-axis) with the ϑ taken from the reconstructed cluster axis. It can be seen that the direction of the cluster can be well reconstructed by this method.

The lateral spread ρ is defined as the average of the distances $d(P_j, CA)$ of the cells' positions P_j to the cluster axis, weighted by w_j

[2]If no cells have been found for a layer, the other two layers are taken. In case of two layers without cells associated, no cluster axis is calculated and ρ cannot be computed.

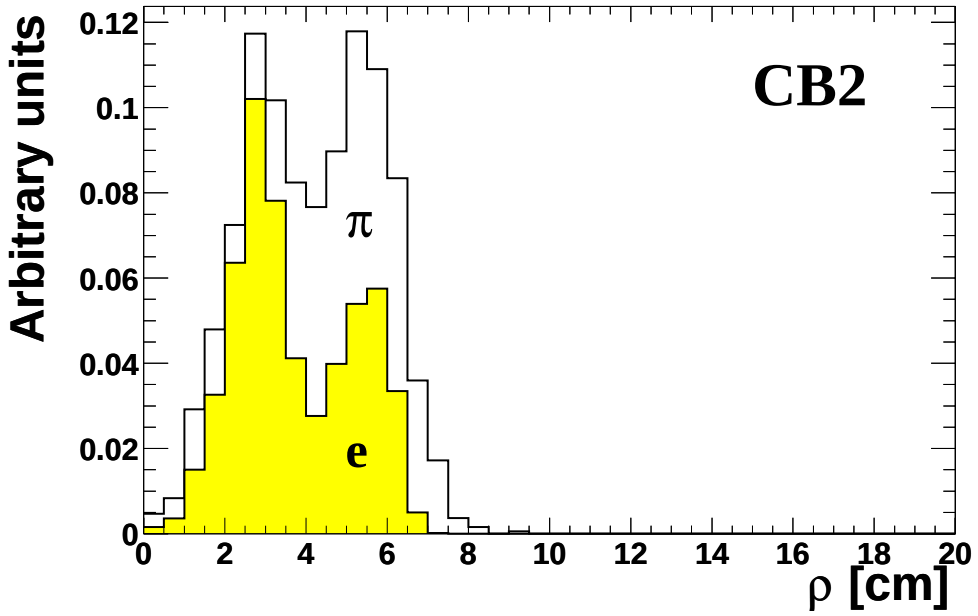

Figure 5.6: *The lateral energy deposition parameter ρ in the calorimeter wheel CB2: pions are shown in the white, electrons are shown in the shaded histogram. Both distributions have been obtained with single particle Monte Carlo simulations. Particles not fulfilling the cuts listed in table 5.1 were not included.*

$$\rho = \frac{\sum_{j=1}^{N} w_j \cdot d(P_j, CA)}{\sum_{j=1}^{N} w_j} \,. \tag{5.4}$$

The lateral spread of pion showers is compared in figure 5.5 for all particles (white histogram) with transverse momenta larger than 2 GeV/c to those fulfilling the requirements listed in table 5.1 (shaded histogram). The tail towards large ρ is very much reduced for the latter distribution, the mean is slightly shifted towards larger values.

The ρ distributions for selected electrons and pions passing the cuts listed in table 5.1 are plotted for particles in the LAr wheels *CB2* and *CB3*. *CB2* is built of larger cells than the wheel *CB3*. The small lateral spread of the electron showers is visible in both plots. The second peak at larger ρ values in case of the *CB2* distribution is caused by the large cell sizes in the second and third layer of the electromagnetic calorimeter.

The ρ distributions for electrons and for pions before and after the preselection from table 5.1 are shown in section A.2 for the different calorimeter wheels.

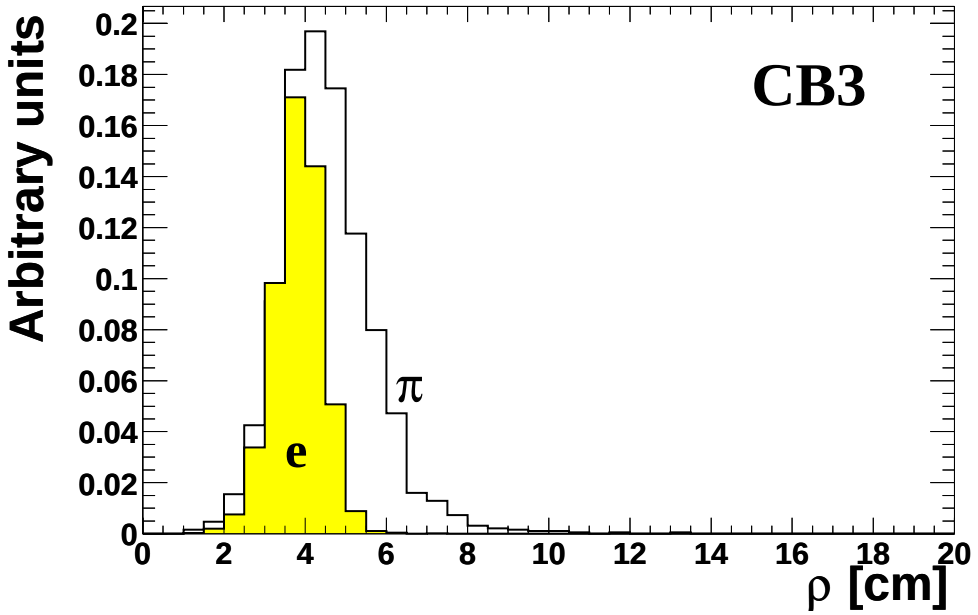

Figure 5.7: *The lateral energy deposition ρ in the calorimeter wheel CB3: pions are shown in the white, electrons are shown in the shaded histogram. Particles not fulfilling the cuts listed in table 5.1 were rejected.*

5.4 Comparison of Data and Simulation

5.4.1 Electrons

The identification of electrons using neural networks will be presented in the next chapter. It will be shown using independent data samples that actually electrons are selected by the neural networks. In this section, the description of the shower shapes in Monte Carlo simulations will be tested by comparing electrons from the decay of elastically produced J/Ψ-mesons in data and DIFFVM Monte Carlo simulations ([51]).

The invariant mass distribution for the J/Ψ-mesons candidates in the data sample is shown in figure 5.8. Electron candidates in events with two tracks were selected using the KALEP electron identification algorithm ([52]). Transverse momenta larger than 0.8 GeV/c were required for both tracks. In the following, only electron candidates from the peak region 2.95 GeV/c^2 $< M_{e^+e^-} <$ 3.15 GeV/c^2 are accepted.

The distribution of the longitudinal shower shape parameter λ (section 5.2) is shown in figure 5.9 for data (crosses) and simulation (solid line) in the LAr wheel *CB3*. The λ distribution is reasonably well described by the simulation in the four LAr wheels used in this analysis.

The lateral shower spread ρ, introduced in section 5.3, is equally well described by the simulation in case of the LAr wheels *CB1, CB2* and *FB1*. The distribution in the wheel *CB2* is shown

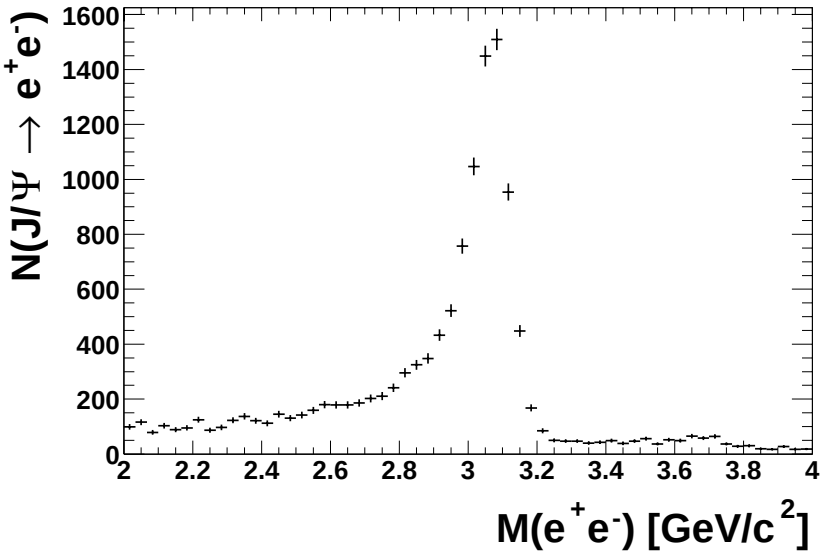

Figure 5.8: *Invariant mass distributions for elastically produced J/Ψ-meson candidates, reconstructed in the decay channel into two electrons. Input are data from the year 2000.*

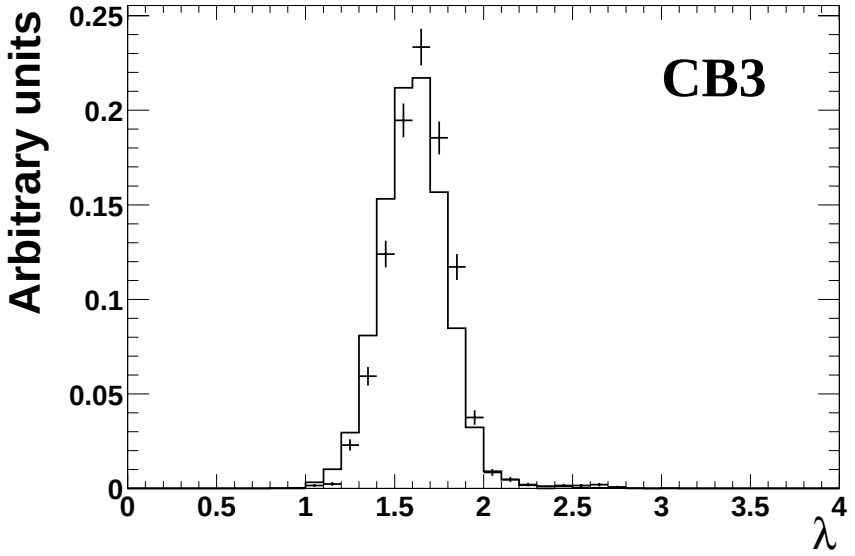

Figure 5.9: *The longitudinal shower shape parameter in the LAr wheel* CB3 *for electrons from the decay of elastically produced J/Ψ-mesons. The distributions show electrons from data (crosses) and from a DIFFVM Monte Carlo simulation (solid line). The λ distribution is reasonably well described by the simulation.*

in the left plot of figure 5.10. A small shift between data (crosses) and the simulation (solid line) is visible in the right plot of this figure where electron showers in the LAr wheel *CB3* are

presented. However, the neural network output values for this wheel are not affected by this shift, see section 6.2.

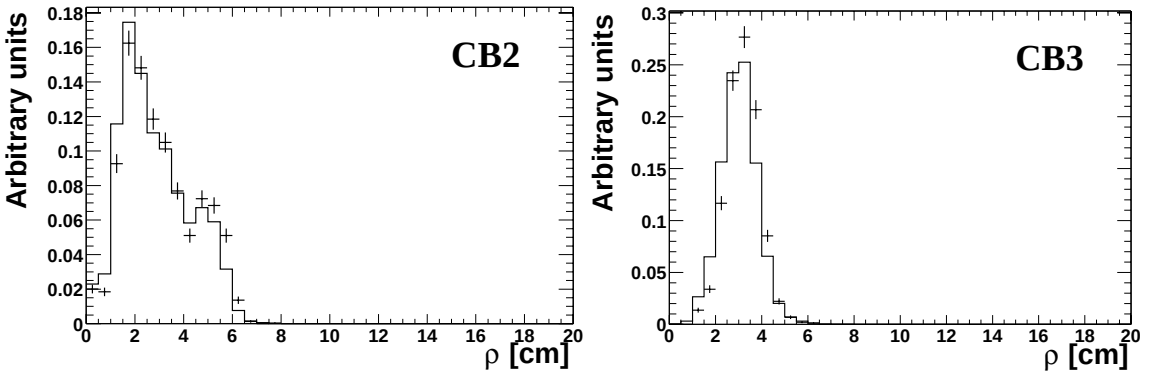

Figure 5.10: *The lateral shower spread in the LAr wheels* CB2 *(left) and* CB3 *(right) for electrons from the decay of elastically produced J/Ψ-mesons. The distributions show electrons from data (crosses) and from a DIFFVM Monte Carlo simulation (solid line). The ρ distribution is well described in case of the wheel* CB2*. The simulation in the high granularity wheel* CB3 *exhibits slight deficiencies as can be seen by the shift between the distributions.*

The "hot core fraction" has been temporarily considered as a third discriminating parameter. It is defined as the fraction of energy in the four most energetic cells of the whole cluster. Electrons tend to have hot core fractions close to one whereas hot core fractions around 0.8 are found for pions. The hot core fraction parameter is well described in the Monte Carlo simulation in case of the LAr wheels *CB1, CB2* and *FB1*. In the wheel with the highest cell granularity, *CB3*, differences between data and simulation are observed as can be seen from figure 5.11. The differences seem to be smaller than in the case of the λ in this calorimeter wheel. However, the resulting neural network output values for electrons from decays of elastic J/Ψ-meson differ very much between data and simulation so that the hot core fraction was not used for the neural network. The hot core fraction distributions for electrons and for pions before and after the preselection from table 5.1 are shown in section A.3.

The hot core fraction parameter was successfully used in a photon identification analysis ([53]) where the Monte Carlo sets were simulated using the standard GEANT ([54]) calorimeter simulation. The Monte Carlo simulations used in this analysis have been simulated with the H1FAST simulation ([42]) to be able to use large sets simulated with this option. The comparisons for the individual shower shape parameters reveal that the simulation of electron showers in the high granularity LAr wheel *CB3* is not optimal. However, no significant differences could be observed when simulating the single particle Monte Carlo sets with the GEANT calorimeter simulation.

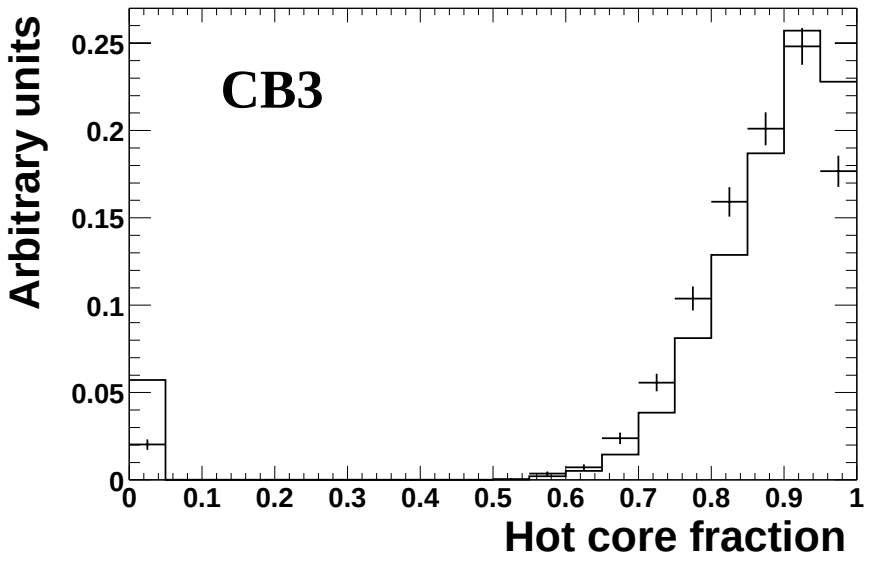

Figure 5.11: *The hot core fraction in the LAr wheel* CB3 *for electrons from the decay of elastically produced J/Ψ-mesons. The distributions show electrons from data (crosses) and from a DIFFVM Monte Carlo simulation (solid line). The Monte Carlo simulation does not describe the hot core fraction well. The description is significantly better in the other LAr wheels which have larger cell sizes.*

5.4.2 Hadrons

Detailed simulation of hadronic showers has not yet been achieved ([50]). It is thus very fortunate for this analysis that calorimeter showers from hadrons surviving the initial requirements listed in table 5.1 are dominated by the electromagnetic shower component. While imperfect simulation of hadronic showers may lead to worse hadron rejection than intrinsically possible, it does not render the electron identification method useless. The contribution of misidentified hadrons in the analysis is determined from the data, as will be explained in section 7.2.

The simulation of hadron showers passing the above mentioned cuts are in reasonable agreement with data. This can be seen from figure 5.13: the λ distribution for pions in the LAr wheel *CB3*, the most problematic wheel for simulations, is sufficiently well described.

It could not be determined in the course of this analysis whether the *fraction* of hadrons with large electromagnetic subshowers is correctly implemented by the simulations. The misidentification rate for pion candidates from K^0_S-meson decays is however, within statistical accuracy, of the same order of magnitude, around 0.1%, for both data and Monte Carlo simulation.

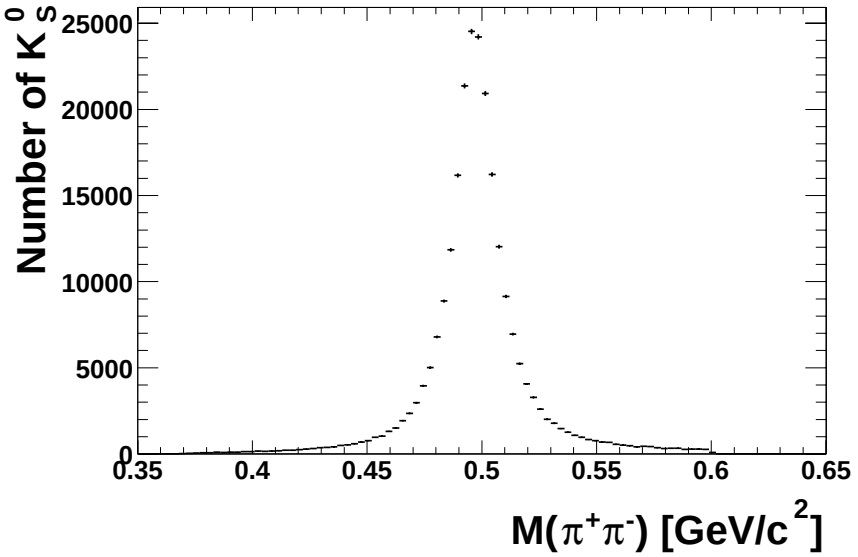

Figure 5.12: *Invariant mass distribution for K_S^0-mesons decaying into two charged pions. One of the pions has a transverse momentum of at least* 0.8 GeV/c. *An upper cut on the mass of* 0.6 GeV/c^2 *was applied.*

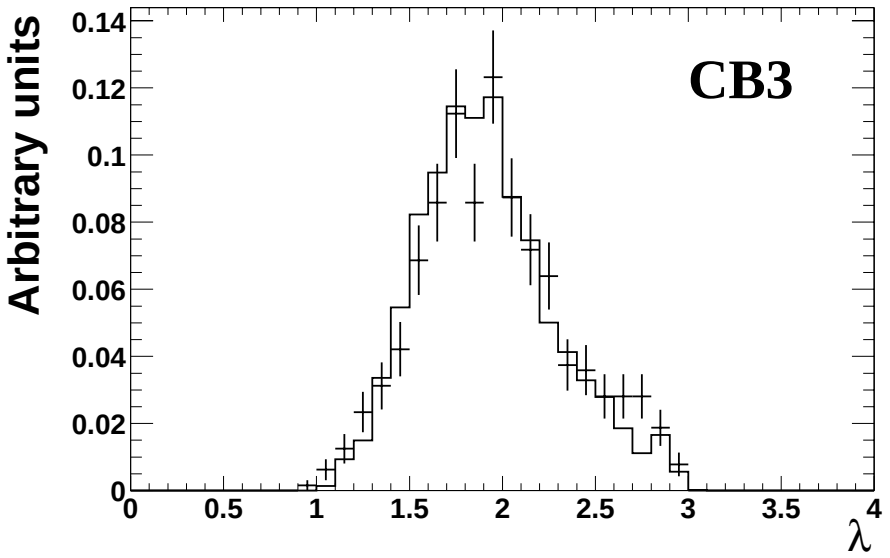

Figure 5.13: *The longitudinal shower parameter in the LAr wheel CB3 for pion candidates from K_S^0-meson decays passing the cuts listed in table 5.1. Pions from data (crosses) are compared with pions from Monte Carlo simulations (solid line). Both λ distributions show reasonable agreement.*

Chapter 6

Electron Identification using Neural Networks

The identification of electrons is performed by the combination of shower shape parameters introduced in the previous chapter and the specific energy loss, measured in the drift chamber, in neural networks. Individual networks are set up for each of the four LAr wheels used because their different granularities lead to differences in the shower shapes. All particles have to pass a set of cuts first, already leading to a rejection of more than 90% of all hadrons before the neural networks.

The setup of the neural networks and the preselection of particles will be presented first in this chapter. It will be followed by a discussion of the neural network output values in Monte Carlo simulations. Afterwards, a search for inelastically produced J/Ψ-mesons in data is performed which shows that the method works to select electrons. In the end, $D^{*\pm}$-meson electron pairs are reconstructed in data.

6.1 Neural Network Setup

6.1.1 Neural Network Training

Each of the calorimeter wheels is treated in its own neural network which have otherwise identical setups. Common feed-forward networks are used, trained with the backpropagation algorithm ([55]). The networks consist of 3 input nodes, one hidden layer containing 6 nodes and one output node. The input parameters are:

- the longitudinal energy deposition λ,
- the lateral shower spread ρ,
- the specific energy loss $\mathrm{d}E/\mathrm{d}x$ measured in the tracking chambers.

The input parameters are scaled to fit into the range [0, 1]. In case of the parameter λ, a fixed value of 1.0 is subtracted before scaling. (See figure 5.3 for a plot of a λ distribution.)

The relativistic rise of $\mathrm{d}E/\mathrm{d}x$ is not well modelled in the Monte Carlo simulations so that a parameterisation from hadrons in data is taken and random values are chosen accordingly.

The neural network training is performed using single particle Monte Carlo simulations for electrons and pions[1]. All particles have transverse momenta of at least 2 GeV/c. The networks are trained such that electrons should receive output values of 1 whereas hadrons should get a value of 0.

6.1.2 Preselection of Particles

Several approaches of electron identification with neural networks were tried before the method used in this thesis was developed.

At first, all particles without any cut were examined by the neural network, only $p_T > 2$ GeV/c was required. This led to very large hadron misidentification rates because the network could not distinguish between electrons and hadrons with electron-like showers. It had only learned to separate the majority of the hadrons – with small electromagnetic sub-showers – from electrons. Tuning of the neural network setup in terms of number of hidden nodes, training cycles and number of particles used for the training had not led to significant improvements.

It was then tried to use a second neural network, running subsequently after the first one. Only electrons and hadrons with neural network output values close to one, the training value for electrons, entered the second network. It was trained using regular Monte Carlo simulations whereas the first network was trained using single particle simulations. However, the overall electron identification efficiency turned out to be very low and the application of the second network was discarded.

In the procedure taken now, easily identified hadrons are rejected and only hadrons with electron-like showers enter the neural network. The most important cut is on the ratio of the shower energy E to the measured momentum p which is around 1 for electrons. The particles have to pass the following cuts:

- The calorimeter cluster must be located in one of the 4 central LAr wheels (corresponding to $28° \leq \vartheta \leq 145°$),
- $p_T > 2$ GeV/c,
- $0.8 < E/p < 1.2$,
- $f_{HAD} = 0$,
- $1 \leq \lambda \leq 3$,
- $\rho < 20\ cm$,

[1] A mixture of pions, kaons and protons instead of using pions only was tried but has not lead to improvements in the background rejection.

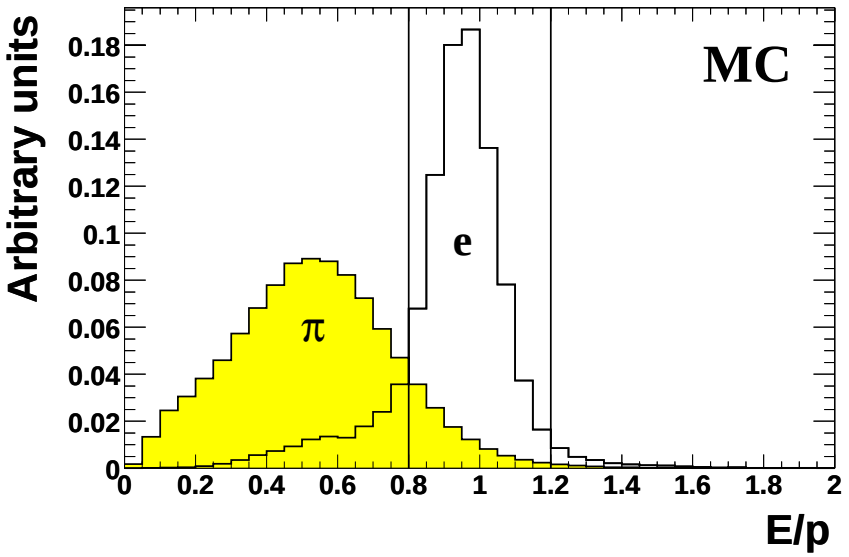

Figure 6.1: *E/p for electrons (white histogram) and pions (shaded histogram) in single particle simulations. Particles inside the range $0.8 < E/p < 1.2$, indicated by the two vertical lines, are selected for the neural network provided they have no energy depositions in the hadronic calorimeter.*

- Every particle must be part of a jet containing at least one additional particle. (This is not required for the neural network training.)

The E/p distributions for electrons and pions are shown in figure 6.1. E/p for electrons (white histogram) and pions (shaded histogram) is plotted for particles with transverse momenta larger than 2 GeV/c which have no energy depositions in the hadronic calorimeter. A large part of the hadrons is rejected by requiring that a particle's E/p value is inside the range $0.8 < E/p < 1.2$ whereas more than 80% of all electrons pass these requirements. The neural networks therefore only have to learn to separate hadrons with electron-like showers from real electrons.

The enrichment of electrons by the selection described above can also be seen from figure 6.2. The $\mathrm{d}E/\mathrm{d}x$ distribution in a PYTHIA Monte Carlo simulation is shown after the selection has been applied. The white histogram contains both electrons and hadrons, the shaded histograms shows the hadron fraction only. Electrons are clearly visible at large $\mathrm{d}E/\mathrm{d}x$ values. The electron fraction in the given sample is approximately 10% before the neural networks.

6.2 Neural Network Output

The performance of the neural networks is tested using a PYTHIA Monte Carlo simulation containing contributions from light and heavy flavour production. Both direct and resolved processes are included. The usual event selection, requiring a track with a minimal transverse momentum of 2 GeV/c and two jets with p_T larger than 6 and 5 GeV/c respectively, was applied.

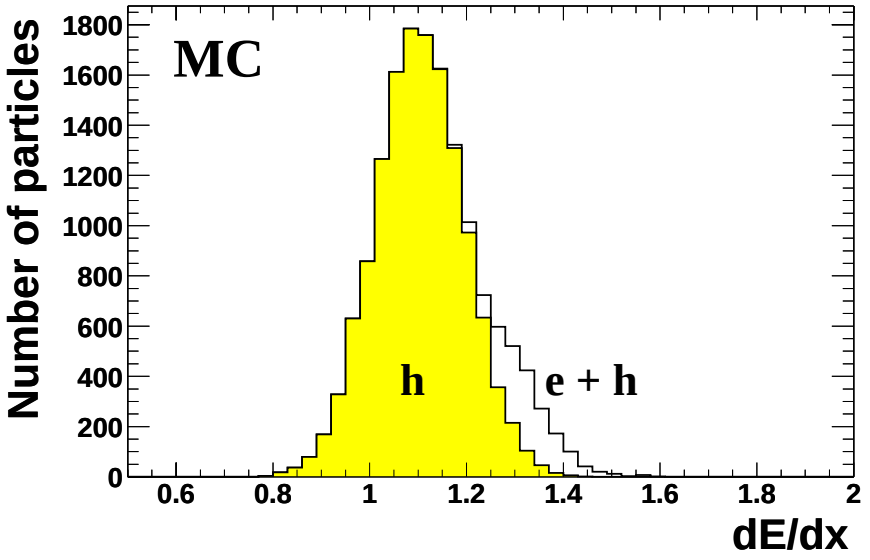

Figure 6.2: *The specific energy loss* $\mathrm{d}E/\mathrm{d}x$ *for hadrons (shaded histogram) and hadrons + electrons (white histogram) which have passed the neural network entrance cuts. The neural network itself has not yet been applied. The contribution from electrons in this PYTHIA Monte Carlo simulation, approximately 10%, is clearly visible.*

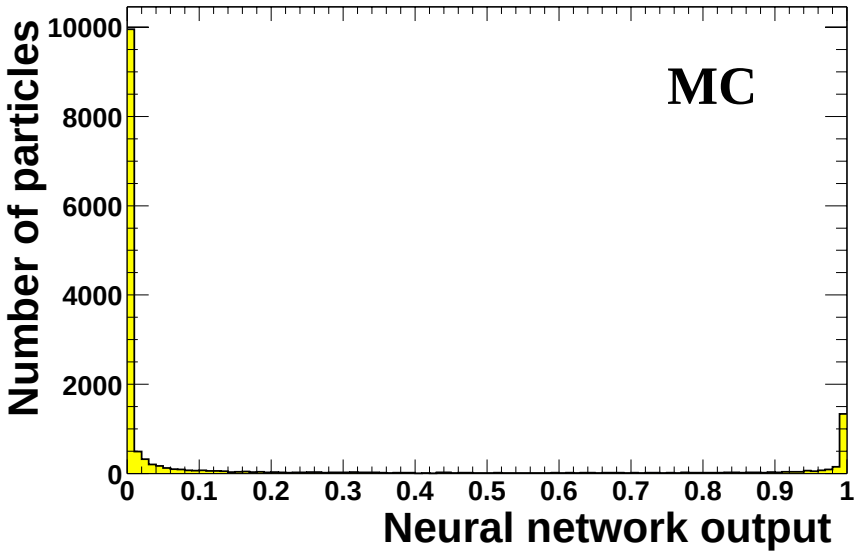

Figure 6.3: *Neural network output values in a PYTHIA Monte Carlo simulation. Almost all hadrons are close to zero, most electrons are found at values close to one. Figure 6.4 shows the close-up range 0.98 – 1.*

The neural network output values are shown in the histogram of figure 6.3. Hadrons are accumulated on the left side at values close to zero, electrons have output values close

to one. Electron candidates are selected by requiring output values larger than 0.99. The distributions of the output values for hadrons and electrons in the individual LAr wheels are presented in figure 6.4. Only the range very close to one, from 0.98 to 1, is plotted. The shaded histograms represent the contributions from hadrons alone, the white histograms show electrons and hadrons. The output value distributions of hadrons are flat so that a cut of 0.99 is chosen. The corresponding distributions for the data samples will be shown in the next chapter.

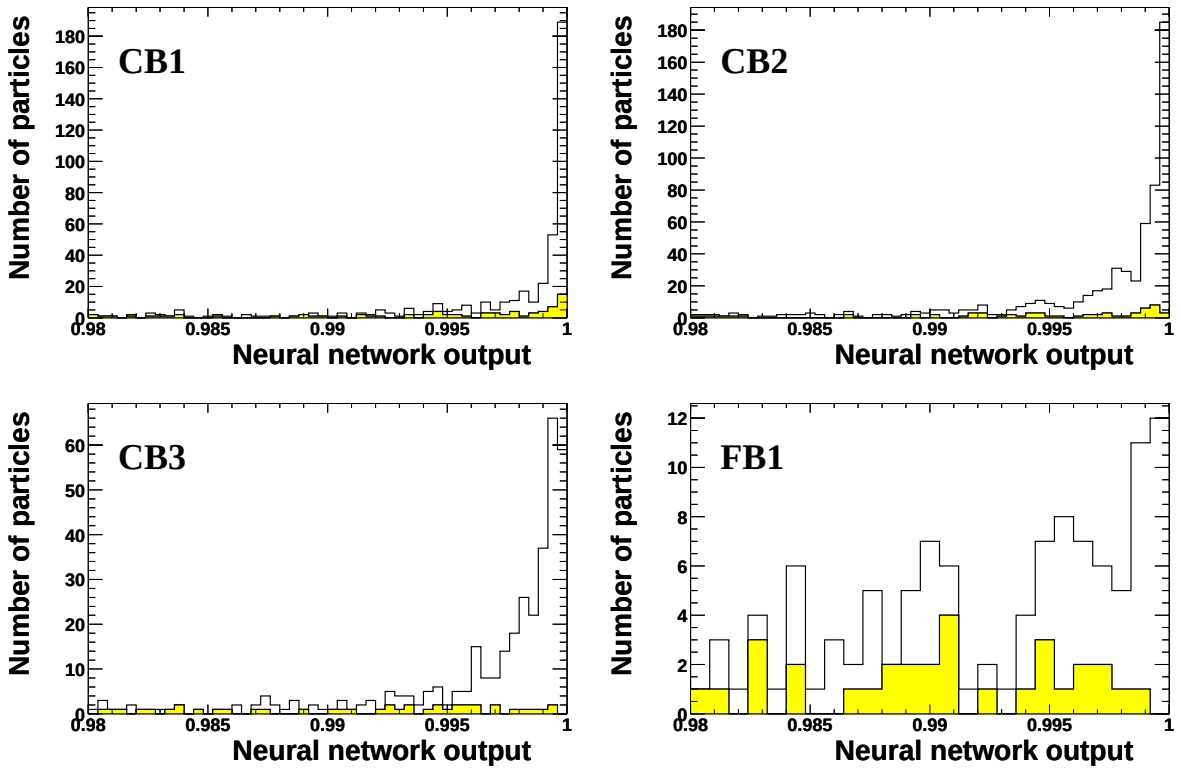

Figure 6.4: *Distribution of neural network output values in the range 0.98 – 1.0 in the four LAr wheels for a PYTHIA Monte Carlo simulation. The contributions from hadrons and electrons are shown as the white histogram, the shaded histograms represent the hadrons only.*

The electron identification efficiency *of the neural networks* is defined as the ratio of electrons accepted by the cut on the neural network output value to the number of electrons in the neural network: $\epsilon_{NN} = \frac{N_{elec}^{acc}}{N_{elec}^{acc}+N_{elec}^{rej}}$. Electrons which have not passed the neural network entrance cuts, see section 6.1.2, are not considered in this efficiency definition. This electron identification efficiency is plotted on the left side in figure 6.5. The electron selection purity, defined as the ratio of electrons selected by the neural networks to the sum of selected electrons and misidentified hadrons, is shown on the right. The efficiency in the fourth LAr wheel, *FB1*, is about 50% lower than for the other wheels but the same level of electron purity of 80 – 90% is reached in *FB1*. The cut on the output value of 0.99 has been chosen as a compromise between

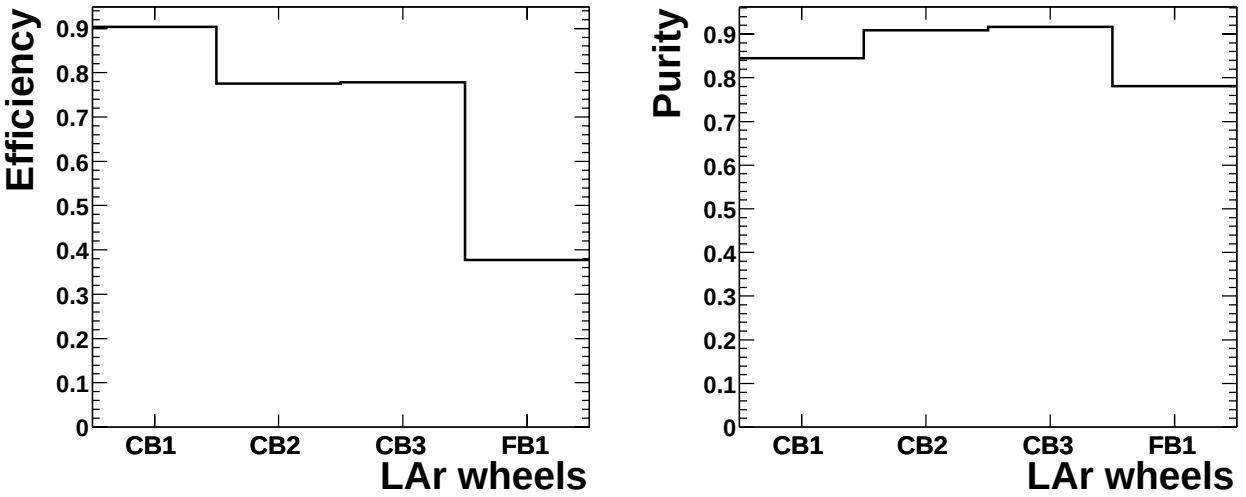

Figure 6.5: *Electron selection efficiency of the neural networks (left) and purity (right) in a PYTHIA Monte Carlo simulation. Electrons are selected by a cut on the neural network output value larger than 0.99. Electrons not entering the neural network are not accounted for in the given selection efficiency values.*

reaching high electron selection efficiencies and low hadron misidentification probabilities. The low electron identification efficiency in *FB1* may be caused by the increase in dead material between the CJC and this LAr wheel.

	Number of electrons	Number of hadrons	Electron purity
Before NN (in acceptance)	3,978	397,882	0.99%
Accepted for NN	1,563 (39.3%)	13,789 (3.5%)	10.2%
Passed NN output cuts	1,183 (29.7%)	144 (0.04%)	89.1%

Table 6.1: *Electron identification efficiencies, hadron misidentification probabilities and electron purities in a PYTHIA Monte Carlo simulation containing contributions from light and heavy flavours. All particles have transverse momenta of at least* 2 GeV/c*. The numbers given also include losses due to the jet cuts: two jets with minimal transverse momenta of 6 and 5* GeV/c *respectively are required for each event.*

The electron identification efficiencies and the hadron misidentification probabilities which have been obtained by this Monte Carlo simulation are summarised in table 6.1. The numbers given also include losses of electrons due to the jet requirements. More than 95% of all hadrons with $p_T > 2$ GeV/c do not even enter the neural networks, 40% of the electrons are accepted. After application of the neural networks, less than 0.1% of all hadrons are falsely identified as electrons, leading to an increase in the electron purity from 1% to 90% throughout the analysis steps.

6.3 Inelastic Production of J/Ψ-Mesons

The applicability of methods derived with extensive input of Monte Carlo simulations to data has to be shown. As no alternative method for the identification of electrons in jets exists, indirect tests have to be performed. Therefore, the reconstruction of inelastically produced J/Ψ-mesons decaying into an electron positron pair has been chosen to test the electron identification.

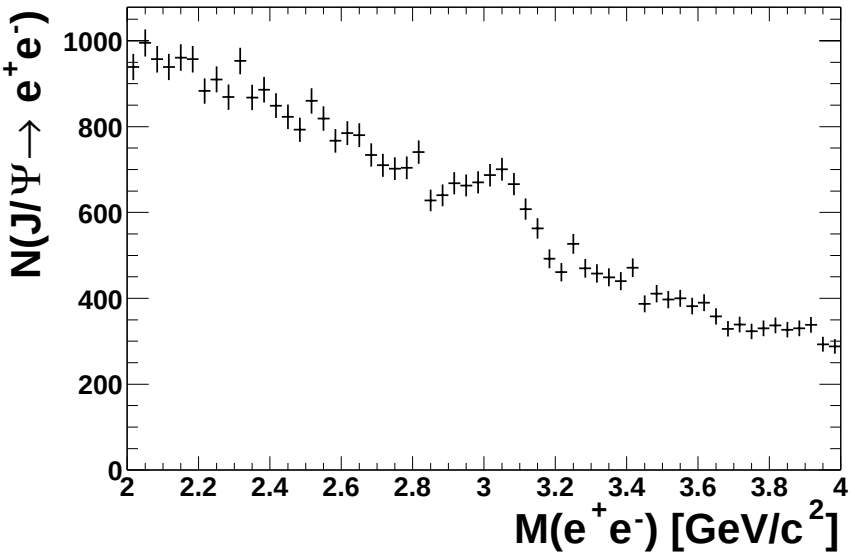

Figure 6.6: *Search for inelastically produced J/Ψ-mesons decaying into two electrons. In this plot, a neural network output value larger than 0.99 was required for one of the tracks. No requirements were made for the second track, i. e. particles with any E/p values were accepted.*

The selection of the events was done as follows:

- All data taken with the H1-Detector in the years 1999 and 2000 were used.
- No preselections (triggers, kinematical cuts) were applied.
- The events must have at least 5 tracks measured in the Central Jet Chambers in order to ensure inelastic production.
- All candidate particles were required to have a minimal momentum of 1 GeV/c. (It should be noted that this kinematic regime only partially overlaps with that of the neural network training, where $p_T > 2$ GeV/c is required.)
- The invariant mass combination for two oppositely charged particles has to be in the range $2\ \text{GeV}/c^2 < M_{e^+e^-} < 4\ \text{GeV}/c^2$ when electron masses are assumed.

The resulting invariant mass distribution is shown in figure 6.6 when one of the tracks was required to be a well identified electron by cutting on a neural network output value of 0.99.

No electron identification was required for the second track. Only a small enhancement in the region of the nominal mass for the J/Ψ-meson at 3.096 GeV/c^2 can be seen.

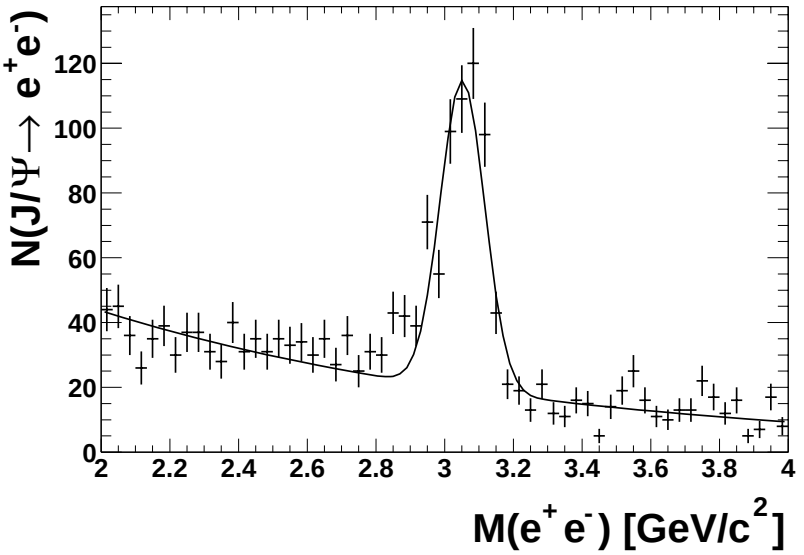

Figure 6.7: *The invariant mass distributions for inelastically produced J/Ψ-mesons after requiring neural network output values larger than 0.1 for both electron candidates.*

The requirements on the electron candidates are changed for figure 6.7. Both particles have to have neural network output values larger than 0.1. The background is very much reduced and a clear mass peak is visible. The main source of background is non-resonant lepton pair production.

The search for inelastically produced J/Ψ-mesons has shown that the identification of electrons using neural networks works and is actually applicable to data. Its application to the semileptonic decay of beauty hadrons will be presented in the next chapter.

6.4 Electrons in Events with $D^{*\pm}$-Mesons

An interesting application of the electron identification in jets is the analysis of $D^{*\pm}$-meson electron pairs. The $D^{*\pm}$-meson is reconstructed in its "golden" decay mode: $c \to D^{*\pm} \to D^0\pi_s^\pm \to K^\mp\pi^\pm\pi_s^\pm$. The pion from the $D^{*\pm}$-meson decay, denoted with $\pi_s^\pm$, is called the "slow pion" because the small mass difference between the $D^{*\pm}$- and the D^0-meson leaves only very few kinetic energy to the pion. The branching ratio for a charm quark pair to yield a $D^{*\pm}$-meson and an electron is small, $\mathcal{B}R(c\bar{c} \to K^\mp\pi^\pm\pi_s^\pm e) = 0.1211\% \pm 0.0055\%$ ([12]), but the combination of a $D^{*\pm}$-meson and a lepton offers a clean double-tag of both heavy quarks and thus to the quark kinematics ([9]).

There are 4 possibilities in which the charge of the $D^{*\pm}$-meson and of the electron and their azimuthal angle difference can be combined. These are called correlation regions ([56], [9]).

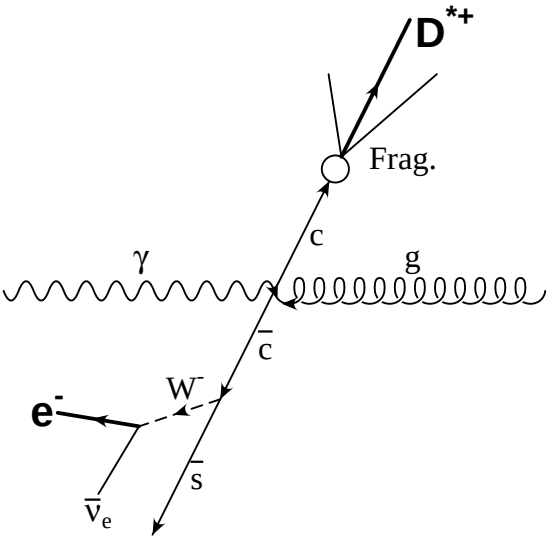

Figure 6.8: *Feynman diagram for the production of a $D^{*\pm}$-meson electron pair in correlation region 4.*

In case of charm production, nearly all events belong to the correlation region 4 (*CR4*): the electron stems from the decay of one charm quark and the $D^{*\pm}$-meson from the decay of the other. As a result, the electron and the $D^{*\pm}$-meson carry opposite charges and have an azimuthal angle difference of approximately 180°. This situation is shown in figure 6.8.

Here, data from the years 1997, 1999 and 2000 were used and one of the subtriggers 61, 83 and 84 was required. No *L4*-finder selection was applied which should be done if a real analysis in this channel would be performed. The following cuts were made on the $D^{*\pm}$-meson electron pair:

- $p_T(D^{*\pm}) > 2.5$ GeV/c,
- $p_T(electron) > 0.8$ GeV/c,
- Neural network output > 0.99.

The number of $D^{*\pm}$-mesons is usually determined by fitting the signal region of the ΔM distribution ([57]). ΔM is defined as the invariant mass difference between the reconstructed $D^{*\pm}$-meson and the D^0-meson, $\Delta M = M(K^{\mp}\pi^{\pm}\pi_s^{\pm}) - M(K^{\mp}\pi^{\pm})$. Figure 6.9 shows the resulting ΔM distribution in the correlation region 4 where 38.6 ± 8.7 $D^{*\pm}$-meson electron pairs are reconstructed. The total data set without electron requirement contains about 7500 $D^{*\pm}$-mesons with a much worse signal to background ratio. No $D^{*\pm}$-meson electron pairs could be reconstructed in the correlation regions 1 – 3 where only few events are expected in case of charm production. $D^{*\pm}$-meson electron pairs in beauty production significantly contribute to correlation regions 2 and 3 but the overall event statistics is too low for a proper measurement. Background processes dominate in correlation region 1.

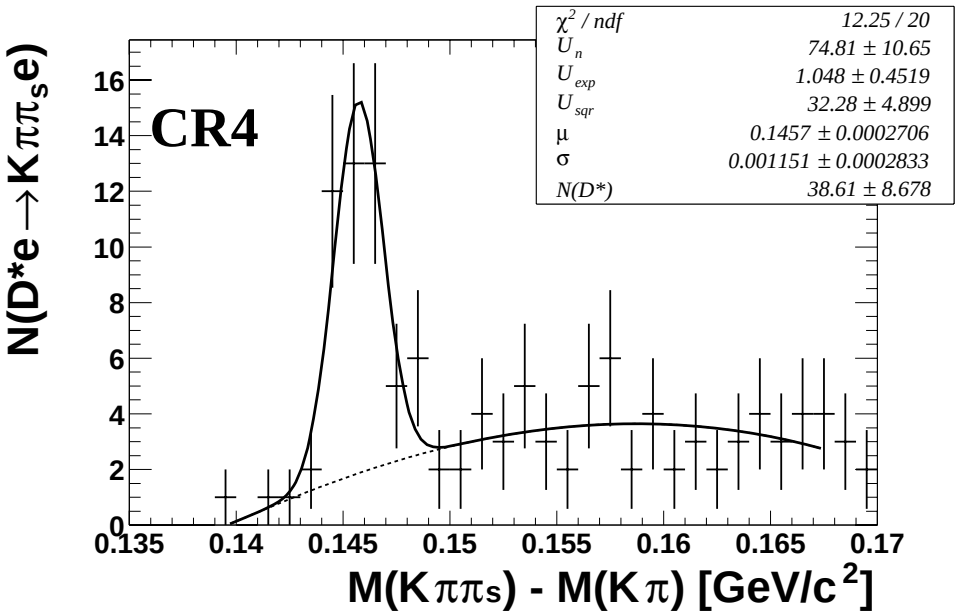

Figure 6.9: ΔM *distribution for* $D^{*\pm}$*-meson electron pairs in the correlation region 4 (CR4, see the text for more details). Transverse momenta larger than* 0.8 GeV/c *are required for the electron candidate and* 2.5 GeV/c *for the* $D^{*\pm}$*-meson. Data taken with the H1-Detector in the years 1997, 1999 and 2000 were used for this plot.*

Chapter 7

Electrons in Beauty Production

The determination of the fraction of electrons from beauty processes in the photoproduction and the DIS sample will be presented in this chapter.

First, the properties of electrons in beauty production will be compared to those from background processes. The dominant contribution to the background are electrons from charm hadron decays, electrons from photon conversion processes and misidentified hadrons.

The fit procedure leading to the determination of the fraction of beauty hadron decays into electrons will be explained afterwards. The fractions of photon conversion electrons and of misidentified hadrons are determined first. In a second step the fractions of beauty and charm electrons are obtained by a fit to the distribution of the relative transverse momenta of the electron candidates.

7.1 Properties of Electrons from Beauty Hadron Decays

The beauty quark's large mass of about 4.75 GeV/c^2 leads to larger energy transfers to the decay electrons than is the case for electrons from charm or light quark decays. In addition, the electrons' spatial separation from other beauty hadron decay particles is larger than for other processes. These features will be exploited to separate the contributions from the individual processes.

7.1.1 Relative Transverse Momentum $\mathbf{p_{T,rel}}$

The relative transverse momentum $p_{T,rel}$ of a particle to the jet it belongs to is defined as

$$p_{T,rel} = \frac{|\vec{p}_{elec} \times \vec{p}_{jet}|}{|\vec{p}_{jet}|} \tag{7.1}$$

The variable $p_{T,rel}$ is used in this analysis to determine the fraction of electrons from beauty production.

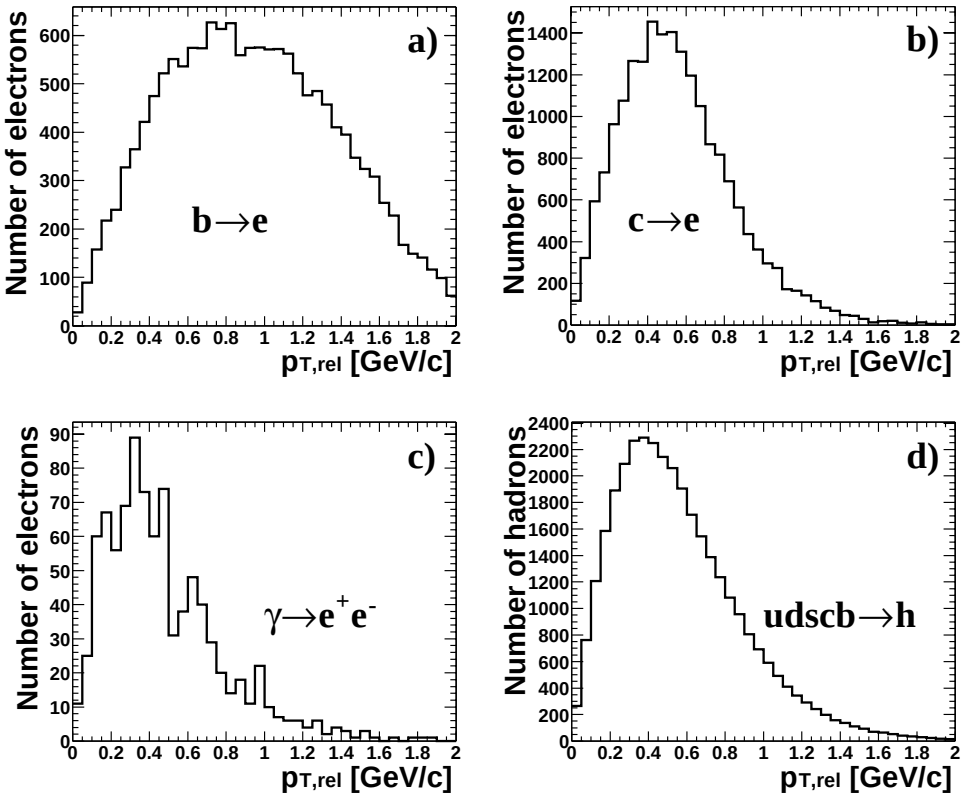

Figure 7.1: *Relative transverse momenta $p_{T,rel}$ of particles in jets in Monte Carlo simulations.* a) *Electrons from beauty production,* b) *electrons from charm production,* c) *electrons from photon conversion processes,* d) *hadrons in light and heavy flavour processes.*

The $p_{T,rel}$ distributions from Monte Carlo simulations for the processes relevant in the analysis are shown in figure 7.1. Electrons from beauty hadron decays show large $p_{T,rel}$ values (a) whereas the $p_{T,rel}$ distributions for electrons from charm production (b) and for hadrons from light and heavy flavour processes (d) are at much smaller values. The distributions for hadrons from light and heavy flavour processes are nearly equal. Furthermore the differences between the $p_{T,rel}$ distributions of charm electrons and hadrons are so small that they cannot be separated reliably. The hadron fraction is thus determined before the final fit and fixed; this will be explained in section 7.2.1.
The third plot (c) shows the $p_{T,rel}$ distribution for electrons from photon conversion processes. The maximum is closer to zero than in the hadron distribution.

7.1.2 Distance to the Neighbouring Track ΔR

The distance of a particle to its closest neighbouring track is measured by

$$\Delta R = \sqrt{(\Delta\varphi)^2 + (\Delta\eta)^2}\ . \tag{7.2}$$

The variables φ and η are track parameters measured in the standard H1 coordinate system introduced in section 2.2. ΔR is a well suited parameter for the determination of the photon conversion fraction. This can be seen from figure 7.2 where the ΔR distribution is shown for the four relevant processes. Electrons from beauty hadron decays are separated from other decay particles (a), leading to ΔR values larger than 0.3 for the majority of the electrons. Electrons from charm hadron decays (b) as well as hadrons (d) tend to be more "inside" their jets, showing ΔR distributions centred around 0.15 – 0.25. Electrons from photon conversion processes are created in pairs with small opening angles. As a result, the distance to the closest neighbouring track is very small as can be seen from figure (d). The second electron must not necessarily be identified as such. Large ΔR values may occur when for example the second electron fails to pass the track selection.

The individual contributions to the ΔR distribution can be demonstrated by looking at "high Q^2 data", corresponding to Q^2 values larger than 150 GeV^2, which are excluded from the regular analysis. Here, the scattered electron is reconstructed in the LAr calorimeter and it is in general spatially separated from the particles of the Hadronic Final State. Three components are expected in the ΔR distribution:

- the scattered electron at very large ΔR,
- electrons from photon conversions at very small ΔR,
- hadrons at medium ΔR.

All of these components can be seen in the plots of figure 7.3: the upper plot shows particles rejected before the neural networks (see section 6.1.2). These are almost all hadrons. Particles accepted for the neural networks lead to a ΔR distribution as in the plot in the middle: photon conversion electrons become visible at $\Delta R \approx 0$, the contribution from scattered electrons appears at large ΔR. When almost all hadrons are rejected by the neural networks as shown in the lowest picture, the region of $\Delta R \approx 0.15 - 0.25$ contains only few entries. The photon conversion electron contribution is even more pronounced.

7.1.3 Reduction of Photon Conversion Processes

As many photon conversion electrons as possible are rejected in the data samples as they are a background process for the analysis. A particle is identified as a photon conversion electron if

- it is fitted to a secondary vertex,
- the two electron candidates form a small opening angle of less than 4.5°,

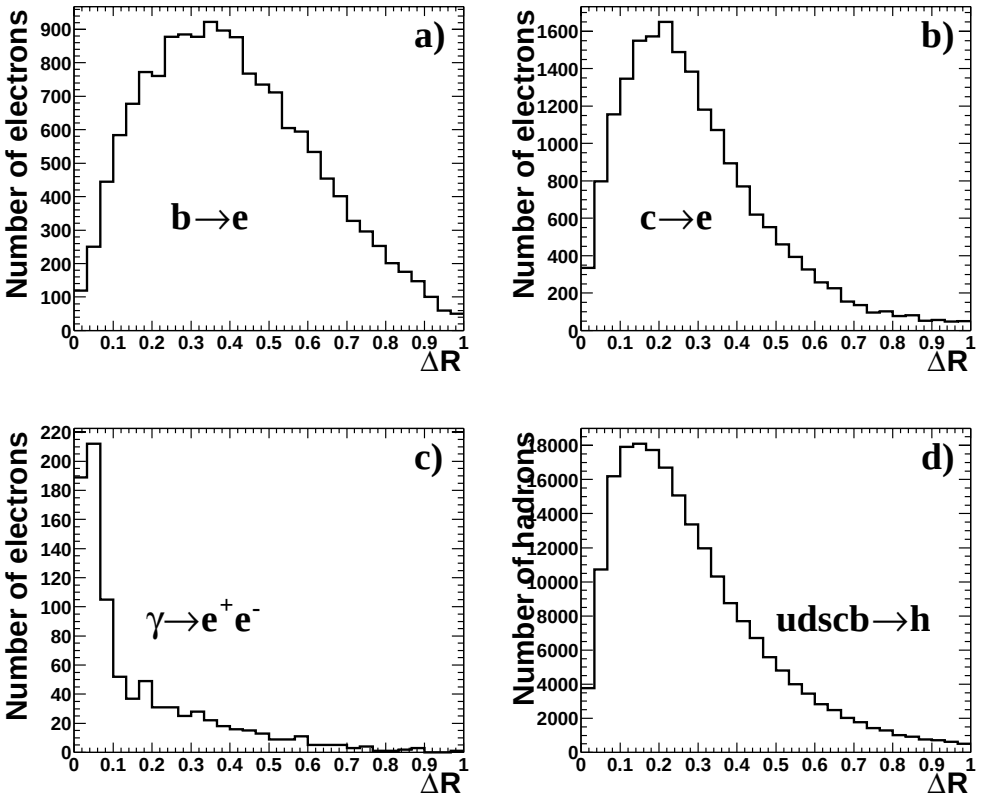

Figure 7.2: *Distance* $\Delta R = \sqrt{(\Delta\varphi)^2 + (\Delta\eta)^2}$ *from a particle to the closest neighbouring track in Monte Carlo simulations:* a) *electrons from beauty production,* b) *electrons from charm production,* c) *electrons from photon conversion processes,* d) *hadrons in light and heavy flavour processes.*

- the invariant mass combination of the two particles assuming electron masses for each of them must be less than 60 MeV/c^2.

The contribution of photon conversion electrons is reduced by a factor 2 with these cuts. This can be seen from figure 7.4 where the ΔR distribution for electron candidates in the photoproduction sample is shown. The left pictures contains 536 entries, a rise towards $\Delta R \approx 0$ is clearly visible. Identified photon conversion electrons are rejected for the right plot, leading to 475 entries in the histogram. The contributions at very low ΔR are strongly reduced.

7.1.4 Contributions of Mesons with Higher Spins

Mesons with higher spins such as the f_2 are not generated by the standard H1 Monte Carlo simulation settings. Many of these mesons decay predominantly into two particles. The absence of these particles in the simulation could result in an inaccurate description of the hadrons' ΔR distribution.

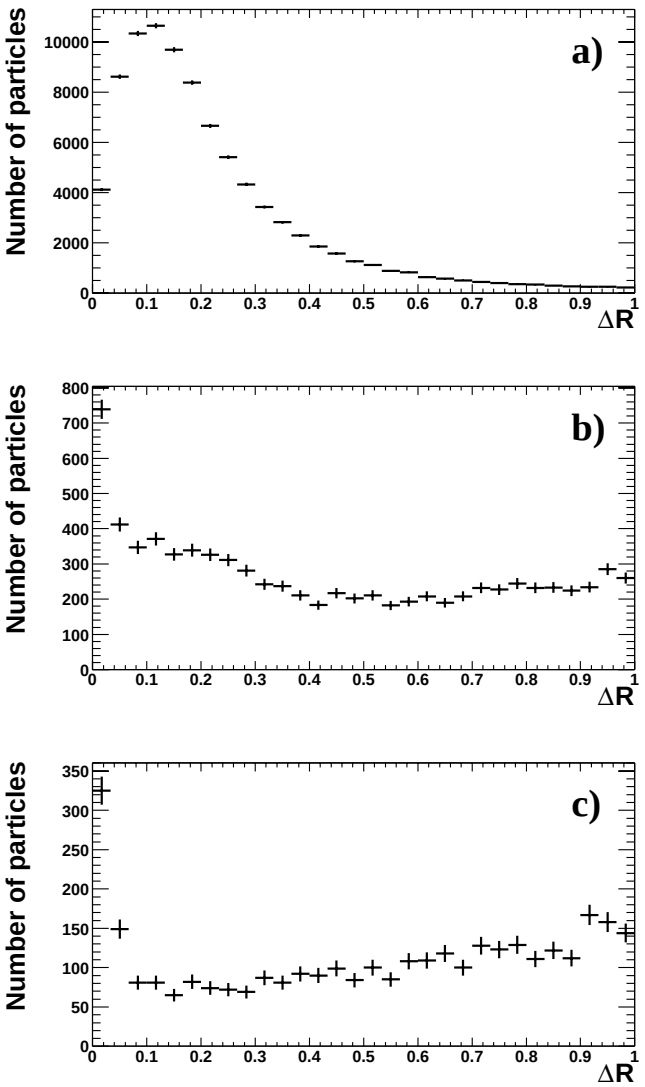

Figure 7.3: *Distance ΔR from a particle to its closest neighbouring track in a data sample where the beam electrons were scattered under very large angles and detected in the LAr calorimeter ($Q^2 > 150$ GeV^2).* a) *Particles rejected before the neural networks,* b) *particles accepted for the neural networks,* c) *electron candidates selected by the neural networks. The contributions of electrons from photon conversion processes at $\Delta R \approx 0$ and of scattered electrons at large ΔR are clearly visible.*

The ΔR distribution for hadron candidates, selected via their rejection for the neural networks, in the photoproduction sample are compared with the standard PYTHIA6.1 simulation and a PYTHIA6.2 simulation containing also mesons with higher spins. The result is shown in figure 7.5: the data (crosses) are reasonably well described by the PYTHIA6.1 simulation (solid line)

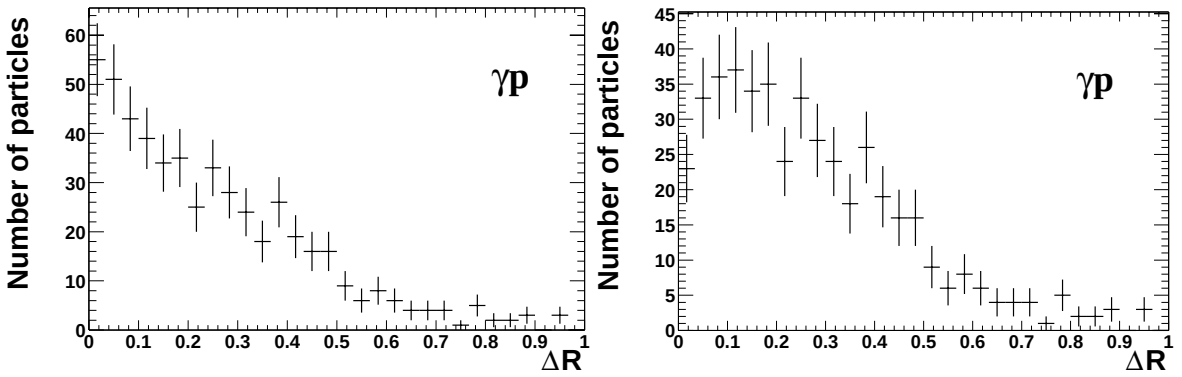

Figure 7.4: *Distance ΔR from a particle to its closest neighbouring track in the photoproduction sample. The plots show the ΔR distribution of electron candidates after passing the neural networks.* Left: *no rejection of electrons from photon conversion processes was applied (536 particles).* Right: *identified photon conversion electrons were rejected before entering the neural networks (475 particles).*

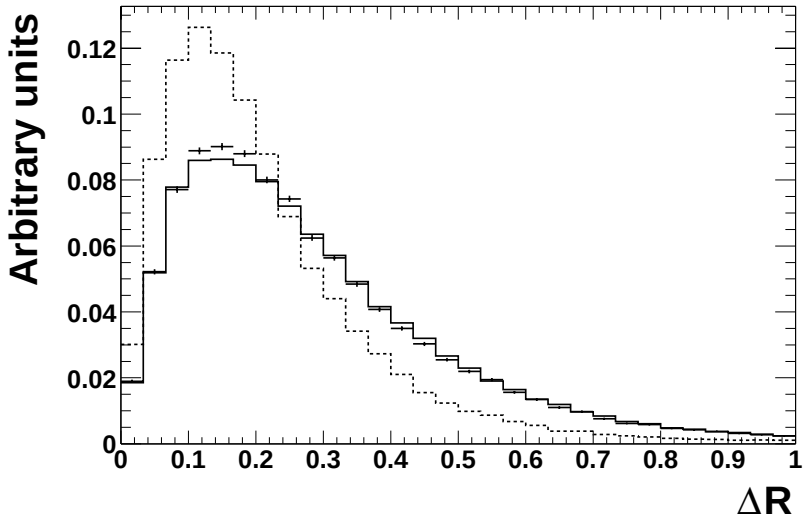

Figure 7.5: *Distance ΔR from a hadron candidate to its closest neighbouring track. The crosses show the distribution for hadrons in the photoproduction sample. It is well described by the PYTHIA6.1 Monte Carlo simulation, drawn as the solid line. The PYTHIA6.2 simulation (dashed line) containing also higher spin mesons such as the f_2 fails to describe the data. All distributions are normalised to the total number of events.*

whereas the PYTHIA6.2 simulation (dashed line) shows a much too narrow distribution[1]. This could be an indication that too many higher spin mesons are generated. Other variables such as

[1]Parameters tuned to LEP data were used for the PYTHIA6.2 simulation. It should be kept in mind that the PYTHIA6.2 generator is not yet a standard Monte Carlo in the H1-Experiment.

the $p_{T,rel}$ distribution of hadrons are properly simulated. The standard PYTHIA6.1 simulation is thus used for the description of the ΔR distribution.

7.2 Determination of the Beauty Fraction

In this section the fraction of electron candidates from beauty production will be determined by fitting the $p_{T,rel}$ distributions of the Monte Carlo simulations to the particles in the data that have passed the preselections summarised in table 8.1. The procedure described in section 7.2.2 of fitting several contributions to obtain the beauty hadron fraction has been used before in the H1-Experiment in the muon analyses [58] and [59].

Four contributions are considered: electrons from beauty and charm production, electrons from photon conversion processes (in light or heavy flavour processes) and misidentified hadrons in any process. Other contributions such as electrons from π^0-meson decays (Dalitz electrons) may be neglected because their cross sections and decay rates are much lower than the resulting uncertainty on the beauty electron fraction.

The fractions of the four contributions in the data are determined using Maximum Likelihood fits of the data and the Monte Carlo simulation histograms, respectively. The fits are based on Poisson distributions for data and Monte Carlo samples, using the method from Barlow [60].

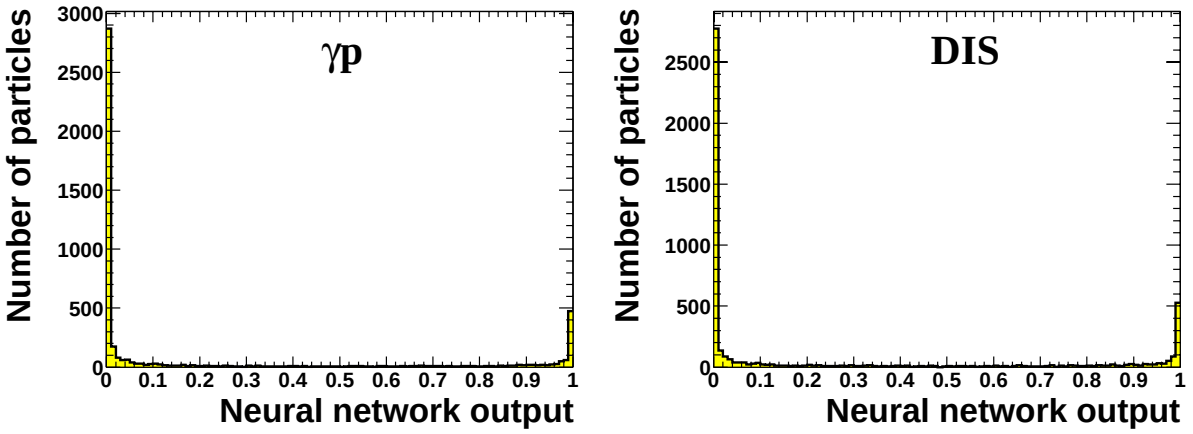

Figure 7.6: *Neural network output values for the photoproduction sample (left) and the DIS sample (right). Electron candidates are selected by requiring output values larger than 0.99.*

Input to the distributions are all particles passing the neural network output cut of 0.99. The output distributions are shown in figure 7.6 for the photoproduction data (left) and the DIS data (right). All particles with output values lower than 0.99 are rejected. More than 85% of the particles in the neural networks do not pass the output cut.

The following numbers of electron candidates are obtained for the two data samples:

- **Photoproduction:** 475 electron candidates,
- **DIS:** 514 electron candidates.

The fit to the $p_{T,rel}$ distributions cannot distinguish reliably between all the contributions. However, the fractions of photon conversion electrons and of misidentified hadrons are rather well defined by the ΔR and the E/p distributions. Thus, the strategy is to determine these contributions by fits to the ΔR and E/p distributions as will be described in the next section. The resulting values are then fixed for the determination of the beauty electron fraction with the $p_{T,rel}$ fit (section 7.2.2). The distributions used to fit the respective fractions of the four contributions are summarised in table 7.1.

	Fraction	**Fitted Distribution**
1	Beauty electrons	$p_{T,rel}$
2	Charm electrons	$p_{T,rel}$
3	Photon conversion electrons	ΔR
4	Misidentified hadrons	E/p

Table 7.1: *Overview of the individual contributions and of the distributions used to obtain their respective fractions.*

It should be kept in mind that the aim of the analysis is a determination of the beauty electron fraction. The determination of the other fractions is necessary for a proper beauty electron measurement. However, especially the fraction of charm electrons may not be very well determined. This question will be further addressed in sections 7.2.2.1 and 7.2.2.2.

7.2.1 Photon Conversion and Hadron Fractions

The fraction of photon conversion electrons in the data is determined by fitting the electron candidates' ΔR distribution to the Monte Carlo simulation predictions for beauty, charm and photon conversion electrons and hadrons, see figure 7.2 for the distributions.

The resulting photon conversion fraction is then used as a fixed value for a fit to the corresponding E/p distribution. Beauty and charm electrons show the same E/p distributions, so that only contributions from beauty and photon conversion electrons and misidentified hadrons are considered. The E/p distribution for photon conversion electrons is different from that of beauty and charm electrons as has been discussed in section 4.2.

The resulting value for the fraction of misidentified hadrons is then fixed for a repeated ΔR fit. Then, the fit to the E/p distributions is performed again as well, keeping the photon conversion fraction fixed.

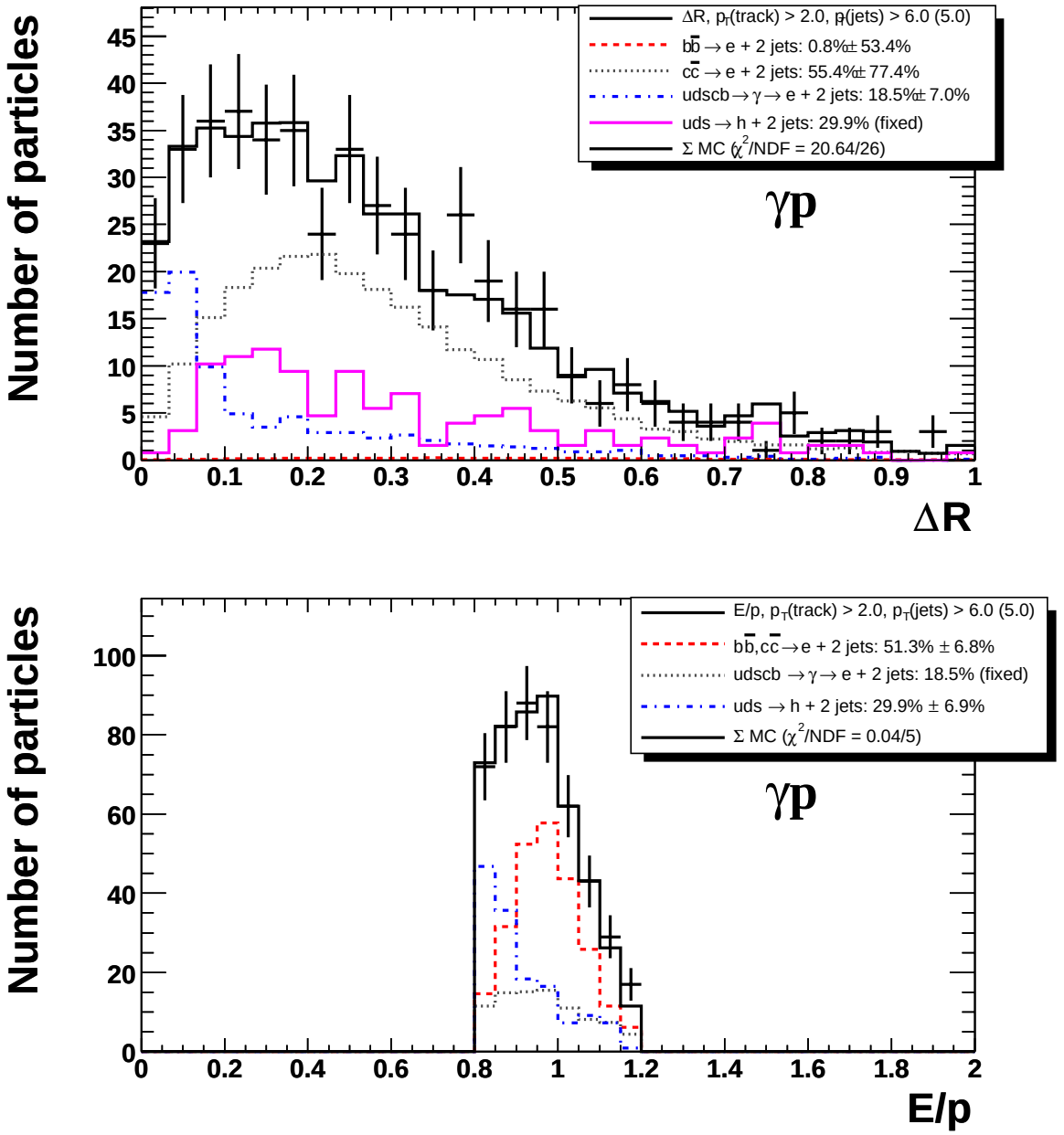

Figure 7.7: *Fits for the determination of the photon conversion fraction (upper plot) and the hadron fraction (lower plot) in the* ***photoproduction*** *sample. The ΔR distribution is fitted in order to obtain the photon conversion fraction. The hadron fraction is determined by fitting the E/p distribution. More details about the fit procedure can be found in the text.*

This procedure is repeated until stable results are obtained. As a cross check, the hadron and photon conversion fractions are varied within the fit uncertainties. The resulting distributions

	Electron candidates	**Photon conversion (ΔR)**	**Misidentified hadrons (E/p)**
Photoproduction	475	$18.5\% \pm 7.0\% \pm 3.0\%$	$29.9\% \pm 6.9\% \pm 3.0\%$
DIS	514	$22.0\% \pm 4.1\% \pm 2.5\%$	$20.5\% \pm 5.8\% \pm 2.5\%$

Table 7.2: *Fitted contributions of electrons from photon conversion processes and of misidentified hadrons. The second error describes the uncertainty due to the hadron fraction in the case of photon conversions, and vice versa. The uncertainties are slightly increased because the other parameter is fixed.*

are shown in figure 7.7 for the photoproduction sample and in figure 7.8 for the DIS sample. The black crosses are the data distributions. The solid black lines correspond to the predictions of the Monte Carlo simulations using the fitted fractions for the individual contributions. The final fit results are given in table 7.2. The second error in the table describes the uncertainty due to the hadron fraction in the case of photon conversions, and vice versa. The uncertainties are slightly increased because the other parameter is fixed.
It will be shown in section 7.2.2.1 that the beauty electron fraction is rather insensitive to the exact values of the photon conversion and the misidentified hadron fractions.

7.2.2 Beauty Fraction

The fractions of the photon conversion and hadron contributions are fixed for the fits to the $p_{T,rel}$ distributions. The results of these fits are beauty electron and charm electron fractions for the photoproduction and the DIS sample.

The fit distributions are shown in figure 7.9 for the photoproduction data and in figure 7.10 for the DIS data. The data are shown as the black crosses. The various lines show the individual contributions. The summed predictions of the Monte Carlo simulations using the fitted fractions are drawn as the solid black lines. The fit prediction and the data agree well for the photoproduction and the DIS data.

	Electron candidates	**Beauty electrons [%] ($p_{T,rel}$)**	**Charm electrons [%] ($p_{T,rel}$)**
Photoproduction	475	21.0 ± 5.2	31.5 ± 6.2
DIS	514	35.1 ± 6.0	21.9 ± 5.7

Table 7.3: *Fitted fractions of the beauty and charm electron contributions in the photoproduction and the DIS sample. The errors given for the beauty electron fraction include uncertainty estimates due to fixing the photon conversion and hadron fractions (see the next section).*

The measured beauty electron fractions are listed in table 7.3. The fractions are 4.0 standard deviations away from no beauty electron contributions in case of the photoproduction sample

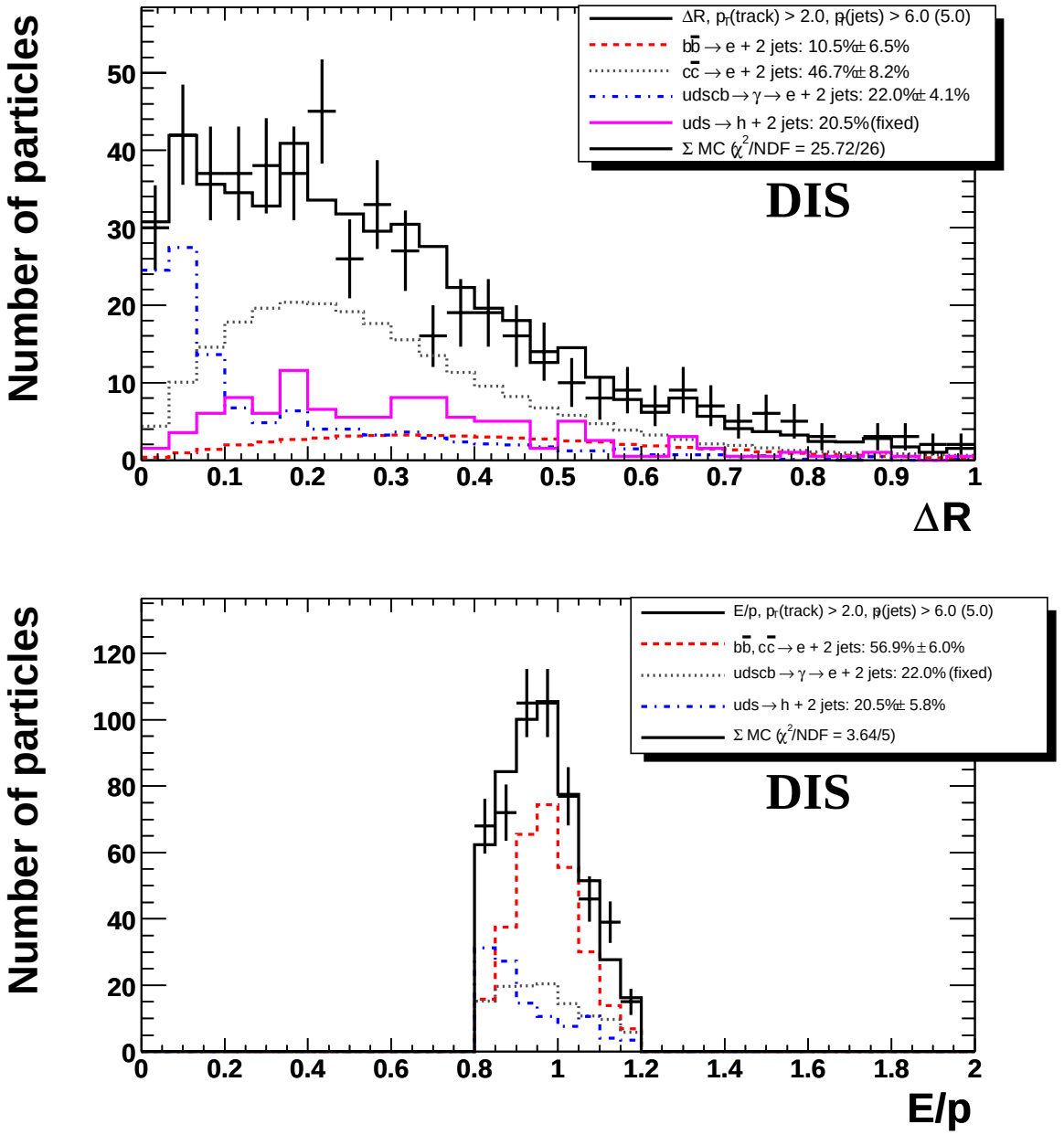

Figure 7.8: *Fits for the determination of the photon conversion fraction (upper plot) and the hadron fraction (lower plot) in the **DIS** sample. The ΔR distribution is fitted in order to obtain the photon conversion fraction. The hadron fraction is determined by fitting the E/p distribution. More details about the fit procedure can be found in the text.*

and 5.9 standard deviations in case of the DIS data, not including systematic uncertainties. (See section 8.4 for a discussion of systematic uncertainties.)

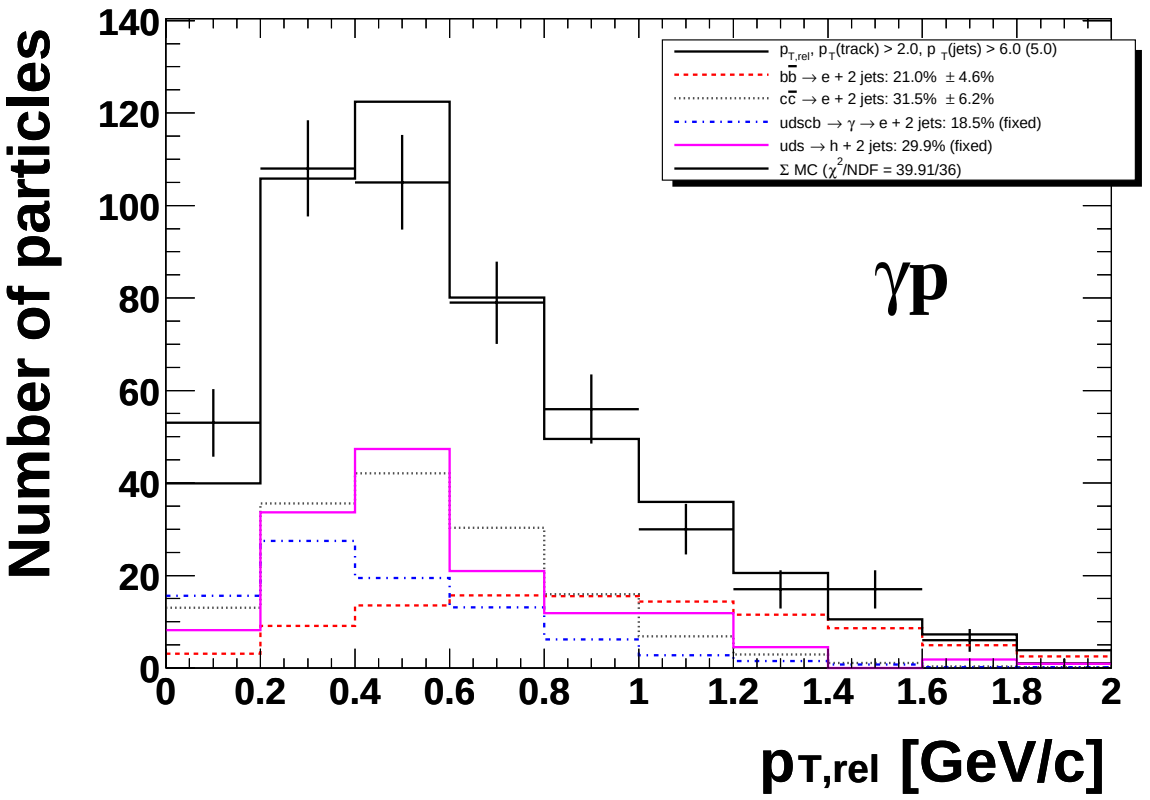

Figure 7.9: *Determination of the beauty electron fraction by fitting the $p_{T,rel}$ distribution for electrons from beauty, charm and photon conversion processes and for hadrons to the data in the* ***photoproduction*** *sample. The fractions determined for photon conversions and hadrons (see figure 7.7) are kept fixed in this fit. More details about the fit procedure can be found in the text.*

7.2.2.1 Stability of the Beauty Electron Fraction Determination

The stability of the beauty fraction determination using the $p_{T,rel}$ distribution is tested by varying the fixed fractions for photon conversion electrons and misidentified hadrons independently. The photon conversion fit inputs are varied by 50% and the fits to the E/p and $p_{T,rel}$ distributions are repeated. The hadron contributions are changed by 25% and the ΔR and $p_{T,rel}$ fits are repeated accordingly.

The results of these fits are summarised in table 7.4. The original beauty electron fractions are listed in the first data column. The changes to these fractions due to the varied photon conversion and hadron fractions are all within one standard deviation. It may thus be concluded that possible inaccurate determinations of the photon conversion and hadron fractions have a negligible impact on the beauty electron fraction. Instead, fluctuations in these contributions affect the fraction of charm electrons.

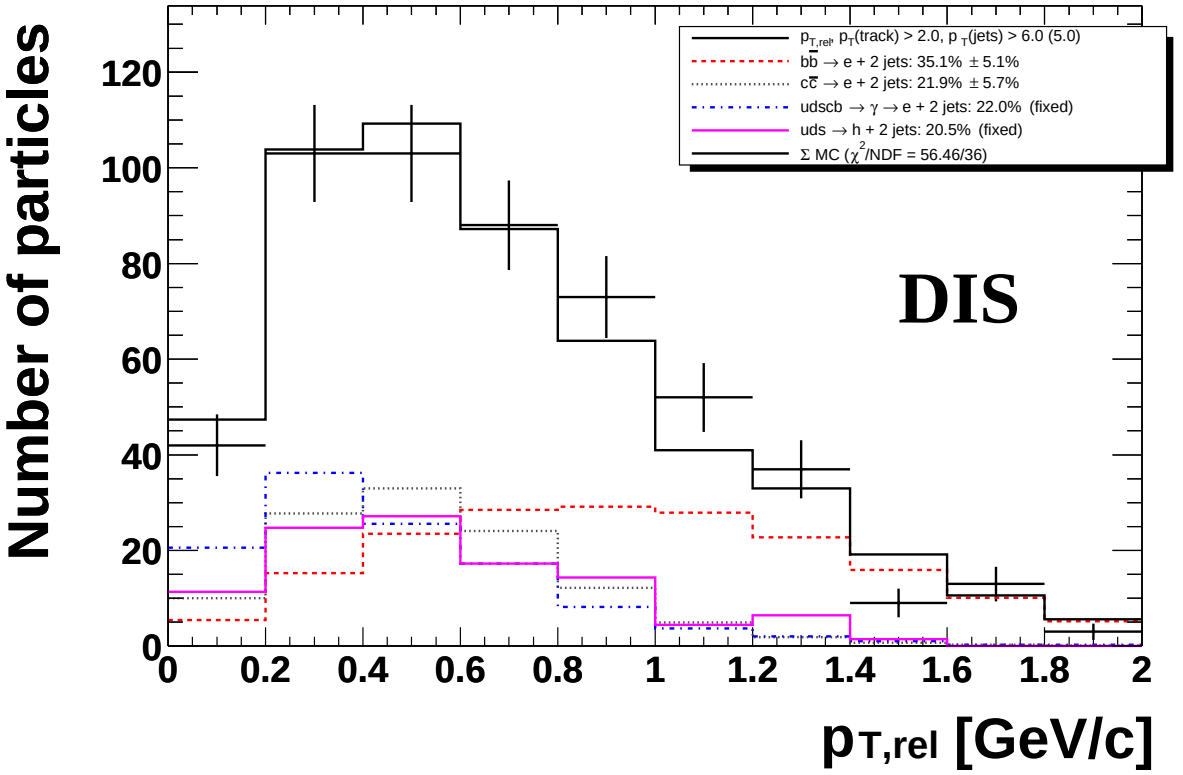

Figure 7.10: *Determination of the beauty electron fraction by fitting the $p_{T,rel}$ distribution for electrons from beauty, charm and photon conversion processes and for hadrons to the data in the **DIS** sample. The fractions determined for photon conversions and hadrons (see figure 7.8) are kept fixed in this fit. More details about the fit procedure can be found in the text.*

The observed shifts in the beauty electron fraction are used to estimate the additional uncertainty on the beauty electron fraction since the photon conversion and the hadron fractions are fixed in the $p_{T,rel}$ fit. Thus, the uncertainty on the beauty electron fraction increases by approximately 10%. The uncertainties given in table 7.3 include these contributions.

7.2.2.2 Cross Check of the Fraction Determination

The accuracy of the fit procedure described in this section is tested with a PYTHIA Monte Carlo simulation (listed in line 6 of table 3.3). The simulation is treated as data and all cuts are applied. The resulting fit fractions are compared with the fractions obtained by counting the respective contributions.

The fit to the $p_{T,rel}$ distribution is shown in figure 7.11. The Monte Carlo data are shown as the black crosses, the solid black line represents the fit prediction for the sum of the individual fractions. The fitted beauty electron fraction amounts to $22.8\% \pm 2.7\%$, the true beauty electron fraction is 21.4%.

Fraction	**Photoproduction**				
Photon conversion	18.5%	0.5 · 18.5%	1.5 · 18.5%	18.5%	18.7.0%
Hadrons	29.9%	33.3%	26.8%	0.75 · 29.9%	1.25 · 29.9%
Beauty electrons	21.0% ± 4.6%	20.4% ± 4.7%	21.6% ± 4.6%	20.9% ± 4.4%	21.1% ± 4.6%
	DIS				
Photon conversion	22.0%	0.5 · 22.0%	1.5 · 22.0%	22.7%	22.9%
Hadrons	20.5%	25.7%	16.3%	0.75 · 20.5%	1.25 · 20.5%
Beauty electrons	35.1% ± 5.1%	32.5% ± 5.2%	36.7% ± 5.0%	36.0% ± 4.9%	32.3% ± 6.1%

Table 7.4: *Changes in the fraction of electrons from beauty production with variations of the fitted fractions for electrons from photon conversions and misidentified hadrons. The photon conversion fractions are varied up and down by 50%, the hadron fractions are varied by 25%. The resulting shifts for the beauty electron fraction are all within one standard deviation.*

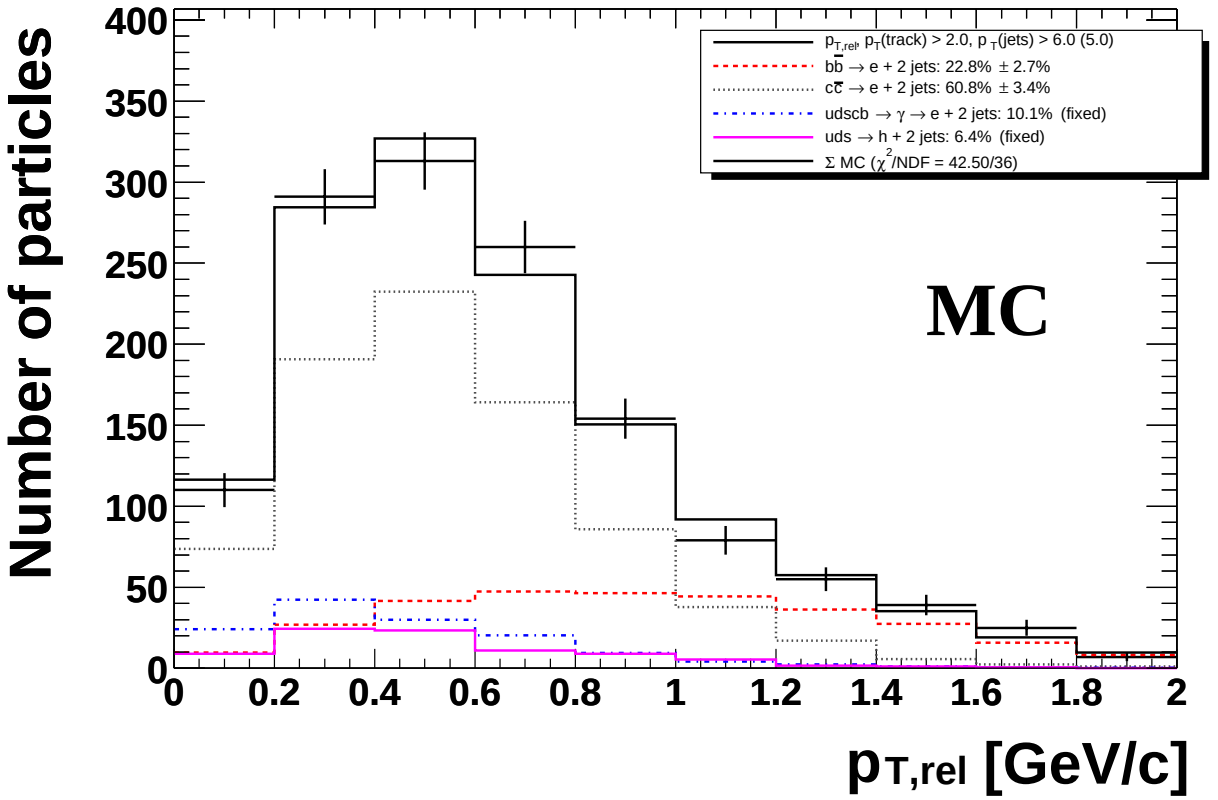

Figure 7.11: *Cross check of the beauty electron fraction determination in a Monte Carlo simulation. The fit procedure is performed as in data, see the text for more details. The fitted beauty electron fraction of 22.8% ± 2.7% matches the true fraction in the sample of 21.4% very well.*

The fitted fractions for the four relevant contributions are compared to the Monte Carlo contents in table 7.5. It can be seen that the fitted hadron fraction comes out too low which in turn results in a slightly high charm electron fraction. The fitted beauty electron fraction is however not significantly affected by this as has already been shown in the previous section.

Fraction	MC contents	Fit
Photon conversion	13.9%	10.1% ± 2.1%
Hadrons	11.1%	6.4% ± 3.0%
Charm electrons	53.6%	60.8% ± 3.4%
Beauty electrons	21.4%	22.8% ± 2.7%

Table 7.5: *Comparison of the true fractions in a PYTHIA Monte Carlo simulation to the fractions fitted using the procedure described in the text. The beauty electron fraction is well determined whereas the hadron fraction is slightly too low, leading to a high charm electron fraction.*

7.2.2.3 Control Plots

In this section the distributions for several kinematical variables in the two data samples will be compared to the predictions of the Monte Carlo simulations using the fitted fractions for the corresponding contributions. PYTHIA Monte Carlo simulations are taken in case of the photoproduction sample and RAPGAP simulations are chosen for the comparison with the DIS data.

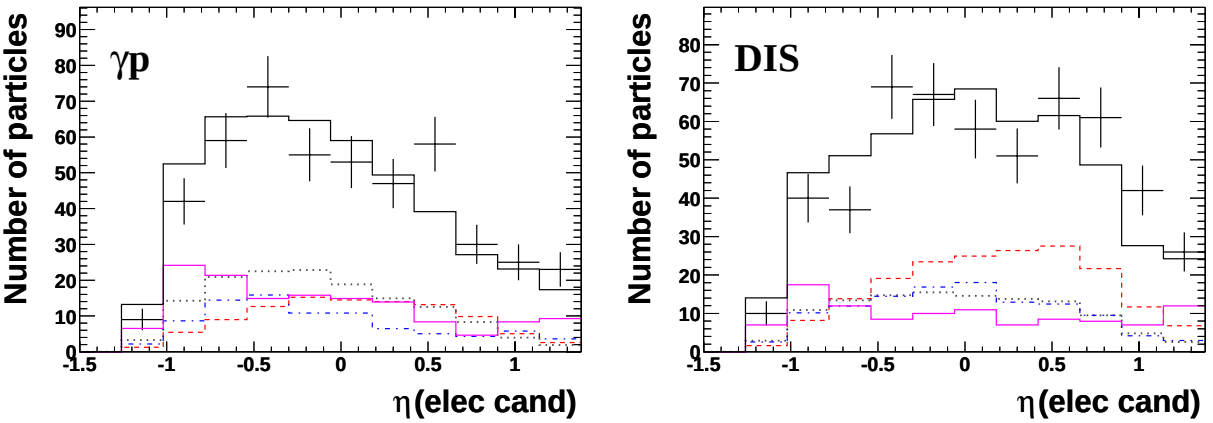

Figure 7.12: *Comparison of the η distribution for electron candidates in data (crosses) with the predictions from the Monte Carlo simulations using the fitted fractions for the individual contributions. The line styles are identical to those in the fit figures 7.7 – 7.11. The photoproduction sample is shown on the left side, the DIS sample on the right side.*

The line styles in the figures are chosen as in the previous figures, see e. g. figure 7.11. The data are shown as the black crosses, the sums of the Monte Carlo simulations are represented by the solid black lines.

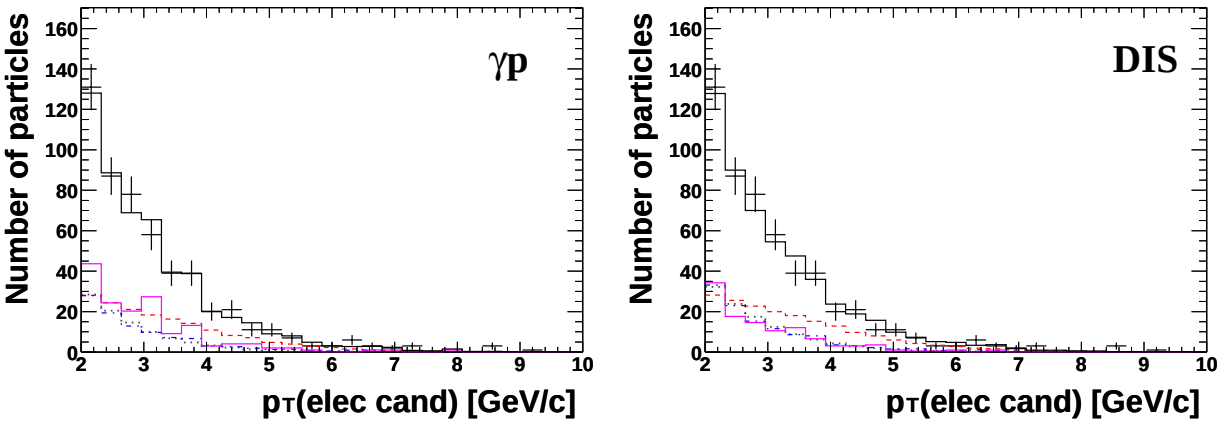

Figure 7.13: *Comparison of the p_T distribution for electron candidates in data (crosses) with the predictions from the Monte Carlo simulations using the fitted fractions for the individual contributions. The line styles are identical to those in the fit figures 7.7 – 7.11. The photoproduction sample is shown on the left side, the DIS sample on the right side.*

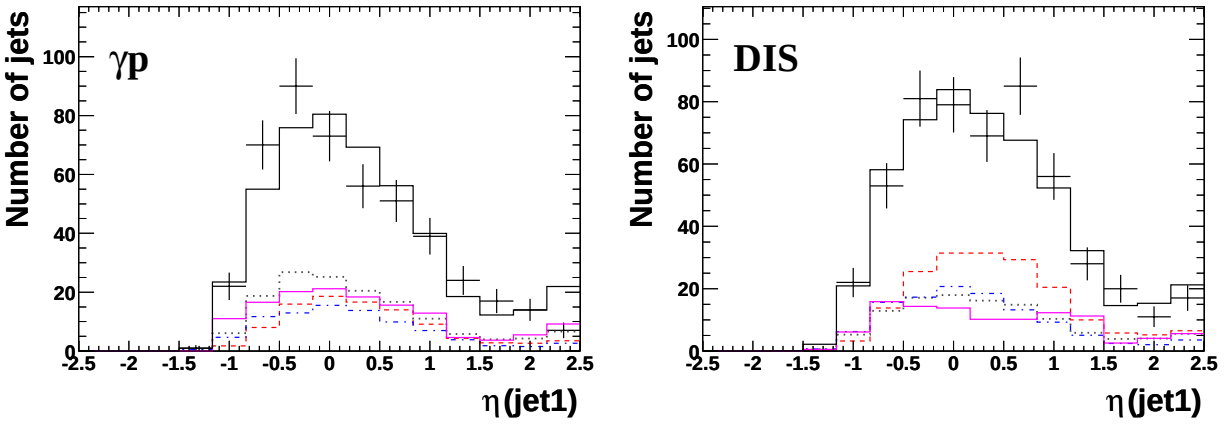

Figure 7.14: *Comparison of the η distribution for the highest p_T jet in data (black crosses) with the predictions from the Monte Carlo simulations using the fitted fractions for the individual contributions. The line styles are identical to those in the fit figures 7.7 – 7.11. The photoproduction sample is shown on the left side, the DIS sample on the right side.*

The η distributions of the electron candidates are shown in figure 7.12 for the photoproduction sample (left) and the DIS sample (right). The corresponding p_T distributions are shown in figure 7.13, with the photoproduction data being on the left hand side and the DIS data on the right hand side. All distributions are reasonably well described by the simulations.

Figure 7.14 shows the η distributions for the jet with the highest transverse momentum in an event. The photoproduction distribution is shown on the left, the DIS distribution on the right. The data are well described by the simulations in both cases. The p_T distributions for these jets are shown in figure 7.15. The data distributions are equally well described by the simulations.

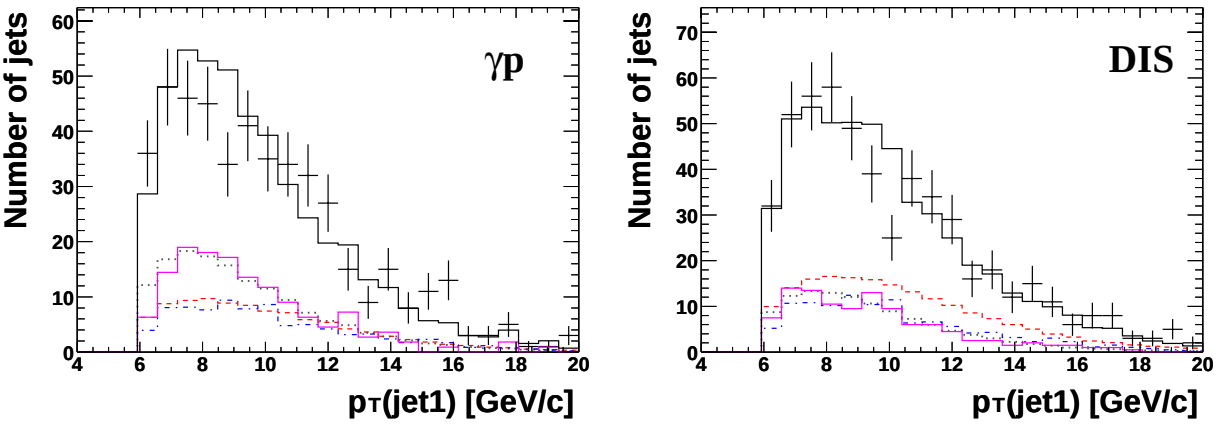

Figure 7.15: *Comparison of the p_T distribution for the highest p_T jet in data (black crosses) with the predictions from the Monte Carlo simulations using the fitted fractions for the individual contributions. The line styles are identical to those in the fit figures 7.7 – 7.11. The photoproduction sample is shown on the left side, the DIS sample on the right side.*

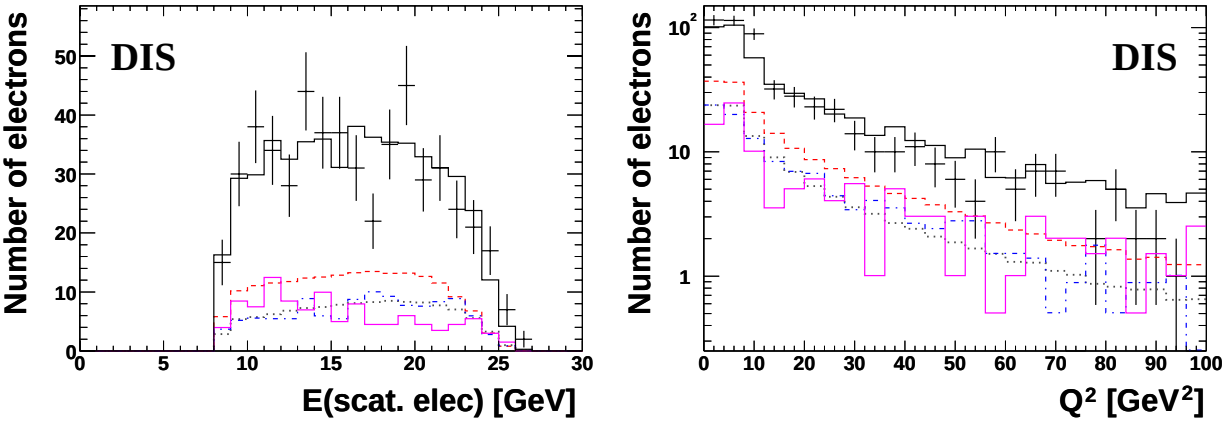

Figure 7.16: *Comparison of the scattered electron energy distribution (left) for the DIS data (black crosses) with the predictions from the Monte Carlo simulations using the fitted fractions for the individual contributions. The corresponding Q^2 distributions are shown on the right hand side. The line styles are identical to those in the fit figures 7.7 – 7.11.*

The scattered electron energy distribution is shown in figure 7.16 (left) for the DIS data. The Monte Carlo simulations describe the data reasonably well. It is interesting to note that the distribution is flat and does not exhibit the rise towards high electron energies as is observed for example in a measurement of D^*-mesons with jets in DIS ([61]). This is because much energy is needed for the production of the heavy quark pair. The corresponding Q^2 distribution is shown on the right hand side of this figure. The contribution at low Q^2 seems to be slightly underestimated by the Monte Carlo simulations.

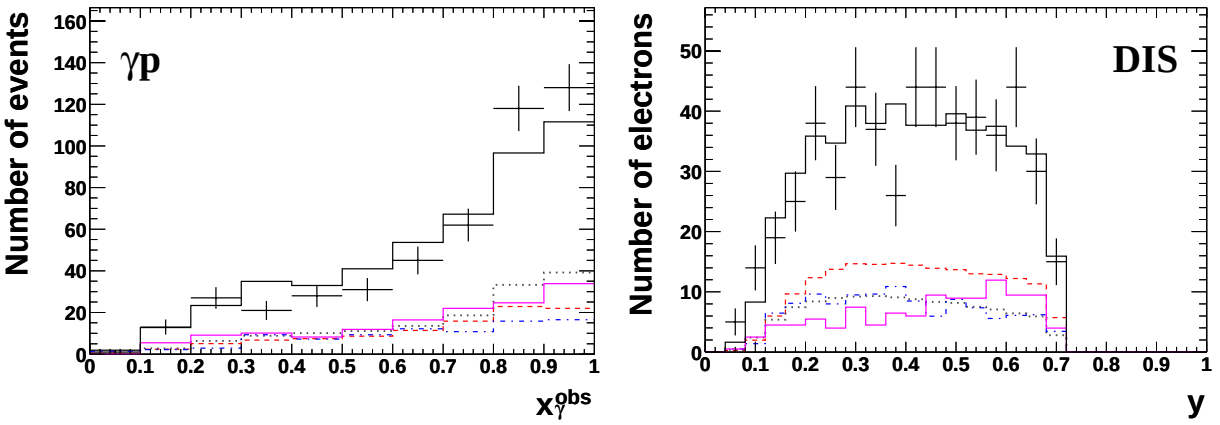

Figure 7.17: *Comparison of the x_γ^{obs} distribution in the photoproduction sample (left) with the predictions from the Monte Carlo simulations using the fitted fractions for the individual contributions. The distribution for the inelasticity in the DIS sample is shown on the right. The line styles are identical to those in the fit figures 7.7 – 7.11.*

The distribution of the reconstructed x_γ, the fraction of the photon's energy entering the hard interaction, is shown on the left hand side of figure 7.17 for the photoproduction data. It is defined as

$$x_\gamma^{obs} = \frac{\sum_{jet1}(E - p_z) + \sum_{jet2}(E - p_z)}{\sum_{HFS}(E - p_z)}, \tag{7.3}$$

with E and p_z being the energy and the z-component of the particles' momenta in the two jets and in the Hadronic Final State (see also section 3.1.1). Events with direct processes have $x_\gamma^{obs} \approx 1$, resolved processes show $x_\gamma^{obs} < 1$ because the photon remnants carries away energy. The x_γ^{obs} distribution is not perfectly described, the data seem to contain more direct processes than predicted by the Monte Carlo simulations.

The inelasticity distribution measured via the scattered electron in the SpaCal is shown on the right hand side of figure 7.17 for the DIS data. The data distribution is well described by the Monte Carlo simulations.

7.2.3 Impact Parameter Method

An alternative method for the determination of the beauty electron fraction is fitting the impact parameter distributions instead of using $p_{T,rel}$ distributions. The impact parameter is defined as the distance between the electron candidate's track and the primary vertex in the xy-plane. The sign of the impact parameter is positive if the track passes the jet axis in positive jet direction.

Using the impact parameter as a discriminating variable makes use of the different lifetimes of the individual contributions. Hadrons from light quark decays are produced at the primary vertex and thus show small impact parameters whereas electrons from beauty hadron decays have large impact parameters because of the beauty hadrons longer lifetimes. The impact parameter distribution for electrons from charm hadron decays is found in between.

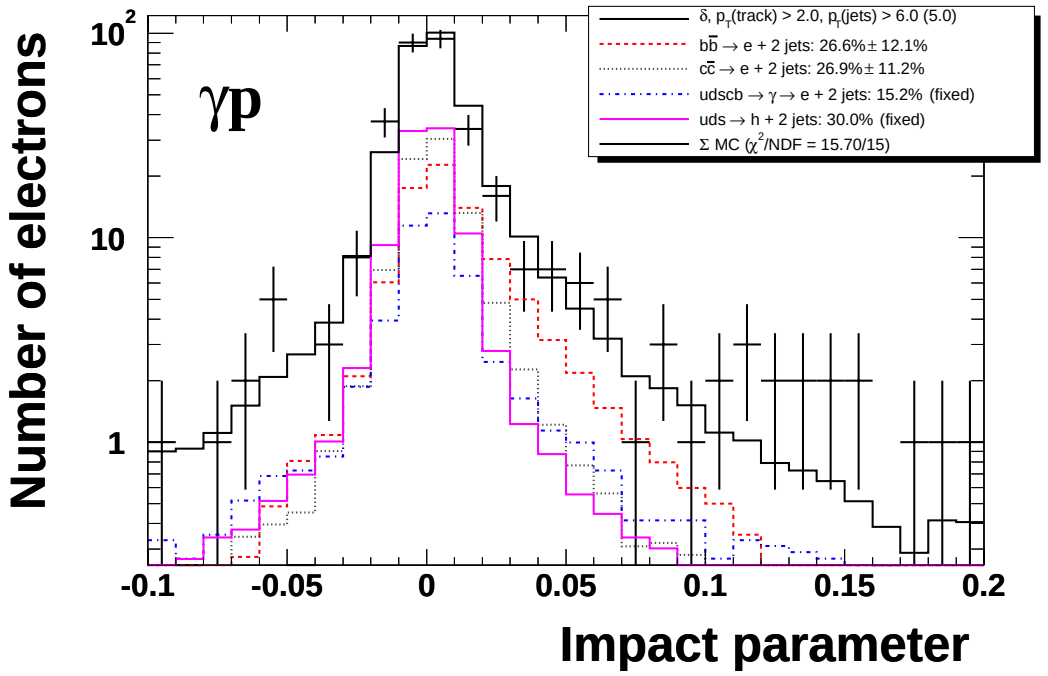

Figure 7.18: *Determination of the beauty electron fraction in the photoproduction sample by fitting the impact parameter distribution instead of* $p_{T,rel}$.

The impact parameter method requires a measurement of the track by the vertex detector CST (see section 2.3). This requirement and the smaller polar angle acceptance of the CST compared to the CJC leads to a reduction of electron candidates as can be seen when comparing the first data row in table 7.6 with that of table 7.3.

	Electron candidates	**Beauty electrons [%] (Impact parameter)**	**Charm electrons [%] (Impact parameter)**
Photoproduction	337	26.6 ± 12.1	26.9 ± 11.2
DIS	368	56.4 ± 32.9	3.4 ± 11.8

Table 7.6: *Fitted fractions of the beauty and charm electron contributions in the photoproduction and the DIS sample when fitting the impact parameter distributions.*

The impact parameter fit distributions with fixed photon conversion and hadron fractions are shown in figure 7.18 for the photoproduction sample. The resulting beauty and charm electron fractions are given in table 7.6 for the photoproduction and the DIS sample. The uncertainties on these fractions are much larger than for the $p_{T,rel}$ fits so that the impact parameter method will not be pursued here any further.

The impact parameter and the relative transverse momentum are used as complementary information in the muon analysis [8]. A two dimensional fit is performed such that the beauty muon fraction can be determined with greater accuracy.

Chapter 8

Cross Sections

In this chapter cross sections will be determined for the photoproduction and the DIS sample. Before, reconstruction and trigger efficiencies will be studied for both samples and systematic uncertainties will be evaluated.

8.1 Cross Section Definition

The cross section in the visible range is defined as

$$\sigma_{vis} = \frac{N}{\mathcal{L}_{int} \cdot \epsilon} \tag{8.1}$$

with N being the number of reconstructed signal events and $\mathcal{L}_{int}$ being the integrated luminosity. The efficiency that a signal event is triggered, has passed the L4-finders and is reconstructed is denoted with ϵ. In the following these efficiencies will be treated individually: $\epsilon = \epsilon_{rec} \cdot \epsilon_{trig} \cdot \epsilon_{L4}$.

The visible range is given by kinematical cuts and detector acceptances. The given cross sections are not corrected for the branching ratio $\mathcal{B}R(b \to e)$ and are not extrapolated to the full phase space. Thus, the cross section definition is:

$$\sigma_{vis}(ep \to eb\bar{b} \to ejjeX) = \frac{N}{\mathcal{L}_{int} \cdot \epsilon_{rec} \cdot \epsilon_{trig} \cdot \epsilon_{L4}} \tag{8.2}$$

Cross sections cannot be given in bins of kinematical variables, e. g. $\eta(electron)$, since the overall event statistics is too low to perform the fits for the beauty electron fraction determination on such subsamples.

8.2 Event Selection and Visible Ranges

The event selections restricting the visible range for the photoproduction and the DIS analysis are summarised in table 8.1. The preselections of the data are explained in sections 3.2 and 6.1.2.

The restriction of the ϑ range for the electrons to $28° - 145°$ follows from the requirement that the electron candidates enter the LAr calorimeter in one of the 4 wheels *CB1 – FB1*.

		Photoproduction	**DIS**
Event selection	Data	1999 e^+p, 2000	
	Subtrigger	83	61
	$E(scattered\ electron)$ [GeV]	–	8
	abs. z-position vertex [cm]	< 35	
	Neural Network output	> 0.99	
Visible kinematic range	$p_T(electron)$ [GeV/c]	> 2.0	
	$\vartheta(electron)$ [°]	$28 < \vartheta < 145$	
	Number of jets	≥ 2	
	$p_T(jet1)$, $p_T(jet2)$ [GeV/c]	$> 6, > 5$	
	$\eta(jets)$	$-2.5 < \eta < 2.5$	
	Inelasticity	$0.29 < y < 0.65$	$0.05 < y < 0.7$
	Q^2 [GeV^2]	(effectively < 0.01)	$2 < Q^2 < 100$

Table 8.1: *Definition of the event selection and of the visible kinematic range for the photoproduction and the DIS sample.*

8.3 Efficiencies

The number of reconstructed signal events is corrected by the probabilities for triggering and reconstructing these events. The efficiencies are determined using Monte Carlo simulations; cross checks with data samples are done where applicable.

8.3.1 Reconstruction Efficiencies

The reconstruction efficiency is defined as

$$\epsilon_{rec} = \frac{N^{rec}|_{vis}}{N^{gen}|_{vis}} \tag{8.3}$$

with $N^{rec}|_{vis}$ and $N^{gen}|_{vis}$ being the reconstructed and the generated signal events in the visible range, respectively. The following individual efficiencies are summarised in the signal event reconstruction efficiency:

- electron track reconstruction,
- electron passing the preselection based on calorimeter energy, listed in table 5.1,
- electron passing the neural network,
- ≥ 2 jets per event,
- scattered electron identified in the SpaCal (in case of DIS).

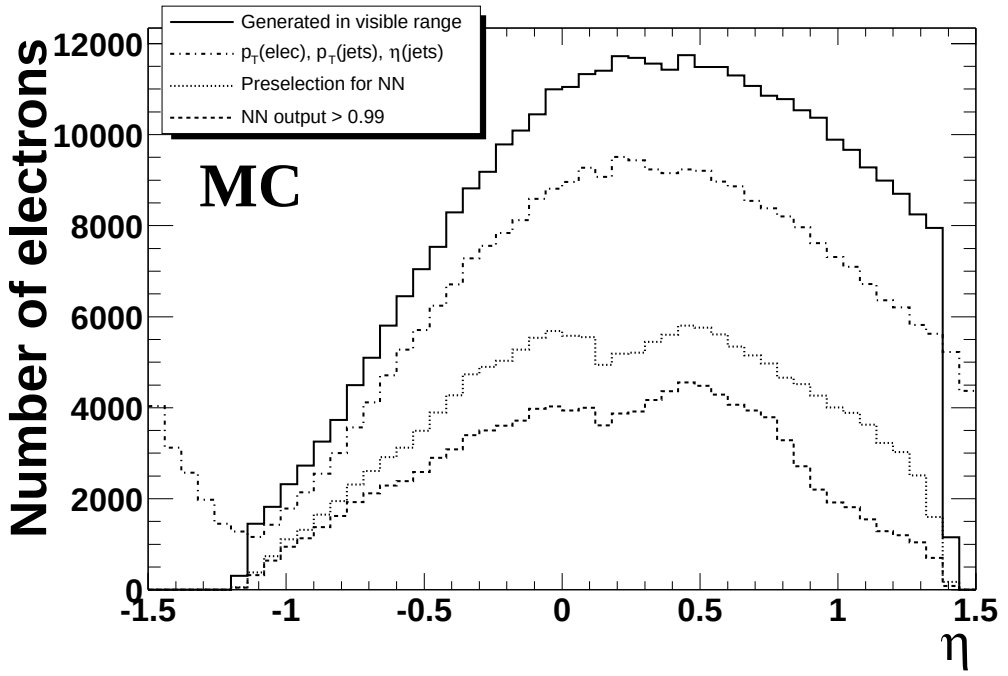

Figure 8.1: *Most important contributions to the reconstruction efficiencies of electrons in dijet events in dependence of $\eta(electron)$ for a PYTHIA Monte Carlo simulation.*

A PYTHIA Monte Carlo simulation is used for the determination of ϵ_{rec} in the photoproduction sample, RAPGAP is used for the DIS data. CASCADE Monte Carlo simulations are used for both data sets. The number of successfully reconstructed signal events is obtained by counting the events so that no additional uncertainty is introduced by fitting the distributions.

The contributions of the most important cuts are illustrated in figure 8.1 for electrons in a PYTHIA Monte Carlo simulation. The electrons generated within the visible range are shown as the solid line. The η distribution of electrons after detector simulation and reconstruction and after the application of the cuts on the electron and the jet kinematics is shown with the dash-dotted line. The dotted line represents the electrons passing the initial neural network cuts (see section 6.1.2). Electrons passing the neural network output cut of 0.99 are shown as the dashed line.

The resulting reconstruction efficiencies are listed in table 8.2. The uncertainties given are the statistical binomial errors.

The uncertainties of the reconstruction efficiency will be discussed in section 8.4.1 together with the uncertainty of the electron identification.

Monte Carlo	Photoproduction	DIS
PYTHIA	35.28% ± 0.21%	–
RAPGAP	–	32.02% ± 0.08%
CASCADE	36.38% ± 0.26%	28.83% ± 0.23%

Table 8.2: *Reconstruction efficiencies ϵ_{rec} for the photoproduction and the DIS sample determined with the Monte Carlo simulations listed in the left column.*

8.3.2 Trigger Efficiencies

The trigger efficiency is defined as the ratio of reconstructed events triggered by a subtrigger to the total number of reconstructed events:

$$\epsilon_{trig} = \frac{N^{rec,trig}|_{vis}}{N^{rec}|_{vis}} \tag{8.4}$$

It is determined from the Monte Carlo simulations already used in the previous sections by counting signal events.

A cross check of the trigger efficiency is performed using data triggered with subtrigger 0 which primarily has a condition on the energy in the SpaCal (`SPCLe_IET>2`, see section 3.1.1). It does not include the trigger elements to be tested, `DCRPh_THigh`, `DCRPh_Tc`, `zVtx_sig` and `zVtx_sig_1`. The main problem with determining the trigger efficiency from data samples is that the event sample composition is different from the signal events, leading to different η distributions or particle multiplicities. In addition the neural networks are not applied to this sample as there is not enough statistics available.

8.3.2.1 Subtrigger 61

The important trigger elements of subtrigger 61 concern the scattered electron energy reconstruction in the SpaCal (`SPCLe_IET`, `SPCLe_IET_Cen_3`), the detection of a central vertex and of central tracks (`zVtx_sig`, `DCRPh_THigh`) as has been explained in section 3.1.1.

The energy which is required for a scattered electron in this analysis is 8 GeV which is well above the threshold of 6 GeV for the subtrigger. In addition, the possibly inefficient inner region of the SpaCal, corresponding to Q^2 values lower than 2 GeV^2, is not used in the analysis. So, an efficiency of 100% is assigned in accordance with other analyses, e. g. ([62]).

The efficiencies of the track related trigger elements are listed in table 8.3. Deviations of a few percent are observed between the two Monte Carlo simulations and the monitor data sample. A systematic uncertainty of 3% is assigned as in [8].

8.3.2.2 Subtrigger 83

The main trigger elements of subtrigger 83 as listed in section 3.1.2 are `LU_ET` && `not LU_PD_low` for the identification of the scattered electron in the electron tagger ET33 and `zVtx_sig_1`,

	zVtx_sig	DCRPh_THigh	S61
RAPGAP	$96.15\% \pm 0.02\%$	$98.09\% \pm 0.02\%$	$94.42\% \pm 0.03\%$
CASCADE	$94.92\% \pm 0.07\%$	$95.97\% \pm 0.07\%$	$91.47\% \pm 0.09\%$
Data (S0)	$89.12\% \pm 0.14\%$	$96.64\% \pm 0.08\%$	$89.12\% \pm 0.14\%$

Table 8.3: *Efficiencies for the track related trigger elements and the complete subtrigger 61. S0 is used as the reference subtrigger in the data samples.*

DCRPh_Tc for the detection of central tracks. The efficiency of the ET33 is included in its acceptance (see figure 3.1) which will be discussed in section 8.5. The photon detector is assumed to be 100% efficient.

	zVtx_sig_1	DCRPh_Tc	S83
PYTHIA	$96.17\% \pm 0.03\%$	$98.21\% \pm 0.02\%$	$94.54\% \pm 0.03\%$
CASCADE	$96.45\% \pm 0.04\%$	$98.16\% \pm 0.03\%$	$94.73\% \pm 0.05\%$
Data (S0)	$90.60\% \pm 0.13\%$	$92.20\% \pm 0.12\%$	$84.77\% \pm 0.16\%$

Table 8.4: *Efficiencies for the track related trigger elements and the complete subtrigger 83.*

The trigger efficiencies determined with the PYTHIA and the CASCADE Monte Carlo simulation are listed in table 8.4. Both simulations result in equal efficiencies which are however 6% higher than in the data for each of the two trigger elements. A systematic uncertainty of 5% is assigned.

8.3.2.3 L4-Finders

It has already been discussed in section 3.2 that all events in the photoproduction and the DIS sample have been accepted by one of the various L4-finders (see section 2.6). None of the events has L4-weights, therefore the efficiency ϵ_{L4} is assumed to be 100% and no systematic uncertainty is assigned.

8.4 Systematic Uncertainties

When evaluating systematic uncertainties one has to distinguish between "systematic effects" and "systematic mistakes" ([63], [64]). A common contribution to the former are uncertainties in calorimeter calibration or detector alignment. The effects of these uncertainties on the result of the analysis have to be evaluated and taken into account for the sum of the systematic uncertainties. With regard to the latter contribution, "blind checks" have to be performed. If the analysis passes a specific test, no uncertainty must be added. If a test fails and neither the test nor the analysis procedure are proven to be wrong, the systematic uncertainty has to be evaluated as well.

When a systematic difference is obtained by comparing two Monte Carlo simulations, the difference between the results is divided by $\sqrt{2}$ if the models are considered to be "typical". In contrast, models are considered "extreme" when it is known that the result lies within the range given by the two models.

8.4.1 Study of Systematic Effects

Here, systematic effects on the analysis will be evaluated. Known sources of this kind are the energy scales of the calorimeters, the alignment of the SpaCal and the branching ratio from beauty hadrons to electrons.

The energy scale of the LAr calorimeter is known to an accuracy of 2% in the electromagnetic section and to 4% in the hadronic part. The resulting uncertainty for the analysis is evaluated by shifting all cell energies by the respective amount. The shifts in the electromagnetic and in the hadronic LAr energies are applied both individually and in combination in all directions. The analysis is redone completely for all 8 possibilities and the numbers of electron candidates is compared to the regular analysis. The largest deviations found are +4% (by a shift +2% for the electromagnetic scale) and -6.5% (by a shift of -2% for the hadronic scale and -4% for the hadronic scale) in case of the photoproduction sample and +2.5% (by a shift of +2% for the electromagnetic scale) and -4.3% (by a shift of -2% for the electromagnetic scale) in case of the DIS sample. Thus, an uncertainty of 5.3% is assigned for the photoproduction data and 3.4% for the DIS data (line 1 in table 8.5).

Precise knowledge of the energy scale of the electromagnetic section of the SpaCal and of the SpaCal's spatial position is important for the selection of the scattered electron and for the calculation of Q^2 and y. The electromagnetic energy scale is known to an accuracy of 0.3% at 27 GeV and to 2% at 7 GeV and a linear behaviour in between can be assumed ([65]). All electromagnetic SpaCal energies are shifted upwards and downwards accordingly and the analysis is redone; Q^2 and y are recalculated. As a result, the number of electron candidates changes by +1.56% and -1.36% and an uncertainty of 1.5% is assigned (line 2 in table 8.5).

The impact of the uncertainty in the spatial alignment of the SpaCal is determined by shifting the scattered electron's position by ± 1 mrad. A shift of +1 mrad leads to 0.78% less electron candidates. A plus of 1.95% in the number of electron candidates is obtained when shifting by -1 mrad. A systematic uncertainty of 1.4% is assigned on the DIS sample (line 3 in table 8.5).

The effect of the uncertainty of the electron energy measured by the electron tagger ET33 is obtained by following the procedure described in [37]. The electron energy is varied by $\pm 1.5\%$ and the data are selected again. Variations in the energy scale lead to changes in the y distribution and thus to different numbers of electron candidates. In addition, the mean acceptance of the ET33 (see section 8.5) changes. An energy shift of +1.5% leads to a 2.74% smaller cross section while a shift of -1.5% results in a 2.32% higher value so that a systematic uncertainty of 2.5% is assigned (line 4 in table 8.5).

The uncertainty on the branching ratio from the direct decay of heavy quarks via a $W^{\pm}$-boson is taken from [12], see section 1.2: $\mathcal{B}R(b, c \to e) = 10.72\% \pm 0.16\%$. The value given in line 5 in table 8.5 includes both the direct decay $b\bar{b} \to e$ from a beauty quark pair into an electron as well as the cascade decay $b\bar{b} \to c \to e$.

8.4.2 Testing for Systematic Mistakes

In this section checks are performed to test the analysis for systematic mistakes; systematic uncertainties are evaluated where needed.

The stability of the electron fraction determination was successfully tested in section 7.2.2.1. It was also shown that the true beauty electron fraction is well determined by the method (see section 7.2.2.2). The control plots presented in section 7.2.2.3 have shown reasonable agreement between data and Monte Carlo simulations.
However, the electron identification efficiency strongly depends on η because of the different geometries in the LAr wheels, see the left histogram in figure 6.5. So, as a test, the simulated η distribution of the electrons is modified in the Monte Carlo simulations by shifting 10% of the electrons from the LAr wheel CB3 to the LAr wheel FB1 and vice versa. The resulting differences in the reconstruction efficiencies are used to estimate the systematic uncertainty. A value of 2% is found for the photoproduction and the DIS analysis.
The differences in the signal reconstruction efficiencies obtained by the individual Monte Carlo simulations are used to evaluate the uncertainties on the reconstruction efficiencies (see table 8.2). A signal event is defined to contain one electron and two jets within the visible range. The track reconstruction efficiency is not included in the reconstruction efficiency (see below).
It is assumed that PYTHIA/CASCADE and RAPGAP/CASCADE present "typical" models (see above) and the systematic uncertainty is obtained by dividing the difference between the single efficiencies by $\sqrt{2}$. The resulting uncertainties are 0.8% for the photoproduction analysis and 2.26% for the DIS analysis. The total systematic uncertainty on the reconstruction efficiency is obtained by adding the 2% determined above to these values in quadrature, leading to 2.2% for the photoproduction sample and 3.0% for the DIS sample (line 6 in table 8.5).

Important event selection cuts such as on the transverse momentum of the electron candidate or on the two jets have been varied. Significant deviations from the regular analysis were not found and no systematic uncertainty is assigned.

The $p_{T,rel}$ distribution which is closely related to the reconstruction of the jet axis is a very important variable for the determination of the beauty electron fraction. Tests were performed by smearing the jet axis by 5 – 10% in η and φ and the corresponding fits to the $p_{T,rel}$ distribution were done again. None of the resulting beauty electron fractions was found to deviate more than one standard deviation from the regular analysis so that no systematic uncertainty has been assigned.

The ΔR distributions, relevant for the determination of the photon conversion and hadron fractions, have been checked to be properly simulated by the Monte Carlo simulations and no systematic uncertainty has been assigned.

The dependence of the beauty electron fractions on the Monte Carlo models is tested by comparing the fit results when using PYTHIA or CASCADE (photoproduction) and RAPGAP or CASCADE (DIS). The fitted beauty electron fractions are:

- PYTHIA: $21.0\% \pm 5.2\%$ vs. CASCADE: $18.0\% \pm 4.2\%$ (photoproduction)
- RAPGAP: $35.1\% \pm 6.0\%$ vs. CASCADE: $34.6\% \pm 4.8\%$ (DIS)

The fractions obtained agree within the uncertainties. As a result, no systematic uncertainty on the Monte Carlo model is assigned.

A systematic uncertainty on the track reconstruction efficiency of 3% is assigned in accordance with other analyses ([62]), see line 7 in table 8.5.

The systematic uncertainties of the trigger efficiencies have already been discussed in sections 8.3.2.1 (S61) and 8.3.2.2 (S83). Uncertainties of 5% for the photoproduction analysis and of 3% for the DIS analysis are assigned (line 8 in table 8.5).

No systematic uncertainty is assigned for the efficiency of the L4-finders, see section 8.3.2.3.

The integrated luminosity is determined with an uncertainty of 1.5% ([66]).

	Source	**Photoproduction**	**DIS**
1	LAr calibration	5.3%	3.4%
2	SpaCal calibration	–	1.5%
3	SpaCal alignment	–	1.4%
4	Energy scale ET33	2.5%	–
5	Branching ratio $b\bar{b} \to e$	0.3%	0.3%
6	Reconstruction efficiency	2.2%	3.0%
7	Track reconstruction	3.0%	3.0%
8	Trigger efficiency	5.0%	3.0%
9	Luminosity	1.5%	1.5%
Sum		**8.7**%	**6.7**%

Table 8.5: *Summary of systematic uncertainties for the photoproduction and the DIS analysis. The sum of the uncertainties is obtained by adding the individual contributions in quadrature.*

The systematic uncertainties are summarised in table 8.5 for the photoproduction and the DIS sample. The individual uncertainties are added in quadrature to obtain the sum of the uncertainties. Finally, the systematic uncertainty amounts to 8.7% for the analysis of the photoproduction data and to 6.7% in case of the DIS sample.

8.5 Cross Section in Photoproduction

The visible range for the photoproduction sample is summarised in the first column of table 8.1.

The mean acceptance $\bar{\mathcal{A}}_{ET33}$ of electron tagger ET33, see figure 3.1, is determined both in the PYTHIA Monte Carlo simulation and in the data. The latter value is used as a cross check only. The resulting acceptances are:

- PYTHIA: $\bar{\mathcal{A}}_{ET33}(y) = 0.447 \pm 0.001$,
- γp data: $\bar{\mathcal{A}}_{ET33}(y) = 0.440 \pm 0.007$.

The cross section definition 8.2 has to be modified to take the mean acceptance into account:

$$\sigma_{vis}(ep \to eb\bar{b} \to ejjeX) = \frac{N}{\mathcal{L}_{int} \cdot \epsilon_{rec} \cdot \epsilon_{trig} \cdot \epsilon_{L4} \cdot \bar{\mathcal{A}}_{ET33}} \tag{8.5}$$

The integrated luminosity, corrected for prescale factors (see section 3.1 and table 3.1), of this sample is:

$$\mathcal{L}_{int} = 50.79 \text{ pb}^{-1}.$$

A beauty electron fraction of $21.0\% \pm 5.2\%$ has been determined for the photoproduction data (see section 7.2.2): so, out of the 475 electron candidates (see section 7.2), 99.8 ± 24.7 are beauty electrons. Using the reconstruction efficiencies determined in section 8.3.1 and the trigger efficiencies from section 8.3.2.2, the following cross sections for the visible range are obtained:

$$\sigma_{\mathbf{vis}}(\mathbf{ep \to eb\bar{b} \to ejjeX})|_{\mathbf{PYTHIA}} = \mathbf{12.5 \pm 3.1 \pm 1.1 \text{ pb}}$$
$$\sigma_{\mathbf{vis}}(\mathbf{ep \to eb\bar{b} \to ejjeX})|_{\mathbf{CASCADE}} = \mathbf{12.1 \pm 3.0 \pm 1.1 \text{ pb}}$$

The visible cross sections predicted by the two Monte Carlo simulations are:

$$\text{PYTHIA: } \sigma_{vis}(ep \to eb\bar{b} \to ejjeX) = 10.9 \text{ pb}$$
$$\text{CASCADE: } \sigma_{vis}(ep \to eb\bar{b} \to ejjeX) = 8.6 \text{ pb}$$

The differences from the cross sections measured in data to those in the Monte Carlo simulations are within one standard deviation when the statistical as well as the systematical uncertainties are taken into account.

8.6 Cross Section in DIS

The visible range for the DIS sample is summarised in the second column of table 8.1.

The integrated luminosity, already corrected for prescale factors (see section 3.1 and table 3.1), of this sample is:

$$\mathcal{L}_{int} = 51.16 \text{ pb}^{-1}.$$

A beauty electron fraction of $35.1\% \pm 6.0\%$ has been determined for the sample (see section 7.2.2): so, out of the 514 electron candidates (see section 7.2), 180.4 ± 30.8 are beauty electrons. Using the reconstruction efficiencies determined in section 8.3.1 and the trigger efficiencies from section 8.3.2.1, the following cross sections for the visible range are obtained:

$$\sigma_{\mathbf{vis}}(\mathbf{ep \to eb\bar{b} \to ejjeX})|_{\mathbf{RAPGAP}} = \mathbf{11.7 \pm 2.0 \pm 0.8 \text{ pb}}$$
$$\sigma_{\mathbf{vis}}(\mathbf{ep \to eb\bar{b} \to ejjeX})|_{\mathbf{CASCADE}} = \mathbf{13.4 \pm 2.3 \pm 0.9 \text{ pb}}$$

The visible cross sections predicted by the two Monte Carlo simulations are:

$$\text{RAPGAP: } \sigma_{vis}(ep \to eb\bar{b} \to ejjeX) = 8.0 \text{ pb}$$
$$\text{CASCADE: } \sigma_{vis}(ep \to eb\bar{b} \to ejjeX) = 10.0 \text{ pb}$$

So, both simulations agree well with the measurement: the cross section for the RAPGAP simulation is 1.3 standard deviations lower than for the data when taking both statistical and systematical uncertainties into account. The prediction from CASCADE is 1.1 standard deviations below the data. It has to be noted that the RAPGAP simulation contains direct processes only.

8.7 Comparison with Other Measurements

Measurements in the same visible ranges have not yet been performed at HERA.

An attempt has been made at the ZEUS-Experiment to measure the semielectronic decay of beauty hadrons ([67]). Data taken in the years 1996 and 1997 were analysed and a beauty production cross section was determined, consistent with background within 2 – 3 standard deviations. Electron candidates with $p_T > 1.6$ GeV/c were selected using a negative subtraction method for $\mathrm{d}E/\mathrm{d}x$, the background contribution from photon conversion electrons was estimated by Monte Carlo simulations. The beauty and charm electron fractions were obtained by fitting the $p_{T,rel}$ distributions.

A comparison with the analysis presented here is hardly possible. The minimal transverse momentum required for the electron candidate is larger in this analysis and the p_T cuts on the two jets are lower ($p_T(jet1) > 7$ GeV/c, $p_T(jet2) > 6$ GeV/c in case of the ZEUS analysis). The η ranges allowed in this analysis is slightly larger and the Q^2 regime is different ($Q^2 < 1$ GeV^2 in case of the ZEUS analysis, $Q^2 < 0.01$ GeV^2 for this analysis).

The most recent measurement of beauty production at the H1-Experiment has been carried out with the data taken in the years 1999 and 2000 which correspond to an integrated luminosity of 50 pb^{-1}. The semimuonic beauty hadron decay has been studied in the photoproduction and in the DIS regime ([8]). As an experimental signature, a muon with a transverse momentum larger than 2.5 GeV/c was required together with two jets in case of photoproduction and one jet in case of DIS.

The beauty muon fraction was determined by a two dimensional fit to the $p_{T,rel}$ and the impact parameter distributions. Fractions for muons from beauty and charm hadron decays and for misidentified hadrons were measured. The misidentified hadron fraction was fixed for the fit and its value was determined with the help of Monte Carlo simulations.

Photoproduction		
	Electron analysis	**Muon analysis**
Visible range	$Q^2 < 0.01$ GeV^2	$Q^2 < 1$ GeV^2
	$0.29 < y < 0.65$	$0.2 < y < 0.8$
	$p_T(e) > 2.0$ GeV/c	$p_T(\mu) > 2.5$ GeV/c
	$28^\circ < \theta(e) < 145^\circ$	$36.8^\circ < \theta(\mu) < 120^\circ$
	$p_T(jet1(2)) > 6(5)$ GeV/c	$p_T(jet1(2)) > 7(6)$ GeV/c
	$\lvert\eta(jets)\rvert < 2.5$	$\lvert\eta(jets)\rvert < 2.5$
$\sigma_{\mathbf{vis}}$ **[pb]**	$12.1 \pm 3.0 \pm 1.1$	$38.4 \pm 3.4 \pm 5.4$
CASCADE [pb] / PYTHIA [pb]	8.6 / 10.9	22.6 / 20.9
DIS		
	Electron analysis	**Muon analysis**
Visible range	2 GeV$^2 < Q^2 < 100$ GeV^2	2 GeV$^2 < Q^2 < 100$ GeV^2
	$0.05 < y < 0.7$	$0.1 < y < 0.7$
	$p_T(e) > 2.0$ GeV/c	$p_T(\mu) > 2.5$ GeV/c
	$28^\circ < \theta(e) < 145^\circ$	$35.1^\circ < \theta(\mu) < 129.4^\circ$
	$p_T(jet1(2)) > 6(5)$ GeV/c	$p_T(jet1,\ Breit\ frame) > 6$ GeV/c
	$\lvert\eta(jets)\rvert < 2.5$	$\lvert\eta(jet)\rvert < 2.5$
$\sigma_{\mathbf{vis}}$ **[pb]**	$13.4 \pm 2.3 \pm 0.9$	$16.3 \pm 2.0 \pm 2.3$
CASCADE [pb] / RAPGAP [pb]	10.0 / 8.0	12.0 / 6.3

Table 8.6: *Comparison of measured visible cross sections for the electron and the muon analyses.*

The measured cross sections seem to be a factor 1 – 2 above NLO QCD calculations, showing a larger excess at low transverse momenta of the muon candidates. In table 8.6 the visible range is shown together with the visible cross sections for the muon analysis and the electron analysis presented here. The ratio of the measured cross sections in the electron analysis to the Monte Carlo predictions is around one standard deviation for the photoproduction and the DIS data when taking both the statistical as well as the systematical uncertainty into account. The measured beauty muon cross sections are about 1.5 – 2 standard deviations above the value predicted by the simulations.

Chapter 9

Summary and Outlook

The first measurement of the beauty quark cross section using the semileptonic decay into electrons at the H1-Experiment has been presented here. The data taken in the years 1999 and 2000, corresponding to an integrated luminosity of 51 pb^{-1}, were analysed in two sets: photoproduction ($Q^2 < 0.01$ GeV^2) and deep inelastic scattering (DIS, 2 GeV$^2 < Q^2 < 100$ GeV^2). One electron with a transverse momentum larger than 2 GeV/c was required per event as well as two jets with transverse momenta larger than 6 and 5 GeV/c respectively.
The number of electrons from beauty production was obtained by fitting the $p_{T,rel}$ distributions of signal and background contributions to the data. The background is composed of electrons from charm production, electrons from photon conversion processes and misidentified hadrons.

A method for the identification of non-isolated electrons has been developed in the course of the analysis. It is based on a new way of associating tracks measured in the Central Jet Chamber with energy depositions in the Liquid Argon (LAr) Calorimeter. This reconstruction of the Hadronic Final State (HFS) differs from common HFS algorithms in being independent of the order in which tracks and cells are associated.
Three variables are defined for the discrimination between electrons and hadrons: the first one, E/p, is the energy deposited in the LAr calorimeter divided by the particle's momentum measured in the Jet Chamber. The longitudinal energy deposition parameter, λ, is a measure of the energy distribution in the three layers of the electromagnetic calorimeter. The transverse broadening of a shower is measured by the lateral shower spread, ρ.
The shower shape parameters λ and ρ are combined in neural networks with the specific energy loss $\mathrm{d}E/\mathrm{d}x$ measured in the Jet Chamber. Individual neural networks are set up for the 4 LAr wheels used because the different wheel granularities lead to varying λ and ρ distributions. Particles have to pass a preselection in order to reduce the hadron fraction before being assigned to one of the neural networks: all energy measured in the LAr calorimeter has to be deposited in the electromagnetic section and E/p has to be in the range expected for electrons: $0.8 < E/p < 1.2$. About 90% of all hadrons are rejected while more than 80% of the electrons pass these requirements.
The electron identification efficiency of the neural networks is about 75% for a sample of dijet events. The electron selection purity in the data sets has been determined to be 70 – 80%. The ratio of electrons from beauty production to background particles (other electrons, misidentified

hadrons) is approximately 1:4 for the photoproduction sample and about 1:2 for the DIS data. The hadron misidentification rate of less than 0.1% is competitive to that of analyses with muons identified in the instrumented iron.
The electron identification method was successfully tested on data by reconstructing inelastically produced J/Ψ-mesons decaying into two electrons.

475 electron candidates have been selected in the photoproduction sample, 514 in the DIS sample. A fit procedure has been established in which the contributions from photon conversion electrons and from misidentified hadrons are determined by fitting the ΔR distribution and the E/p distribution. ΔR represents the distance from a particle to its closest neighbouring track. The ΔR distribution is sensitive to the fraction of photon conversion electrons in a sample. Neither E/p nor ΔR were used as parameters in the neural networks and therefore pass the networks undistorted.
The photon conversion fraction and the misidentified hadron fraction are then fixed for the fit to the $p_{T,rel}$ distribution in which the beauty electron fraction and the charm electron fraction are determined. The beauty electron fraction in the photoproduction sample has been found to be $21.0\% \pm 5.2\%$, a value of $35.1\% \pm 6.0\%$ has been obtained for the DIS sample.
The stability of the beauty electron fraction has been successfully checked by varying the fractions for photon conversions and misidentified hadrons. In addition it has been shown with a Monte Carlo simulation that the true beauty electron fraction is well reproduced by the fit procedure.
It has been tried to determine the electron beauty fraction by fitting the impact parameter distribution instead of the $p_{T,rel}$ distribution. However, not enough statistics are available for this fit and the resulting uncertainty on the electron beauty fraction is large.

The cross section in the visible range given in table 8.1 was determined to be $\sigma_{vis}(ep \rightarrow eb\bar{b} \rightarrow ejjeX)|_{PYTHIA} = (12.5 \pm 3.1 \pm 1.1)$ pb for the photoproduction sample and $\sigma_{vis}(ep \rightarrow eb\bar{b} \rightarrow ejjeX)|_{RAPGAP} = (11.7 \pm 2.0 \pm 0.8)$ pb in case of DIS. The reconstruction efficiencies have been determined using PYTHIA and RAPGAP Monte Carlo simulations respectively; they were checked with CASCADE Monte Carlo simulations. Possible sources for systematic uncertainties were carefully examined and total systematic uncertainties of 8.7% (photoproduction) and 6.7% (DIS) have been determined.
The cross sections predicted by the Monte Carlo generators PYTHIA, RAPGAP and CASCADE match the measurement well: the cross section measured for the photoproduction sample agrees with the Monte Carlo predictions within one standard deviation. In case of the DIS data, agreement with the Monte Carlo generators is found within 1.5 standard deviations.

Recent considerations suggest that measured beauty cross sections and theoretical predictions, obtained from modern NLO programs such as FONLL ([68]) and MC@NLO ([69], [70]), agree within the respective uncertainties ([1], [2], [3]). So, the question arises in which way, apart from increased luminosity and optimised triggers, existing analyses of beauty quark production have to be modified to further shrink the statistical and systematical uncertainties.

For the analysis presented here, the number of electron candidates would increase when applying lower cuts on the transverse momentum of the particles. However, the energy resolution of the LAr calorimeter decreases with lower momenta while the separation power of $\mathrm{d}E/\mathrm{d}x$ between electrons and pions increases. The ratio of beauty electrons to background particles (other electrons, misidentified hadrons) would probably decrease.
The overall electron identification efficiency might be improved if softer requirements were applied for the preselection of the particles. The electron selection purity would deteriorate if the performance of the neural networks was not improved at the same time. Using a second type of neural network for particles failing the original preselection might solve this problem.
Another possibility to gain statistics, in case of the DIS analysis, is to require only one jet, boosted e. g. to the Breit frame. An increase in statistics of up to 30% could be expected according to the muon analysis ([8]) so that the application of the impact parameter method might become possible.
Finally, one might want to go through the process of electron identification again, reviewing the variables and methods which have been discarded in the course of this analysis, such as using Fisher's Discriminant. Other multivariate methods might be tested, for example support vector machines.

Clean heavy quark samples are obtained if double-tagging of the heavy quark pair is performed. The most promising channel appears to be the study of electron muon pairs. The events would be triggered by high momentum muons reconstructed in the instrumented iron. The beauty fraction in the resulting event sample would already be high so that only moderate momentum cuts for the electron would be necessary. Alternatively, the requirements on the electrons in the neural networks could be loosened, leading to increased electron identification efficiencies.
It has already been shown in this thesis that the measurement of $D^{*\pm}$-meson electron pairs is possible with the data taken in the HERA-I run period. An analysis of this channel may be promising – although the overall event yield is low – because a very clean charm quark sample is obtained. The low transverse momenta required for the electron candidate, $p_T > 0.8$ GeV/c, do not lead to an enrichment of beauty quark processes as is the case for the $D^{*\pm}$-meson muon analysis ([9]) where high muon momenta have to be required. A beauty cross section measurement using $D^{*\pm}$-meson electron pairs may not be possible with the statistics of the HERA-I data.

Several improvements for the analysis of heavy quarks, aside from the increase in statistics, are expected from the upcoming HERA-II data: a better separation of the $\mathrm{d}E/\mathrm{d}x$ values of electrons and hadrons is observed because the readout of the Jet Chamber has been adjusted such that less hits from minimally ionising pions are lost. The difference between the minimum and the saturation plateau has increased as a result of the modification.
The installation of the trigger level 3 components of the Fast Track Trigger (FTT) should allow online reconstruction of final states such as the golden decay channel of $D^{*\pm}$-mesons. Without the FTT, events of open heavy quark production can only be recorded if either the scattered electron or high momentum muons are triggered. Using the FTT, access would be gained to the regime of untagged photoproduction, largely increasing the statistics available for the analysis of $D^{*\pm}$-meson electrons pairs.

Ideally, the improvements in the HFS reconstruction method presented here should be integrated into the standard HFS algorithm. However, the development of a muon identification method based on similar principles as the electron identification has to be completed first. It should be noted that an HFS reconstruction method should be performed during the event reconstruction and not on the analysis level. Additional information from the track reconstruction, such as kinks indicating radiation of photons, could be used which are not accessible later on. The reconstruction of energy depositions in the calorimeters should be done simultaneously with the track cell assignment so that the same particle associations would be used for the HFS and for the software weighting of the calorimeter energies.

Appendix A

Shower Shapes in LAr Wheels

The λ, ρ and hot core fraction distributions obtained from single particle Monte Carlo simulations of electrons and pions will be shown here in the LAr wheels *CB1 – FB1*. The distributions for pions will be compared before and after the preselection of table 5.1. The particles were simulated with a flat momentum distribution in the range 1.5 GeV/c < p < 10 GeV/c and a cut on $p_T > 2$ GeV/c was applied afterwards.

The **longitudinal energy distribution** has been introduced in section 5.2. It is defined as

$$\lambda = \frac{\sum_{i=1}^{3} E_i \cdot i}{\sum_{i=1}^{3} E_i} \,. \tag{A.1}$$

The index i is the number of the electromagnetic layer, with $i = 1$ being the innermost one.

The **lateral energy distribution**, introduced in section 5.3, is defined as the average of the distances $d(P_j, CA)$ of the cells' positions P_j to the cluster axis CA, weighted by $w_j = \sqrt{|E_j|}$

$$\rho = \frac{\sum_{j=1}^{N} w_j \cdot d(P_j, CA)}{\sum_{j=1}^{N} w_j} \,, \tag{A.2}$$

with E_j being the energy of cell j.

The **hot core fraction**, see section 5.4.1, is defined as the fraction of energy in the four most energetic cells of the whole cluster. The hot core fraction is zero if the cluster contains less than four cells.

The distributions for electrons are shown in the left column. The pion distributions before the preselection are shown in the middle and the right column shows the pion distributions after the preselection.

A.1 Longitudinal Energy Distribution λ

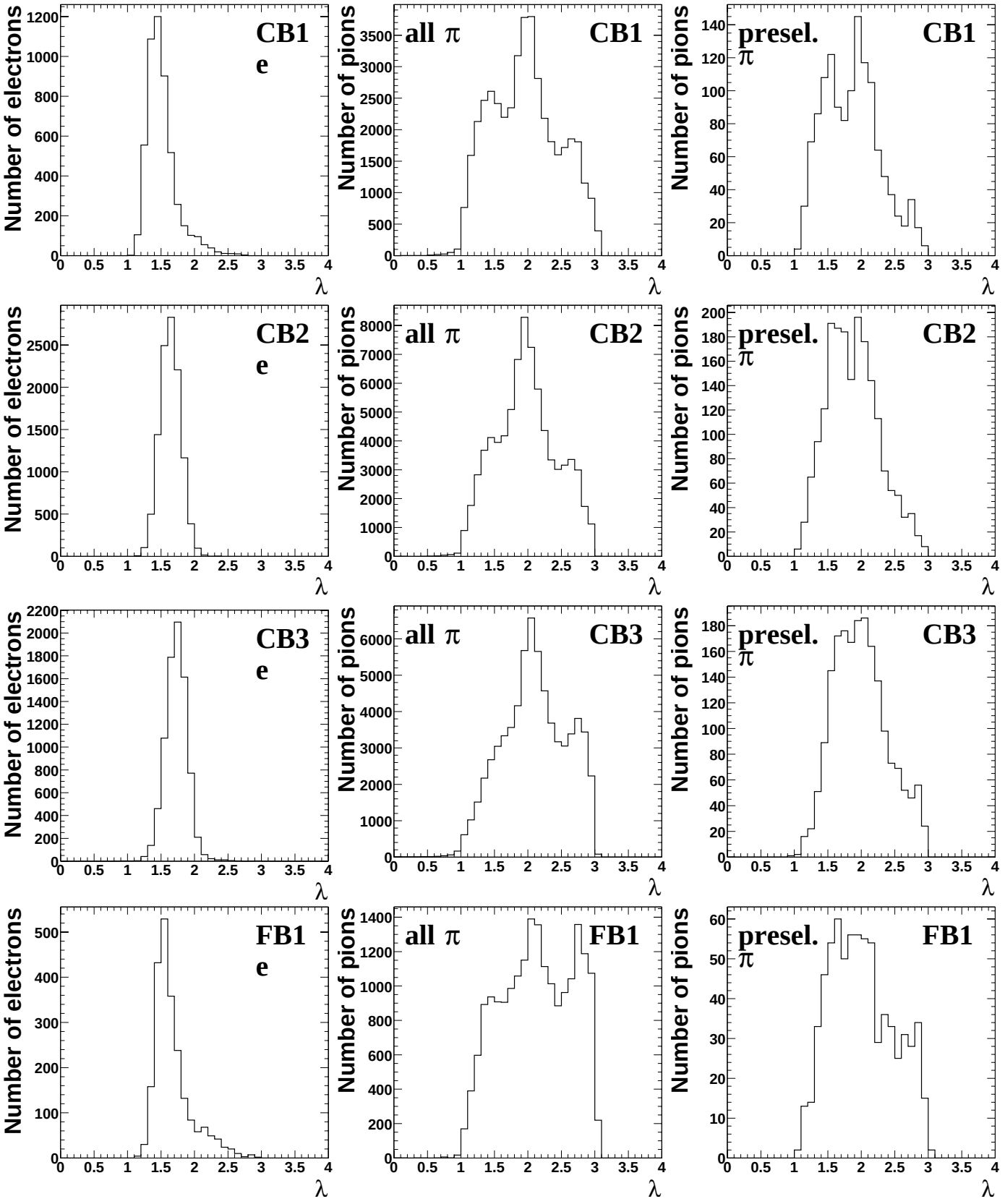

A.2 Lateral Energy Distribution ρ

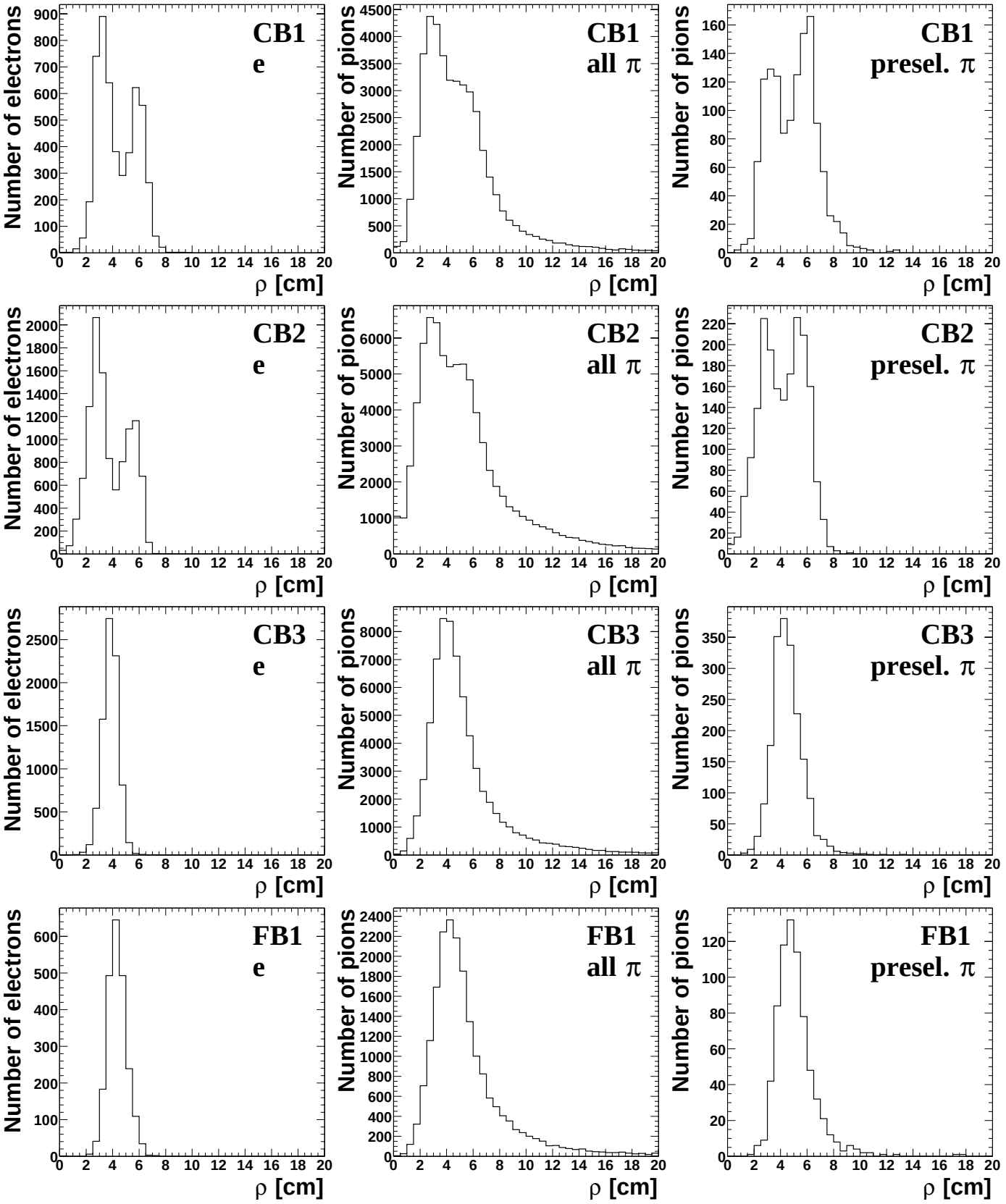

A.3 Hot Core Fraction

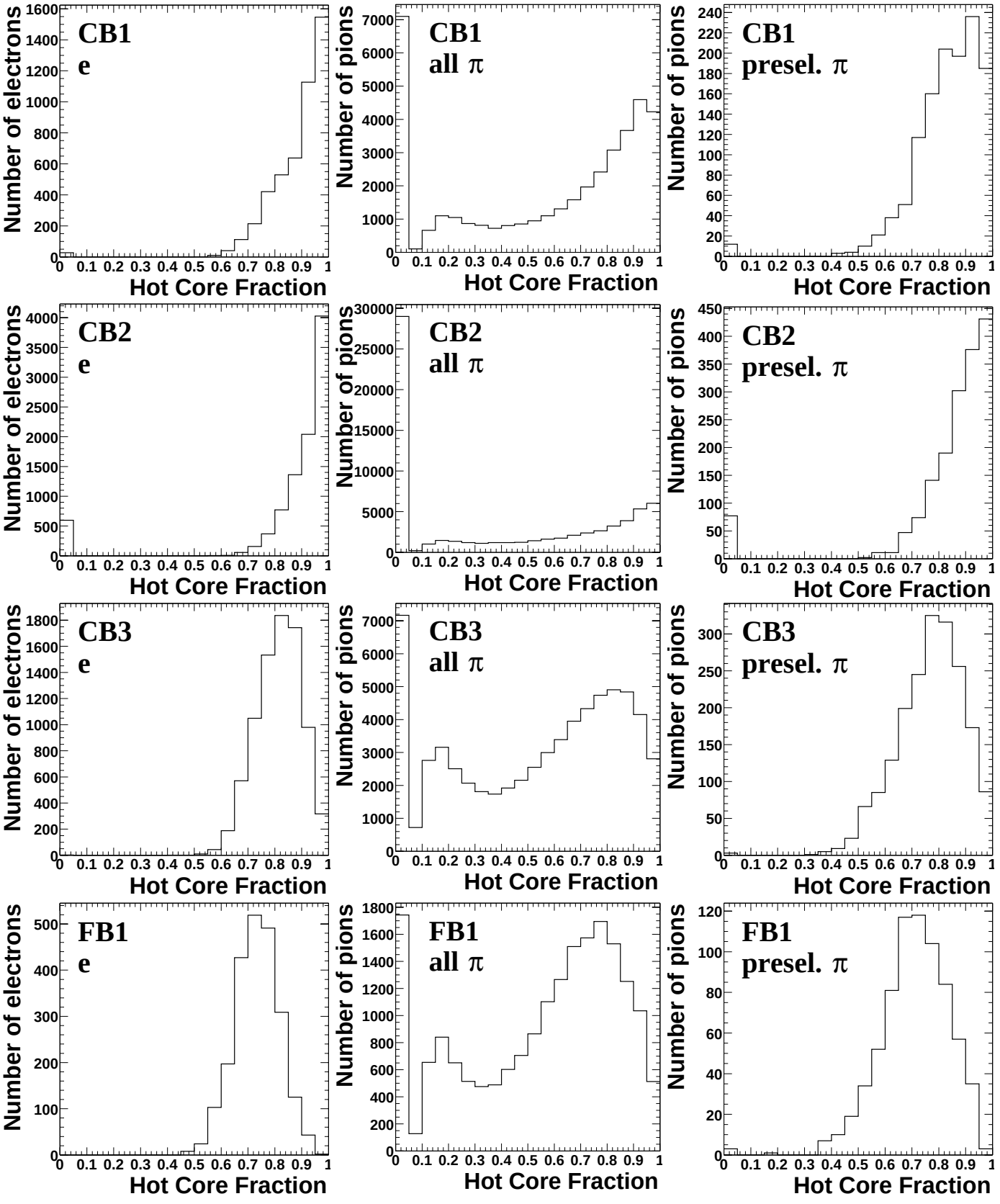

Bibliography

[1] M. Cacciari, S. Frixione, Michelangelo L. Mangano, P. Nason, and G. Ridolfi, *QCD analysis of first b cross section data at 1.96 TeV*, hep-ph/0312132.

[2] M. Cacciari, *Rise and Fall of the Bottom Quark Production Excess*, hep-ph/0407187.

[3] S. Frixione, *Bottom Production*, in *Proceedings of DIS'2004*, hep-ph/0408317.

[4] P. Fleischmann, *Elastic J/Ψ production at HERA*, PhD thesis, Universität Hamburg, 2004.

[5] P. Fleischmann, *Elastic Photoproduction of J/Ψ Mesons*, H1prelim-03-075.

[6] H1 Collaboration, A. Aktas *et al.*, *Inclusive Production of D^+, D^0, D_s^+ and D^{*+} Mesons in Deep Inelastic Scattering at HERA*, Submitted to Eur. Phys. J. (2004), hep-ex/0408149.

[7] L. Finke, *Untersuchungen zum Erkennen von B-Mesonen im H1-Detektor*, Diploma thesis, I. Institut RWTH Aachen, 2003.

[8] H1 Collaboration, A. Aktas *et al.*, *Measurement of Beauty Production at HERA Using Events with High Momentum Muons*, To be submitted to Eur. Phys. J. C.

[9] J. Wagner, *Charm and Beauty Production at HERA with D^*-Muon Events*, PhD thesis, Universität Hamburg, 2004.

[10] H1 Collaboration, C. Adloff *et al.*, *Inelastic Leptoproduction of J/Ψ Mesons at HERA*, Eur. Phys. J. **C25**, 41 (2002), hep-ex/0205065.

[11] S. Frixione, M. L. Mangano, P. Nason, and G. Ridolfi, *Heavy-quark production*, (1997), hep-ph/9702287.

[12] S. Eidelman *et al.*, *Review of Particle Physics*, Physics Letters B **592**, 1+ (2004).

[13] W.-K. Tung, *Perturbative QCD and the Parton Structure of the Nucleon*, http://www.physics.smu.edu/~olness/cteqpp/tung2003/IntroPqcd.pdf.

[14] T. Sjöstrand *et al.*, *High-Energy-Physics Event Generation with PYTHIA 6.1*, Comput. Phys. Commun. **135**, 238 (2001), hep-ph/0010017.

[15] H. Jung, Comput. Phys. Commun. **86**, 147 (1995).

[16] V. N. Gribov and L. N. Lipatov, Yad Fiz **15**, 781 (1972).

[17] G. Altarelli and G. Parisi, Nucl. Phys. B **126**, 298 (1977).

[18] M. Ciafaloni, Nucl. Phys. B **296**, 49 (1988).

[19] S. Catani, F. Fiorani, and G. Marchesini, Phys. Lett. B **234**, 339 (1990).

[20] G. Marchesini, Nucl. Phys. B **445**, 49 (1995).

[21] H. Jung and G. P. Salam, *Hadronic Final State Predictions from CCFM: The Hadron- Level Monte Carlo Generator CASCADE*, Eur. Phys. J. **C19**, 351 (2001), hep-ph/0012143.

[22] H. Jung, *The CCFM Monte Carlo Generator CASCADE*, Comput. Phys. Commun. **143**, 100 (2002), hep-ph/0109102.

[23] C. Peterson, D. Schlatter, I. Schmitt, and P. Zerwas, Phys. Rev. D **27**, 105 (1983).

[24] B. Andersson, G. Gustafson, G. Ingelman, and T. Sjöstrand, *Parton Fragmentation and String Dynamics*, Phys. Rept. **97**, 31 (1983).

[25] H1 Collaboration, I. Abt *et al.*, *The H1 Detector at HERA*, Nuclear Instruments and Methods in Physics Research **A386**, 310 (1997).

[26] T. Kuhr, *Messung des Wirkungsquerschnitts von b-Quark-Produktion in tiefunelastischer Elektron-Proton-Streuung bei H1*, PhD thesis, Universität Hamburg, 2002.

[27] H1 Collaboration, *A Fast High Resolution Track Trigger for the H1 Experiment*, hep-ex/0104010.

[28] D. Pitzl *et al.*, *The H1 Silicon Vertex Detector*, Nuclear Instruments and Methods in Physics Research **A454**, 334 (2000), hep-ex/0002044.

[29] H1 SPACAL Group, R. D. Appuhn *et al.*, *The H1 Lead/Scintillating-Fibre Calorimeter*, Nuclear Instruments and Methods in Physics Research **A386**, 397 (1997).

[30] J. Reidberger, *The H1 Trigger with Emphasis on Tracking Triggers*, (1995), `H1-01/95-419`.

[31] T. Wolff *et al.*, *A Driftchamber Track Finder for the First Level Trigger of H1*, (1992), `H1-02/92-213`.

[32] H. Beck, *Principles and Operation of the z-Vertex Trigger*, (1996), `H1-05/96-479`.

[33] F. Sefkow, E. Elsen, H. Krehbiel, U. Straumann, and J. Coughlan, *Experience with the First Level Trigger of H1*, IEEE Trans. Nucl. Sci. **42**, 900 (1995).

[34] V. Boudry *et al.*, *The Inclusive Electron Trigger for the SPACAL: Design and CERN-Test Results*, (1995), `H1-03/95-430`.

[35] E. Sauvan, *Electron Finders in OO*, https://www-h1.desy.de/icas/oop/finders/efinder/oo-efinder.html.

[36] H1 Collaboration, S. Aid *et al.*, *Measurement of the Total Photon Proton Cross Section and its Decomposition at 200 GeV Centre of Mass Energy*, Z. Phys. **C69**, 27 (1995), hep-ex/9509001.

[37] S. Levonian, *Help for the e-tagger related analyses*, https://www.desy.de/~levonian/QPETAC.html.

[38] S. Levonian, *Event Classification used for Repro-2000*, https://www-h1.desy.de/itrigger/L4Farm/rep_2000_eclass.html.

[39] H1 Collaboration, *H1 OO Analysis Framework*, https://www-h1.desy.de/icas/oop/.

[40] A. Meyer, *A New Physics Analysis Framework for H1*, EPS 2001, Budapest.

[41] S. Ellis and D. Soper, *Succesive Combination Jet Algorithm for Hadron Collisions*, Physical Review **D48**, 3160 (1993), hep-ph/9305266.

[42] H1 Collaboration, *Guide to Simulation program H1SIM*, https://www-h1.desy.de/imc/h1sim/guide.html.

[43] A. Kwiatkoswki, H. Spiesberger, and H.J. Möhring, Comput. Phys. Commun. **69**, 155 (1992).

[44] J. Marks, *HFS*, https://www-h1.desy.de/iwork/iescale/hfs/hfs.html.

[45] M. Peez, *Hadron Finder in OO (HADROO)*, https://www-h1.desy.de/icas/oop/finders/hadronfinder/oo-hfsfinder.html.

[46] G. Alexander *et al.*, *TESLA Technical Design Report, Part IV, A Detector for TESLA*, 2001, http://www.desy.de/~lcnotes/tdr/released/detector/tdr.ps.gz.

[47] F. Jacquet and A. Blondel, *Detectors For Charged Current Events*, in *Study for an ep-Facility in Europe*, edited by U. Amaldi, pp. 393–396, DESY, 1979.

[48] R. Sedgewick, *Algorithmen in C++* (Addison-Wesley, Bonn, 1992).

[49] P. E. Black, *Dictionary of Algorithms and Data Structures: balanced tree*, http://www.nist.gov/dads/HTML/balancedtree.html.

[50] R. Wigmans, *Calorimetry* (Oxford University Press, September 2000).

[51] B. List and A. Mastroberardino, in *Proc. of the Workshop on Monte Carlo Generators for HERA Physics*, p. 396, 1999, DESY-PROC-1999-02.

[52] B. Naroska, S. Schiek, and G. Schmidt, *Lepton Identification in the H1 Detector at Low Momenta*, (1997), H1-05/97-518.

[53] R. Lemrani-Alaoui, *Prompt Photo Production*, PhD thesis, Universität Hamburg, 2003.

[54] R. Brun, F. Bruyant, M. Maire, A. C. McPherson, and P. Zanarini, *GEANT 3 User's Guide*, 1987, CERN-DD/EE/84-1.

[55] L. Faussett, *Fundamentals of Neural Networks* (Prentice-Hall, 1994).

[56] B. Weßling, *Identifizierung von Elektronen in D^*-Ereignissen mit dem H1-Detektor*, Diploma thesis, Universität Hamburg, 2001.

[57] G. Feldman *et al.*, *Observation of the Decay $D^{*+} \to D^0\pi^+$*, Phys. Rev. Lett. **38**, 1313 (1977).

[58] J. Kroseberg, *A Measurement of Beauty Production in High-Energy Positron-Proton Scattering*, PhD thesis, Universität Zürich, 2002.

[59] O. Behnke, *Measurement of Beauty Photoproduction at HERA using Semi-Muonic Decays*, H1prelim-03-072.

[60] R. Barlow and C. Beeston, *Fitting finite Monte Carlo samples*, Comput. Phys. Commun. **77**, 219 (1993).

[61] S. Schmidt, *Inclusive D^* Meson and Associated Dijet Production in Deep Inelastic Scattering*, H1prelim-03-074.

[62] S. Schmidt, *Messung charminduzierter Zweijetereignisse in tief inelastischer ep-Streuung mit dem H1-Detektor bei HERA*, PhD thesis, Technische Universität München, 2004.

[63] R. Barlow, *Systematic Errors: facts and fictions*, hep-ex/0207026 .

[64] R. Barlow *et al.*, *Recommended Statistical Procedures for BABAR*, BABAR Analysis Document Nr 318, Version 1 (2002).

[65] T. Laštovička, *Measurement of the Inclusive Deep Inelastic Scattering Cross Section at Low Q^2*, PhD thesis, Humboldt Universität zu Berlin, 2004.

[66] S. Levonian, *H1 Lumi Summary*, https://www-h1.desy.de/h1det/lumi/summary_tables/summary.html.

[67] ZEUS Collaboration, J. Breitweg *et al.*, *Measurement of open beauty production in photoproduction at HERA*, The European Physical Journal C **18**, 625 (2000).

[68] M. Cacciari, M. Greco, and P. Nason, JHEP **9805**, 007 (1998), hep-ph/9803400.

[69] S. Frixione and B. R. Webber, JHEP **0206**, 029 (2002), hep-ph/0204244.

[70] S. Frixione, P. Nason, and B. R. Webber, JHEP **0308**, 007 (2003), hep-ph/0305252.

List of Figures

List of Tables

Danksagung

Zuallererst danke ich Herrn Prof. Blobel für die hervorragende Betreuung und für viele lehrreiche Diskussionen im Verlauf der gesamten Arbeit. Es hat mir wirklich großen Spaß gemacht, diesen Daten ihre Elektronen zu entlocken.
Bei Herrn Prof. Heuer möchte ich mich für die Anfertigung des zweiten Gutachtens bedanken. Großer Dank geht an Frau Prof. Naroska für ihre tatkräftige Unterstützung der Analyse innerhalb des letzten Jahres.

Andreas Meyer und Olaf Behnke danke ich für ihre Hilfe mit den Monte-Carlo-Simulationen. Andreas sei hier auch für so manch andere Diskussion gedankt, obwohl, oder gerade weil, wir häufig unterschiedlicher Meinung waren.

Bei meinen Bürokollegen Dirk, Gero, Ingo, Jeannine, Martin, Svetlana und Thomas bedanke ich mich für die angenehme Arbeitsatmosphäre während meiner gesamten Zeit hier bei H1. Insbesondere möchte ich mich bei Gero und Ingo für die lustige und produktive Zusammenarbeit am H1OO-Projekt bedanken. Gero, unser μODS ist immer noch das beste ;-)

Meinen Eltern danke ich für ihre unermüdliche Unterstützung nicht nur während der letzten Jahre.